HIGH FREQUENCY ELECTRO-OPTIC MODULATORS FOR INTEGRATED OPTICS

A Thesis

Submitted to the Faculty of Engineering

of the University of Glasgow

for the degree of

Doctor of Philosophy

by

Douglas F. Clark, B.Sc.(Eng.)

August 1986

Dedicated to:

Mum, Graham and Nan.

Liber scriptus proferetur
in quo totum continetur
unde mundus judicetur

ACKNOWLEDGEMENTS

I would like to thank Dr. Richard De La Rue for his encouragement, enthusiasm and general concern for my well being throughout the course of this work.

I would also like to thank my other colleagues especially M.R.S.Taylor for his technical advice about microwave circuitry, J.R.Tobin for sharing his unique perception of the world with me. The help of A.C.G.Nutt and K.K.Wong is gratefully acknowledged during the initial investigation of the proton exchange process. Special thanks are due to Sumaia Al Shukri for her many helpful remarks and discussions during the compilation of this thesis.

I am also indebted to the other members of Staff in the Department of Electronics and Electrical Engineering (both academic and technical) for their advice and support, either directly or indirectly. In particular: Dr. J.Richter for many thought provoking discussions, Norman Bett and Tom Watson for their unwavering dedication in helping to develop new methods for fabricating the standing wave modulator.

I sincerely thank Professor John Lamb for the opportunity to use his excellent research facilities and Professor Masayuki Izutsu, Osaka University, for his initial proposal of the standing wave modulator design and his continuing encouragement.

Financial support was given by an S.E.R.C. C.A.S.E award in conjunction with S.T.L. (Ltd.).

Finally, I would like to thank Mrs. M.R.S.Taylor for

typing the initial draft of this thesis from a manuscript that did not excel in clarity or coherence, and to D.K.Goold for his helpful advice during the preparation of this thesis.

TABLE OF CONTENTS.

SUMMARY

This thesis encompasses the theoretical design and experimental evaluation of a novel type of high speed phase modulator using $LiNbO_3$ and GaAs technology suitable for guided wave optics.

A brief review of the development of Integrated Optics and in particular of optical modulators is given in Chapter 1, along with an outline of the aims of this project.

Chapter 2 provides a comprehensive survey of the methods available for determining the theoretical propagation constant of a guided wave in a variety of dielectric waveguide configurations. A comparison between the various methods is made to provide an indication of the accuracy and complexity of each procedure for a particular waveguide geometry. The effect of metal films in close proximity to optical waveguides on the propagation characteristics is derived through the effective index method. The results obtained are then applied to minimise absorption losses due to the metal overlay in active devices.

The main theoretical design of the proposed electrode structure is developed in Chapter 3. The input impedance of the device is matched to the characteristic impedance of the transmission line drive system at the operating frequency using the standard transmission line equations for low-loss lines. The response of the device is modelled by a computer program which calculates the input impedance of two short circuited transmission lines of unequal length connected in parallel. The program allows the asymmetry of the line lengths, the attenuation

constant and characteristic impedance to be independently varied so that their influence upon the overall response may easily be determined. An expression is derived for the theoretical depth of modulation and the power/bandwidth ratio for such a device. Finally a description is given of the numerical methods used to obtain the characteristic impedance and attenuation constant of symmetric and asymmetric coplanar microwave waveguide. The chapter concludes with a brief mention of the analysis procedure for Schottky contacts on GaAs.

The general photolithographic and fabrication procedures for forming optical waveguides in $LiNbO_3$ and GaAs are introduced in chapter 4. This chapter also gives a detailed account of the modified lift-off technique which is successfully employed to pattern metal films up to 2μm thick - a technique which is required for the standing wave modulator electrode.

The use of proton-exchange waveguides as a suitable optical waveguide for high speed active devices is explored in chapter 5. An initial experimental investigation is presented with the theoretical determination of the refractive index profile for waveguides formed in X- and Z- cut $LiNbO_3$ from the observed optical properties. The fabrication parameters required to produce monomode stripe optical waveguides are determined and verified experimentally for a variety of exchange conditions. Other techniques are discussed which offer more control over the refractive index profile and address the problem of index stability. A brief description of the micro-analytical techniques available to monitor the hydrogen concentration is also given.

Chapter 6 describes the methods available for characterising the small signal response of the modulator. A comparison is given between the experimental results and the theoretical predictions. Factors affecting the discrepancies in the response are also mentioned. In particular the uncertainties of the high frequency dielectric constants of $LiNbO_3$ are quantified.

Chapter 7 concludes the thesis with an outline of the future work required and the conclusions that may be drawn from the work carried out so far on proton exchange and the standing wave modulator.

CHAPTER 1

1.0 INTRODUCTION

Optical communication systems have arisen out of the inadequacy and expense of existing technology to keep pace with ever-increasing bandwidth demands. These requirements have primarily been brought about by the extensive transfer of information between commercial and scientific centres. The relative cheapness and small physical size of optical fibres, along with their capacity to carry large bandwidth signals, have made them the natural successor to existing systems.

Although optical communication systems are not a new idea, the realisation of such systems was not possible until the early sixties with the development of coherent light sources. Indeed, electromagnetic radiation confinement within dielectric structures was shown to be theoretically possible as early as 1910 by Hondros et al. [1], although in 1899 Sommerfeld [2] showed that fields could be confined to a dielectric coating around a metallic cylinder. However, it was not until 1966 that the first optical fibre transmission system was proposed by Kao et al. [3]. By today's standards, these systems were crude with fibre losses of 40dB/km compared to 0.18dB/km for single mode fibres used today [4].

In 1969 Miller [5] suggested that many of the components comprising an optical system such as lasers, detectors, switching devices and filters could be fabricated on a single chip in a manner analogous to large scale semiconductor integration. From this possibility the term "Integrated optics" arose, although a more apt term would have been "Guided wave optics" [6,7]. This concept,

nonetheless still remains, the ultimate aim being to have several devices fabricated in the same chip with all the necessary electronic processing circuitry as well. Conventional photolithographic methods could be employed to form the complex optical circuit patterns on one small chip.

The active devices necessary for systems consist mainly of modulators, switches and filters. These devices are fabricated using materials which exhibit electro-optic, magneto-optic or pyro-electric properties. The other remaining active devices, such as lasers and detectors, have to be fabricated using semiconductors formed from Ga,In,P,Al and As compounds. These elements may be combined to produce ternary and quaternary heterostructure materials whose band-gap may be continually varied between 0.8μm and 2.5μm. Optical waveguides and detectors have also been fabricated in semiconductor materials and it may be concluded that III-V compounds offer the possibility of total integration [8], although the different electrical carrier concentration requirements and composition of each layer for the different devices may be difficult to realise on a single substrate.

Several materials other than glass [9] have been used to illustrate the concept of integrated optics to date. The ferroelectric materials $LiNbO_3$ and to a lesser extent $LiTaO_3$ [10] have been found to be especially useful for manufacturing both active and passive devices. In general they exhibit large electro-optic coefficients, are strongly pyro-electric and possess large non-linear coefficients. However $LiNbO_3$ has gained greater acceptance because of its higher Curie temperature and greater pyro-electric coefficient. The only drawback is

that total integration, with $LiNbO_3$ as the substrate, is difficult because lasers and sources cannot readily be formed.

Optical waveguides can be formed in $LiNbO_3$ by a number of different methods. Waveguides were first formed by the controlled out-diffusion of lithium at elevated temperatures [11]. Out-diffusion was superceded by in-diffusion of transition metals [12] into the bulk of the substrate to produce low loss one and two dimensional waveguides. The most popular transition metal for this purpose is titanium and it appears unlikely that there will be any contender to succeed the present method in the immediate future. Currently, work is being carried out on the proton-exchange method [13] which shows great promise, though several problems inherent with proton-exchange still have to be addressed: notably the refractive index stability and the reduced electro-optic effect. The variety of devices that have been reported using $LiNbO_3$ technology is remarkable in its diversity and the number of devices that can be formed.

The simplest active device in $LiNbO_3$ is the single waveguide phase modulator. Several very good general review articles have been written about electro-optic modulators especially those by Alferness [14], Chen [15] and Kaminow [16]. The local refractive index of the waveguide is modified by the application of a voltage to electrodes in close proximity to the optical waveguide which locally alters the propagation characteristics of the confined optical field. The effect can be maximised by the correct orientation of the electrode with respect to the crystal axes and this may be obtained from the electro-optic tensor [17]. A numerical

calculation is also necessary to compute the ideal configuration to maximise the overlap integral between the electric and optical fields.

An amplitude modulator may be constructed by two phase modulators connected in a push-pull configuration to give a Mach-Zehnder Interferometer [18]. Other modulators that have been reported are Bragg deflection modulators [19], and the cut-off modulator [20]. Directional couplers [21] and active Y-junctions [22] have also been designed which can switch light between either waveguide at very high frequencies. For operation upto 1-2GHz the bandwidth of the electrode is found by analysing it as a simple RC circuit. Very high frequency operation requires the travelling wave modulator which offers bandwidths in excess of 10GHz [23]. In this device the electrode structure is designed to match the chacteristic impedance of the drive system. The design of the electrode requires careful attention and involves using coplanar asymmetric microwave waveguide. The optical waveguide then runs parallel to the electrode, and the R.F. field interacts with the optical field to produce phase modulation. The high frequency response falls off due to phase mismatch between the R.F. and the optical field.

Other devices of interest are TE-TM mode converters [24] and optical bistable devices [25]. Non-linear effects exhibited by $LiNbO_3$ have been used to produce second harmonic generators [26] and parametric converters [27].

1.1 OBJECT.

The aim of this project was to develop a high frequency modulator operating at 10GHz using either proton-exchange or titanium in-diffusion into $LiNbO_3$ and to obtain the experimental frequency response of such a device. An initial attempt was also made to synthesize a device using III-V semiconductor technology, but the material requirements could not easily be obtained.

The design of the modulator was based upon a new form of electrode structure, only recently reported by Molter-Orr et al. [28]. It was envisaged that this modulator would be useful for high frequency, relatively narrow bandwidth operation or for producing pico-second pulses. Considerable computing was required to ascertain the frequency response of the electrode structure and the variation with metal film thickness. The theoretical conduction losses of the electrode structure were also calculated by using a finite difference method to find the restrictions imposed on the bandwidth and Q factor of the standing wave modulator. It should be noted that guided-wave optical devices operating at 10GHz had hitherto not been made at this University.

References Chapter 1

[1] D.Hondros and P.Debye.
Elektromagnetische Wellen an Dielektrischen Drahten.
Ann. der Physik, Vol.32(8), 1910, pp.465-476.

[2] A.Sommerfeld.
Ueber die Fortpflanzung elektrodynamischer Wellen langs eines Drahates.
Ann. der Physik, Vol.67(2), 1899, pp.233-290.

[3] K.C.Kao and G.A.Hockham.
Dielectric fibre surface waveguides for optical frequencies.
Proc. I.E.E., Vol.113(7), 1966, pp.1151-1150.

[4] T.Miya, Y.Terunuma, T.Hosaka and T.Miyashita.
Ultimate low-loss single mode fibre at 1.55μm.
Elect. Letts., Vol.15(4), 1979, pp.106-108.

[5] S.E.Miller.
Integrated optics: an introduction.
Bell Sys. Tech. Journ., Vol.48(7), 1969, pp.2959-2069.

[6] P.K.Tien.
Integrated optics and new wave phenomena in optical waveguides.
Rev. Mod. Phys., Vol.49(2), 1977, pp.361-381.

[7] H.F.Taylor and A.Yariv.
Guided Wave Optics.
Proc. I.E.E.E., Vol.62(8), 1974, pp.1044-1060.

[8] D.Botez and G.J.Herskowitz.
Components for optical communications-sytems.
Proc.I.E.E.E., Vol.68(6), 1980, pp.689-731.

[9] T.G.Giallorenzi, E.J.West, R.Kirk, R.Ginter and R.A.Andrews.
Optical waveguides formed by thermal migration of ions in glass.
Appl. Opt., Vol.12(6), 1973, pp.1240-1246.

[10] A.Rauber.
Chemistry and physics of lithium niobate.
Current topics in materials science.
Vol.1 ed. E.Kaldis, North Holland, 1978.

[11] I.P.Kaminow and J.R.Carruthers.
Optical waveguiding layers in $LiNbO_3$ and $LiTaO_3$.
Appl. Phys. Lett., Vol.22(7), 1973, pp.326-328.

[12] R.V.Schmidt and I.P Kaminow.
Metal diffused optical waveguides in $LiNbO_3$.
Appl. Phys. Lett., Vol.25(8), 1974, pp.458-460.

[13] J.L.Jackel, C.E.Rice and J.J.Veselka.
Proton exchange for high index waveguides in $LiNbO_3$.
Proc. Topical Meeting on Integrated and Guided Wave Optics., Pacific Grove, 1982, PDP1

[14] R.C.Alferness.
Waveguide electro-optic modulators.
I.E.E.E. Trans. Microwave Theory and Tech.
Vol.M.T.T.30(8), 1982, pp.1121-1137.

[15] Fang-Shang Chen.
Modulators for optical communications.
Proc. I.E.E.E., Vol.58(10), 1970, pp/1140-1157.

[16] I.P.Kaminow.
Optical waveguide modulators.
I.E.E.E. Trans. Microwave Theory and Tech.
Vol.M.T.T.23(1), 1975, pp.57-69.

[17] O.G.Ramer.
Integrated optic electro-optic modulator
electrode analysis.
I.E.E.E. J. Quant. Electr., Vol.QE18(3), 1982,
pp.386-392.

[18] V.Ramaswamy, M.D.Divino and R.D.Standley.
A balanced bridge modulator switch.
Appl. Phys. Lett.,Vol.32(10), 1978, pp.644-646.

[19] J.C.An, Y.Cho and Y.Matsuo.
Electro-optic distributed Bragg reflection
modulator for Integrated Optics.
I.E.E.E. J. Quant. Electr., Vol.QE13(4), 1977,
pp.206-208.

[20] H.F.Schlaak, A.Neyer and W.Sohler.
Electro-optical oscillator using an
Integrated Optic modulator.
Opt. Comm., Vol.32(1), 1980, pp.72-74.

[21] M.Papuchon, M.Courbemale, X.Mathieu, D.B.Ostrowsky, L.Reiber, A.M.Royd, B.Sejourne and M.Werner.
Electrically controlled optical directional coupler:COBRA.
Appl. Phys. Lett., Vol.27(5), 1975, pp.289-291.

[22] H.Sasaki and I.Anderson.
Theoretical and experimental studies on active Y-junctions in optical waveguides.
I.E.E.E. J. Quant. Electr., Vol.QE14(11), 1978, pp.883-892.

[23] C.M.Gee, G.D.Thurmond and H.W.Yen.
17GHz bandwidth electro-optic modulator.
Appl. Phys. Lett.,Vol.43(11), 1983,pp.998-1000.

[24] R.C.Alferness.
Efficient waveguide electro-optic TE-TM mode converter wavelength filter.
Appl. Phys. Lett., Vol.36(7), 1980, pp.513-515.

[25] P.W.Smith, I.P.Kaminow, P.J.Maloney and L.W.Stulz.
Integrated bistable devices.
Appl. Phys. Lett., Vol.33(1), 1978, pp.24-26.

[26] N.Uesugi, K.Daikoku and K.Kubota.
Electric field tuning of second harmonic generation in a three dimensional $LiNbO_3$ optical waveguide.
Appl. Phys. Lett., Vol.34(1), 1979, pp.60-63.

[27] N.Uesugi.
Parametric difference frequency generation in a three dimensional $LiNbO_3$ optical waveguide.
Appl. Phys. Lett., Vol.36(2), 1980, pp.178-181.

[28] L.A.Molter-Orr, H.A.Haus and F.J. Leonberger.
20GHz optical waveguide sampler.
I.E.E.E. J. Quant. Electrs.,Vol.QE19(12),1983, pp.1877-1883.

CHAPTER 2

THE THEORETICAL CHARACTERISATION OF OPTICAL WAVEGUIDES.

2.0 INTRODUCTION

This chapter provides a comparison of the analysis techniques available to compute the propagation characteristics of optical waveguides with confinement in two dimensions. Being able to predict the behaviour of such structures accurately facilitates the initial design of more complex components e.g. directional couplers, ring-resonators, and Y-junctions where single-mode operation is necessary, without the need to perform extensive experimental investigations. Several excellent review articles describe the various numerical and approximate methods available for analysing waveguides e.g. Yeh et al. [1] and Wexler [2].

Several methods are described and comparisons are made of their accuracy and ease of implementation for a specific waveguide geometry and refractive index distribution. Of special interest for the design of the standing wave modulator is the influence of thin metal films upon the optical mode cut-off dimensions of the optical waveguide. In particular, the changes in the propagation characteristics of an optical field due to the presence of a metal film are addressed with a view to choosing a metal which produces the minimum attenuation.

2.1. DERIVATION OF THE WAVE EQUATION FOR DIELECTRIC WAVEGUIDES.

The behaviour of an electromagnetic field propagating in a region composed of several dielectric layers can be

described by Maxwell's Curl Equations. For a time harmonic field in a non-magnetic, isotropic, source-free medium with arbitrary dielectric constant they take the form [3]:

$$\nabla \times \underset{\sim}{E} = j\omega\mu_0 \underset{\sim}{H} \tag{2.1a}$$

$$\nabla \times \underset{\sim}{H} = -j\omega\epsilon_0\epsilon(r)\underset{\sim}{E} \tag{2.1b}$$

In the classical derivation of the Wave Equation describing the propagation of an electromagnetic field in a dielectric medium the curl of Equ.(2.1a) is taken and the resulting expression is substituted into Equ.(2.1b). On application of the standard curl identity:

$$\nabla \times (\nabla \times \underset{\sim}{A}) = \nabla(\nabla \cdot \underset{\sim}{A}) - \nabla^2 \underset{\sim}{A} \tag{2.2}$$

the expression below then follows in terms of the electric field:

$$-\nabla(\nabla \cdot \underset{\sim}{E}) + \nabla^2 \underset{\sim}{E} = -\omega^2\mu_0\epsilon_0\epsilon(r)\underset{\sim}{E} \tag{2.3}$$

If the dielectric constant is uniform then the first term in Equ.(2.3) is zero and then Equ.(2.3) reduces to the standard form of the Wave Equation or the Helmholtz form. For a situation where there is some variation of $\epsilon(r)$ then $\nabla \cdot \underset{\sim}{E}$ is not zero but is equal to $-\underset{\sim}{E}\frac{\nabla\epsilon(r)}{\epsilon(r)}$. Depending on the magnitude of the variation in the dielectric constant it may be possible to approximate this contribution to zero, and obtain the Wave Equation. If a spatial variation in the Z- direction of the form $e^{-j\beta z}$ is assumed, then Equ.(2.3) can be re-written as:

$$\nabla_T^2 \underset{\sim}{E} - (\beta^2 - \omega^2\mu_0\epsilon_0\epsilon(r))\underset{\sim}{E} = 0 \tag{2.4}$$

where ∇_T^2 is the two dimensional Laplacian operator. A similar expression may be derived for the Wave Equation for the H field if the curl of Equ.(2.1b) is taken first of all and then substituted into Equ.(2.1a). No ambiguity arises concerning the term $\nabla.\underset{\sim}{H}$ because the permeability is assumed to be constant throughout the region.

A solution is sought for the electric field E which obeys Equ.(2.4) in all of space and also conforms with the boundary conditions imposed by the optical waveguide geometry. In certain cases, exact solutions of a simple functional form exist for the problem, but, in general, for more complicated configurations,accurate solutions are only available through numerical computation. However, a variety of approximate methods for analysing optical waveguides with a two-dimensional refractive index variation have been developed which incorporate the results from the exact analysis for one dimensional slab waveguides.

2.2 THE DIELECTRIC SLAB OPTICAL WAVEGUIDE.

The simplest one dimensional structure that can be analysed exactly is the slab dielectric waveguide comprising three dielectric regions infinite in extent along the X- and Z- direction as shown in Fig.2.1. The central layer has an optical dielectric constant ϵ_2 which is surrounded above and below by regions with optical dielectric constants ϵ_1 and ϵ_3. The magnitude of the dielectric constants of the surrounding media are less than that of the central region.

The derivation of the eigenvalue equation defining the propagation constants of the discrete modes of the waveguide originates from the solution of the Helmholtz

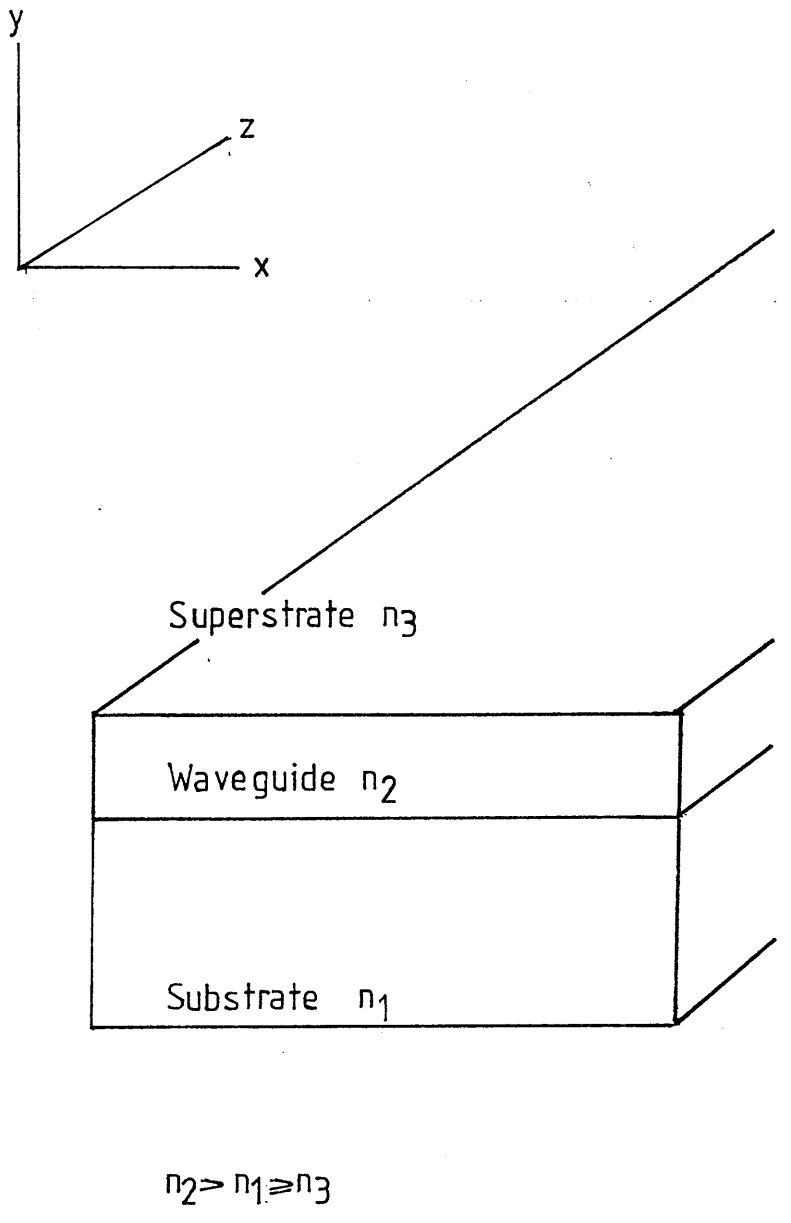

FIG.2.1. The dielectric slab waveguide.

form of the Wave Equation [4]. The solutions found for these fields are subject to the boundary conditions and the physical realisability of the problem.

Starting from Equ.(2.1a) and Equ.(2.1b) with the assumption that the field has both harmonic time and spatial dependence, two sets of independent equations are found. In these sets of equations, two dependent field components are expressed solely as a function of the third field component. These equations describe the two types of wave polarisation which the waveguide can support, and are classified as TE- and TM- waves. For TE- waves the field components Hx and Hy are expressed in terms of Ey and for TM waves Ex and Ey are expressed in terms of Hy. These generating functions themselves satisfy the one-dimensional Wave Equation from which the field distribution is obtained.

As an example, the solution of the Wave Equation for TE- polarised waves will be considered. The Wave Equation for the generating field is again the Helmholtz form:

$$\frac{d^2E_4}{dx^2} + (n_i^2 k_o^2 - \beta^2) = 0 \qquad (2.5)$$

where:

$$\epsilon_i = n_i^2 \quad : i = 1, 2, 3 \qquad (2.6)$$

and:

$$k_o^2 = \omega^2 \mu_o \epsilon_o = \frac{\omega^2}{c^2} = \left(\frac{2\pi}{\lambda_o}\right)^2 \qquad (2.7)$$

A field distribution is now sought which constitutes a guided mode. The general form of the distribution may be

arrived at through simple physical arguments. For instance, the energy of a guided mode should be finite and be bound in the vicinity of the dielectric material with the largest dielectric constant, which suggests that the field should possess an exponential decay with distance away from the high refractive index region. Within the region of high refractive index the field distribution will vary harmonically.

Expressing these concepts mathematically leads to the following field expressions for each of the layers. Each distribution has a form which intrinsically is a solution of the Wave Equation. In region 1 of Fig 2.1 Equ.(2.5) has the solution:

$$E_y(x) = A.\exp(-\gamma_1 x) \quad : \gamma_1^2 = \beta^2 - k_o^2 n_1^2 \tag{2.8}$$

and similarly for regions 2 and 3 of Fig.2.1:

$$E_y(x) = B_1.\exp(-j\gamma_2 x) + B_2.\exp(j\gamma_2 x) : \gamma_2^2 = k_o^2 n_2^2 - \beta^2 \tag{2.9}$$

$$E_y(x) = C.\exp(\gamma_3 x) \quad : \gamma_3^2 = \beta^2 - k_o^2 n_3^2 \tag{2.10}$$

The solutions correspond to situations where the quantity $(k_o^2 n_i^2 - \beta^2)^{1/2}$ is either real or imaginary. If it is real then evanescent fields exist which decay exponentially away from the guiding layer. For imaginary values sinusoidal solutions exist which indicate an unattenuated guided mode.

From the above expressions for the Ey field distribution the other field components may be generated. The pre-exponential terms are evaluated by ensuring the continuity of the tangential component of the electric field and the magnetic field across the interface. The

second condition is equivalent to the derivative of the electric field being continuous across the interface.

Applying these boundary conditions to determine the pre-exponential term leads to the eigenvalue equation giving the propagation constant β, of the guided modes. The derivation may be found in any standard text on dielectric waveguides and only the result will be stated here. For TE-modes the eigenvalue equation is:

$$2\gamma_2 d - \arctan\left(\frac{\gamma_1}{\gamma_2}\right) - \arctan\left(\frac{\gamma_3}{\gamma_2}\right) = m\pi \qquad (2.11)$$

The determinantal equation for TM-modes is of a similar but slightly more complicated form:

$$2\gamma_2 d - \arctan\left(\frac{\gamma_1 n_2^2}{\gamma_2 n_1^2}\right) - \arctan\left(\frac{\gamma_3 n_2^2}{\gamma_2 n_3^2}\right) = m\pi \qquad (2.12)$$

where γ_1, γ_2, and γ_3 have been defined earlier. It can be deduced from Equ.(2.11) that for a symmetric slab waveguide i.e. one where $n_1=n_3$, there is no cut-off wavenumber for the fundamental TE mode. In this situation the propagation constant of the guided mode approaches that for a plane wave propagating in the surrounding media.

2.3. APPROXIMATE METHODS OF ANALYSING WAVEGUIDES WITH TWO DIMENSIONAL VARIATION OF REFRACTIVE INDEX PROFILE.

The propagation characteristics of a guided mode confined in a dielectric waveguide of rectangular geometry which possesses a refractive index profile that varies in not one but two dimensions cannot be analysed exactly. The analysis of these two dimensional dielectric waveguides requires recourse to a variety of numerical approximations some of which utilise the exact

determinantal equation for a slab waveguide.

One of the first attempts to describe the modes supported by a two dimensional dielectric waveguide was carried out by Marcatili [5]. In his formulation, the optical waveguide is rectangular in shape and surrounded by either a rarer medium of refractive index n_1 or embedded in a rarer medium of refractive index n_1 with n_3 at the top interface (Fig.2.2). The modes supported within the waveguide are classified as E^x_{pq} and E^y_{pq} in his analysis, where the superscript indicates the direction along which the electric field is most prominent. The subscript relates to the number of extrema which the dominant electric field component has within the waveguide.

As an example, for the E^x_{pq} modes, the field component E^x plays the role of the generating function and obeys the two dimensional Wave Equation:

$$\frac{\partial^2 E^x}{\partial x^2} + \frac{\partial^2 E^x}{\partial y^2} + (n_i^2 k_o^2 - \beta^2) E^x = 0 \qquad (2.13)$$

The magnitude of E^x_{pq} is then a function of both the X- and the Y- co-ordinates and may therefore be stated mathematically as the product of separate X-and Y-dependent functions:

$$E^x(x,y) = E^x(x).E^x(y) \qquad (2.14)$$

so that on substitution into Equ.(2.13):

$$E^x(y).\frac{d^2E^x(x)}{dx^2} + E^x(x).\frac{d^2E^x(y)}{dy^2} + (n_i^2 k_o^2 - \beta^2) E^x(x) E^x(y) = 0 \qquad (2.15)$$

which can be separated into two second order differential equations:

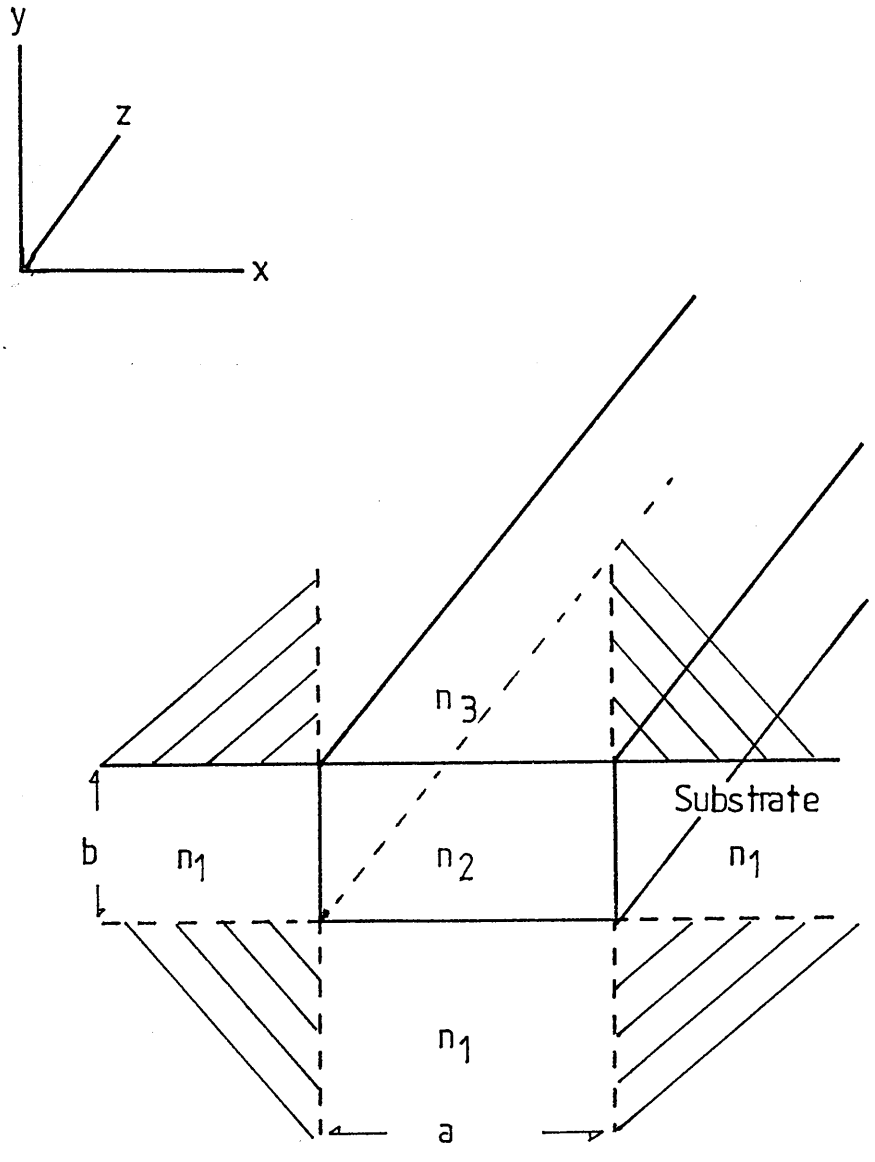

FIG.2.2. The dielectric rectangular waveguide.

$$\frac{d^2E^x(x)}{dx^2} = k_x^2 E^x(x) \qquad (2.16a)$$

$$\frac{d^2E^x(y)}{dy^2} = k_y^2 E^x(y) \qquad (2.16b)$$

where:

$$k_x^2 + k_y^2 + \beta^2 = k_o^2 n_1^2 \qquad (2.17)$$

The equations Equ.(2.16a) and Equ.(2.16b) now resemble the Wave Equation for a slab waveguide, transverse respectively in the X- and Y- directions with kx and ky being the transverse propagation constants for the equivalent infinite slab waveguide. The values of kx and ky are found by solving the determinantal equation for the slab dielectric waveguide Equ.(2.11) or Equ.(2.12), for the correct polarisation. The longitudinal propagation constant for the composite rectangular dielectric waveguide is then simply found from substitution of these constants into Equ.(2.17).

The approximations inherent in following this procedure are as follows. The mode is assumed to be well confined so that most of the energy is contained within the rectangular region of Fig.2.2. From this assumption it follows that the fields in the shaded regions are neglected. The mathematical solution of the Wave Equation by the method of separation of variables is only strictly true when the fields are not perturbed by each other; that is they are not coupled to each other. This again is only true to a good approximation when the fields are well confined in the rectangular dielectric waveguide. The accuracy of this method deteriorates when the above conditions are not fulfilled, i.e. principally when the mode is close to the cut-off condition. As this point is

reached a greater proportion of the energy lies outwith the guiding region in the evanescent fields. The propagation constants obtained for the equivalent slab structure do not take into account the field that may be present in the other region (Fig.2.2).

Neglecting the penetration of the field into the shaded regions leads to a larger value for the transverse propagation constants, kx and ky. Substitution of these constants into Equ.(2.17) consequently produces a smaller value for the longitudinal propagation constant when compared with other more accurate methods [6].

It has been shown by Kumar et al. [7] that, by applying a perturbation approach, greater accuracy can be achieved by this type of variable separation technique.

2.3.1. THE EFFECTIVE INDEX METHOD.

In an attempt to overcome the over-estimation problem of the cut-off propagation constant associated with Marcatili's analysis, the effective index method was developed by Knox and Toulios [8] for the analysis of microwave dielectric waveguides. The method provides a convenient means of incorporating the coupling effects between the orthogonal components of the fields which are assumed independent in the Marcatili method. Instead of using the absolute refractive index when calculating the second orthogonal propagation constant, the effective index found for the first equivalent transverse slab structure is used. The modification couples the two initially independent propagation constants together although the field penetration into the shaded areas of Fig.2.2 is still implicitly ignored.

A problem inherent with the effective index method is the choice of the order in which the two orthogonal propagation constants are calculated i.e. whether the propagation constant for the equivalent vertical or horizontal slab is calculated first. For small index changes this difference is not significant. However, for larger index changes and greater degrees of asymmetry in the dielectric layers the order of calculation does have a marked effect, with up to a 10% variation between the calculated propagation constants [9]. The propagation constant for the equivalent transverse slab which exhibits the least confinement is calculated first as it is the most sensitive to the index change and waveguide dimension.

The effective index method has proved to be a very versatile technique because it can be modified easily to include non-step refractive index profiles and other optical waveguide geometries e.g. rib and strip loaded structures[10]. But once the waveguide geometry deviates from the general rectangular form, the implementation of this method becomes cumbersome [11]. Both the effective index and the separation of variables methods can accommodate the additional problem of the inclusion of complex dielectric constants, that permits the effect of a lossy medium upon the propagation constants to be evaluated. Of particular interest for integrated optics is the modification of the propagation characteristics of a confined optical field by the presence of a metal film. A situation of particular importance is the case of a metallic electrode pattern close to an optical waveguide, as used in an active device.

2.3.2 THE TRANSVERSE RESONANCE METHOD.

A similar method of analysis to the effective index method is the transverse resonance method [12]. It is based upon a principle commonly employed in analysing microwave structures and uses concepts found in Transmission Line theory. When it is generalised to the two dimensional rectangular waveguide it is equivalent to the effective index method.

As an illustrative example, the determinantal equation will be found for the asymmetric slab waveguide. It is assumed that the waveguide is continuous in the Y- and Z- directions. As the name implies, a direction transverse to the direction of propagation is considered in order to derive the eigenvalue equation and for this example the X- direction is taken. The propagation constants for a plane wave travelling in this direction in each medium are respectively γ_3, $j\gamma_2$ and γ_1. The wave impedance of a plane wave (for a TE-mode) in a homogeneous medium is $\frac{\omega\mu_0}{\beta}$ whereas that for a TM-mode is $\frac{\beta}{\omega\epsilon_0\epsilon_r}$ where β is the effective propagation constant. In the slab dielectric waveguide, for a TE-mode, the magnetic field is in the 'resonant' direction so the wave impedance is given by $\frac{\omega\mu_0}{\beta}$ in each region. The wave impedance must be a real quantity in the guiding region and an imaginary quantity in the cladding regions, because of the restriction on β for each region.

The equivalent circuit representing this structure is shown in Fig.2.3. The transverse resonance method requires that the impedance at plane aa' (Fig.2.3) is either zero for the loss-less case or purely real for the lossy situation. The substrate impedance $Z_3 = \frac{\omega\mu_0}{j\gamma_3}$ has to be referred to the plane aa' and this is accomplished by

the standard expression used for transmission lines i.e.:

$$-\frac{\omega\mu_0}{j\gamma_1} + \frac{\omega\mu_0}{\gamma_2}\left[\frac{\frac{\omega\mu_0}{j\gamma_3} + j\frac{\omega\mu_0}{\gamma_2}\tan 2\gamma_2 d}{\frac{\omega\mu_0}{\gamma_1} + \frac{\omega\mu_0}{\gamma_3}\tan 2\gamma_2 d}\right] = 0 \qquad (2.18)$$

After some rearrangement Equ.(2.18) may be expressed as:

$$\tan 2\gamma_2 d = \frac{\frac{\gamma_3}{\gamma_2} + \frac{\gamma_1}{\gamma_2}}{1 - \gamma_3\gamma_1/\gamma_2^2} \qquad (2.19)$$

which should be compared with Equ.(2.11). A similar expression for TM-modes may be derived for Equ.(2.12) in exactly the same manner, but by using the TM-mode impedance in the resonant direction. This method has particular application in the analysis of rib waveguides, where it is used in conjunction with an equivalent circuit representation for the step discontinuity first proposed by Oliner et al. [13] in the analysis of surface acoustic wave devices and later developed for optical structures by Koshiba et al. [14,15,16].

The effective index may be used in analysing this structure by obtaining the propagation constants for TE modes in regions I and II (Fig.2.4). These regions are assumed to be infinite in the transverse direction for this purpose. The effective index for each region is used to form a composite structure in the x- direction in which the propagation constant for a TM- mode is found. The value is then an approximation to the actual longitudinal propagation value.

The step discontinuity in the resonant direction is modelled by an ideal transformer of turns ratio 'n' connected in parallel with a susceptance to represent the junction. The turns ratio is calculated by equating the modal fields expansion at the interface for the two slab regions. The transverse resonance method is then applied

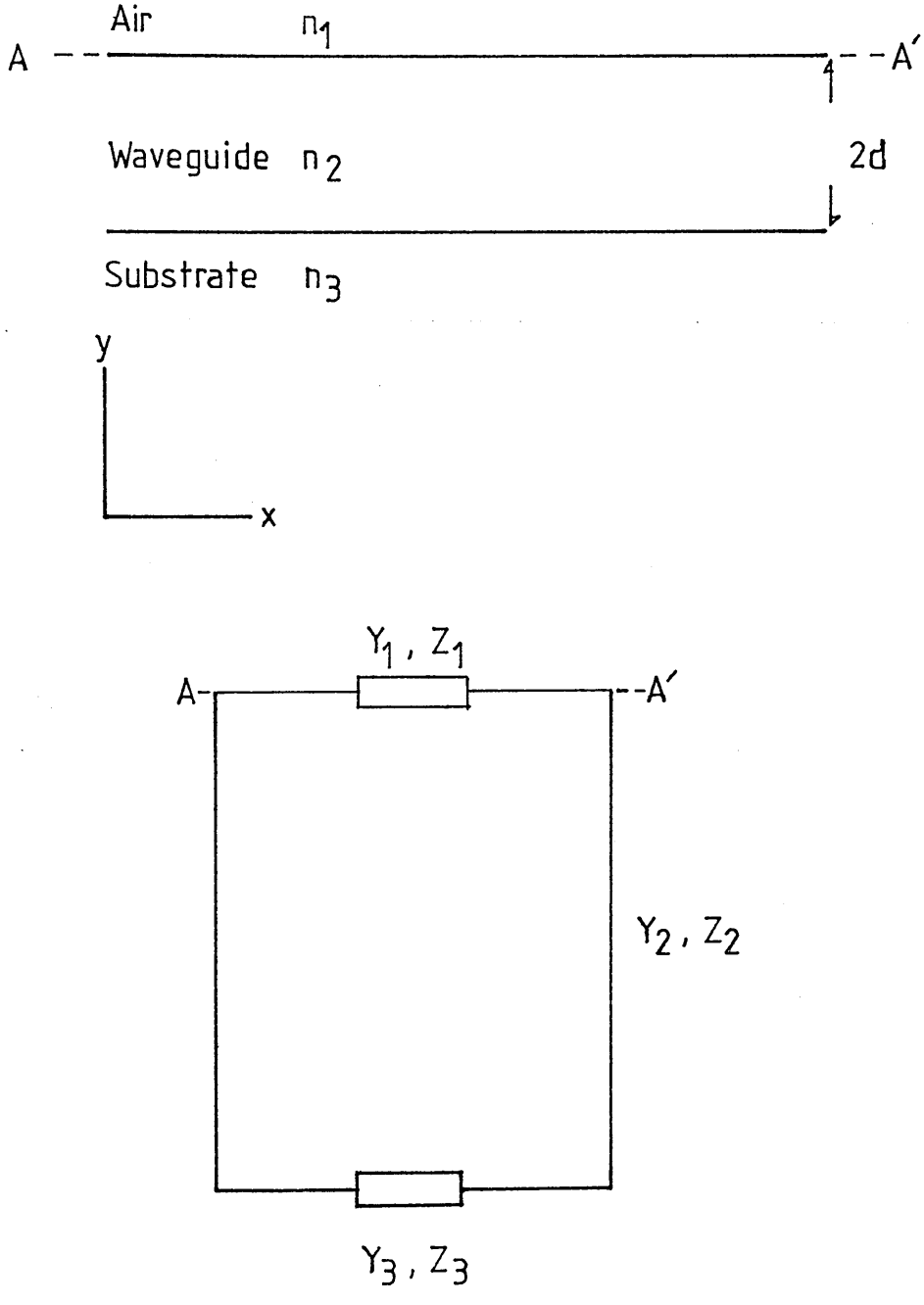

Transmission Line Representation

FIG.2.3. The transverse resonance technique.

to the structure shown in Fig.2.4. The middle of the rib can be taken as a plane of symmetry; either a magnetic or an electric short circuit is assumed to exist there. The magnetic short circuit corresponds to the fundamental mode.

For TE-like modes, the wave impedance in each region is given by $\frac{\omega\mu_0}{\beta}$, where β is the propagation constant for the same order of mode in each region. The eigenvalue value equation for this condition is found by equating the impedance at the plane of the rib edge for the infinite slab to the transferred short circuit impedance at the centre of the rib structure.

The accuracy of the above is better than that of the effective index method alone, for rib type structures, because some attempt is made to match the fields at the boundary. It arises from expression of the modes in each region as an infinite sum of normal modes for that region. An attempt is then made to match the tangential and normal fields of each expansion term in the infinite series at the boundary. In the method only the first terms are used. However, the propagation constant k_x used for each isolated planar structure to give the wave impedance assumes that the lateral confinement does not affect the longitudinal propagation constant. For large aspect ratio structures it is a valid approximation but the validity is questionable for structures less than a few wavelengths wide.

For both the effective index and the transverse resonance methods, region II is assumed to support a mode. If this condition is not fulfilled, then the bulk propagation constant for the superstrate material has to be used. Dagli et al. [17] have reported developments

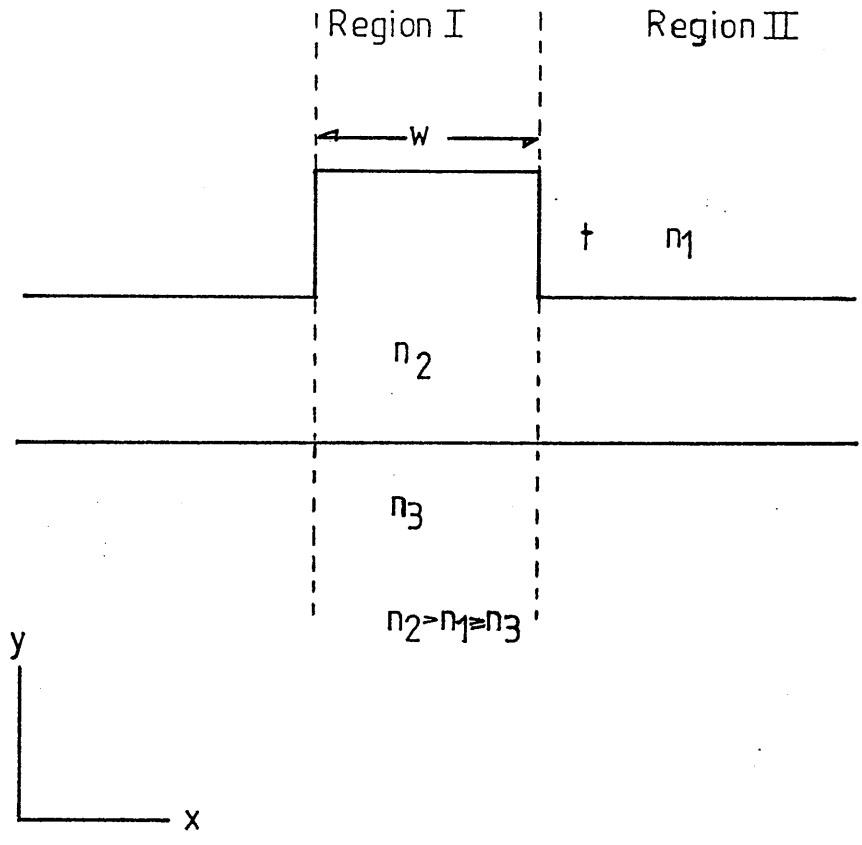

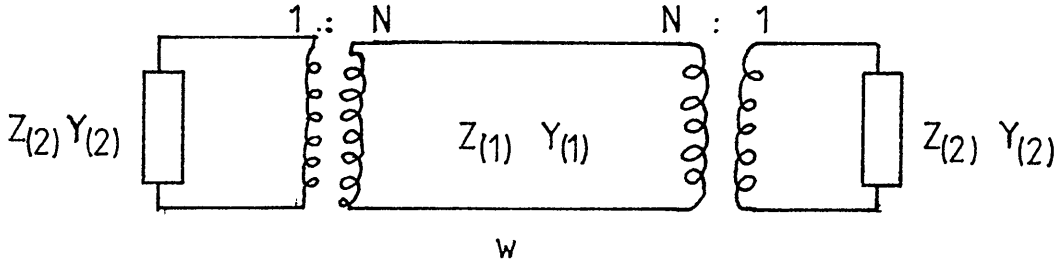

$$E_x \text{ Modes } Z = \frac{\omega \mu . k_x}{\beta^2}$$

$$E_y \text{ Modes } Z = \frac{\beta^2}{\omega \epsilon k_x}$$

$$k_x^2 + k_z^2 = \beta^2$$

FIG.2.4. The transverse resonance representation of a rib waveguide.

whereby the propagation constants of the higher order modes may be found.

2.4 NUMERICAL METHODS FOR SOLVING THE TWO DIMENSIONAL WAVE EQUATION.

The methods described above have all been intuitive approximations based on the exact analysis of the infinite slab waveguide. In this section, true numerical methods will be described in some detail. There are several review articles describing these methods in detail e.g. Wexler [2]. Such methods do not rely upon some approximate representation for the waveguiding structure, but rather provide numerical solutions of the Wave Equation for the structure capable, in principle, of indefinite refinement to give any level of accuracy required. Two methods will be described, both of which require the use of at least a mini-computer for computation; one is based on a finite-difference representation of the Wave Equation and the other, on a variational approach. These are not the only numerical methods: the finite element method provides the greatest degree of accuracy as it solves the vector Wave Equation to find true hybrid modes, which is explained in more detail in refs.[18,19,20].

2.4.1. SOLUTION OF THE TWO DIMENSIONAL WAVE EQUATION WITH KNOWN INDEX DISTRIBUTION BY FINITE-DIFFERENCES.

To illustrate the approach adopted in each method for calculating the propagation constant for optical waveguides, Equ.(2.3) is taken as the starting point. The usual assumptions of a non-magnetic, isotropic, source free medium still apply. There is some flexibility as regards the isotropy of the medium: an anisotropic medium

can be analysed but necessitates the use of a matrix representation for Equ.(2.3). For a dielectric structure with no free charge carriers, $\nabla \cdot \underset{\sim}{D} = 0$ where $\underset{\sim}{D} = \epsilon_o \epsilon(r) \underset{\sim}{E}$. However, the dielectric distribution may be a function of both transverse co-ordinates and is therefore expressed as:

$$\epsilon(r) = \epsilon_r(x,y) \tag{2.20}$$

Then:

$$\nabla \cdot D = \epsilon_o \left(\epsilon_r(x,y) \nabla \cdot E + \underset{\sim}{E} \cdot \nabla(\epsilon_r(x,y)) \right) = 0 \tag{2.21}$$

and therefore:

$$\nabla \cdot \underset{\sim}{E} = - \frac{1}{\epsilon_r(x,y)} \underset{\sim}{E} \cdot \nabla(\epsilon_r(x,y)) \tag{2.22}$$

In the case of dielectric optical waveguides, the gradient of the dielectric constant term is often assumed to be so small that it can be ignored. For small index variations this is usually taken as a valid assumption, but Haus [21] has questioned the validity of this assumption and suggests that a vector potential be used instead. A quasi-TE mode is now assumed, indicating that the field component Ey is appreciably greater than the Ez component. The Ez component is taken to be approximately zero, which then reduces the Wave Equation to the standard Helmholtz form:

$$\frac{\partial^2 E_x}{\partial x^2} + \frac{\partial^2 E_x}{\partial y^2} + (k_o^2 n^2(x,y) - \beta^2) E_x^2 = 0 \tag{2.23}$$

which is essentially identical to Equ.(2.4), but has explicit (x,y) dependence.

The differential operators in this technique are

replaced by a finite difference representation. The first partial derivative of a function denoted by f at a point x is approximately equal to:

$$f'_x = (f_{x+h} - f_{x-h})/2h \qquad (2.24)$$

where h may be made as small as necessary. In the limit $h \to 0$ Equ.(2.24) approaches the exact partial derivative. The derivative of f at a point (x+h) is simply:

$$f'_{x+h/2} = (f_{x-h} - f_x)/h \qquad (2.25)$$

The second derivative is given approximately by the difference of the first order derivatives:

$$f''_x = (f'_{x+h/2} - f'_{x-h/2})/h \qquad (2.26)$$

$$f''_x = (f_{x+h} + f_{x-h} - 2.f_x)/h \qquad (2.27)$$

The Laplacian operator may then be approximated by the following finite-difference representation for an arbitrary function f(x,y) which, for f(x,y) real, must be infinitely differentiable at x,y.:

$$\left.\frac{\partial^2 f(x,y)}{\partial x^2}\right|_{x_0,y_0} + \left.\frac{\partial^2 f(x,y)}{\partial y^2}\right|_{x_0,y_0} = \frac{f(x_0+h,y_0)+f(x_0-h,y_0)-2f(x_0,y_0)}{h^2} + \frac{f(x_0,y_0+h)+f(x_0,y_0-h)-2f(x_0,y_0)}{h^2} \qquad (2.28)$$

Once more, as h tends to zero, Equ.(2.28) tends towards the exact derivative. From Equ.(2.28), if the field surrounding some point is known at adjacent nodes then the second order derivatives may be calculated easily. To aid the actual numerical evaluation of Equ.(2.28) the distance, h, between adjacent nodes need not be the same for the X- and Y- directions. There is however, some increase in the program complexity if this option is used [22].

The refractive index distribution has also to be expressed as a discrete variation for each point in the region of interest. The Wave Equation in finite difference form then becomes:

$$\frac{E_x(I+1,J)+E_x(I-1,J)-2E_x(I,J)}{(\Delta x)^2}+\frac{E_x(I,J+1)+E_x(I,J-1)-2E_x(I,J)}{(\Delta y)^2}=-k_o^2E_x(I,J)(N^2(I,J)-N^2) \quad (2.29)$$

where $N(I,J)$ is the index distribution at the mesh point and $\Delta x,\Delta y$ represent the distance between adjacent points in the X- and Y- directions respectively. In order to find a minimum value for the effective index a stationary form for Equ.(2.29) has to be used.

A minimisation procedure for N from Equ.(2.29) can be derived by multiplying Equ.(2.4) scalarly by Ex and then integrating throughout all space, which yields:

$$N^2k_o^2 \leq \int_V \left(\nabla_T^2 E_x + k_o^2 N^2(I,J)\right) E_x \, dV \Big/ \int_V E_x^2 \, dV \quad (2.30)$$

If there is no confinement in the propagation direction the volume integral can be replaced by a double integral. This expression can be shown to be stationary by replacing the exact field Ex by the approximation E_x+pe_x and differentiating the expression with respect to p. After extensive vector manipulation the expression (see for example ref.[4]):

$$\frac{\partial(k_o^2N^2)}{\partial p} = -\frac{2\oint_S (\underset{\sim}{e}_x \times \nabla_T \times \underset{\sim}{E}_x)\cdot d\underset{\sim}{S}}{\int_V \epsilon |\underset{\sim}{E}_x|^2 \, dV} \quad (2.31)$$

is obtained. This expression is zero for any guided mode because the term $\underset{\sim}{e}_x \cdot d\underset{\sim}{S}$ is equal to zero if the surface chosen is sufficiently large, so that the field at the boundary is approximately zero. The numerical evaluation of the terms in Equ.(2.30) is relatively

straight forward with the integration done by the trapezoidal method or some other more advanced method if the computing capacity exists.

An initial guess is made for the field distribution which is subsequently iterated to provide a new value of N from Equ.(2.30). To speed up the relaxation process, successive over relaxation is employed. A fuller description is given by Carree [23]. The updated value of the electric field at each node is then overcorrected using an acceleration factor. After each iteration of the field has been carried out, Equ.(2.30) is evaluated to provide a new value of the effective index. The process is performed until the subsequent values obtained for N have converged. It should be noted that Equ.(2.30) will always produce values for N that are above the true absolute value, a problem common to the variational approach. Conceptually, by the prudent choice of mesh size and boundary conditions, the over estimation inherent from Equ.(2.30) may be made as small as possible.

The most attractive feature of solving the Wave Equation by finite differences is that any waveguide geometry with arbitrary index can, at least in principle, be analysed easily. The drawback with this particular technique is that at least a mini-computer must be employed to produce values for the effective index in a reasonable period of time. Special attention must be paid to ensure that the boundary conditions [24,25] used are an accurate representation of the physical situation. A particular problem was considered by Robertson et al. [26], although they did not clearly explain the conditions imposed at the boundaries. Care must be exercised in forcing the field at the boundary of

the total region of interest to zero and in accounting correctly for the discontinuities at the corners. This can affect the effective refractive index by up to 1-2%, as Robertson et al. [26] demonstrated.

Ideally, the value of the field at the edge of the box containing the region in which the Wave Equation is to be solved should correspond to the field being zero at infinity. If it were possible to implement such boundary conditions, the size of the box would be immaterial, with the error in the effective index arising simply from the separation between adjacent mesh points. The box would act as a window in a particular region in space, the interior of which would correspond to the unique solution for all of space.

In practice, the fields at the box edges are forced to some predetermined value: the most common condition being to force the field to zero at the boundary of the box, which is justified by choosing a box of sufficient size that the field has decayed almost to zero. However, by using the method described by Cermak et al. [24] it becomes unnecessary to have such a large box. Even first order interpolation can improve dramatically the calculated value of the effective index when compared with intrinsically more accurate methods,as will be described later.

The drawbacks associated with incorpating these more sophisticated boundary conditions are the increased complexity in the coding and the increased computational time. Nevertheless a point may be reached where the inclusion of such techniques to fix the boundary values can lead to a saving in the time required before overall convergence is achieved.

2.4.2. SOLUTION OF THE WAVE EQUATION BY THE RAYLEIGH-RITZ METHOD.

The Rayleigh-Ritz variational technique can also be employed in the numerical solution of Equ.(2.23) [27]. It differs from the finite difference method in that the approximation to the exact field is given by the summation of a series of trial functions, the coefficients of which are individually adjusted to give a stationary value for the propagation constant. In the finite-differences formulation, an initial distribution is assumed which is subsequently corrected until there is little variation in it. In the Rayleigh-Ritz method, the functions should, in the first instance, be a reasonable approximation for the actual field distribution. A sensible choice of basis functions will ensure that the summation converges rapidly. The most frequently used in this method are those classed as Hermite-Gaussian functions which describe the field distribution within a semi-conductor laser cavity. These are chosen because they form an orthogonal set of functions which are infinitely differentiable and tend to zero at $X \to \infty$:

$$D_n(X) = (-1)^n \cdot \exp\left(\frac{X^2}{4}\right) \cdot \frac{\partial^n}{\partial X^n}\left\{\exp\left(-\frac{X^2}{2}\right)\right\} \qquad (2.32)$$

the exact field distribution is then approximated by a linear combination of the products of the above functions, assuming that the X- and Y- dependence are separable variables:

$$E_x(X,Y) = \sum_{ij} \alpha_{ij} D_i\left(\frac{X}{s}\right) \cdot D_j\left(\frac{Y}{\eta}\right) \qquad (2.33)$$

The computational problem involves the determination of the variable coefficients α_{ij} of each combination such

that the variational expression:

$$\frac{\partial(k_0^2 N^2)}{\partial \alpha_{ij}} = 0 \qquad (2.34)$$

simultaneously for all i,j. As this condition is reached for each product, the summation is assumed to approach the exact field distribution. It can be shown, [26], that the calculated value for the effective index is a lower bound to the actual value.

The accuracy of this method is clearly dependent upon the number of basis functions that are used in each direction. For structures which exhibit symmetry, the number of functions in the symmetry direction is typically small. For structures which exhibit a sudden index change and a large geometrical asymmetry, a considerable number of trial functions is necessary to take accurate account of the field variation. Of course, an increase in accuracy is offset by the additional computational effort involved.

The index profile describing the waveguide geometry has to be represented by points on a mesh and this may lead to an error in the calculation arising fron the finite spacing between points. The index change between various regions may occur between adjacent nodes, leading to an error in the actual waveguide dimensions. Boundary conditions can substantially shift the value of the calculated effective index. These effects have been described elsewhere [24].

2.5. COMPARISON BETWEEN EFFECTIVE INDEX, FINITE DIFFERENCE AND VARIATIONAL METHODS FOR ANALYSING RIB TYPE GEOMETRIES.

This section is devoted to comparisons of the calculated propagation constants for various rib type structures formed by etching GaAs/AlGaAs epitaxial layers, using the previously described analysis procedures. The results obtained and the conclusions drawn are applicable, with appropriate modifications, to the other methods of forming optical waveguides - for instance diffused waveguides in $LiNbO_3$. The main aim is to find a method which offers an acceptable degree of accuracy.The variational program used was developed by R.G.Walker et al. [28] at Glasgow University.

Two particular examples are considered in making the comparisons between the various methods. The first is a rib waveguide of fixed width but variable step height, as shown in Fig.2.5. This structure is equivalent to a rib waveguide etched in $GaAs/Al_xGa_{1-x}As$ where x is of the order of 0.20. The second is a buried waveguide, assumed to be rectangular in shape which has various degrees of confinement and aspect ratio. This configuration is similar to one that may be encountered experimentally. It corresponds approximately to either a proton-exchanged waveguide formed in $LiNbO_3$ using an undiluted melt only or one that also has been annealed.

The rib structure has also formed the basis of an analysis carried out by Benson et al. [22] and Austin [29]. The most accurate result is assumed to be that given by the variational method using as many trial functions and as fine a mesh as time reasonably permits (typically of the order of 10mins on a GEC 4180).

From the graph and data shown in Figs.2.5 and 2.6 it can be seen that as the waveguide dimensions approach cut-off, the discrepancy between the values of the effective index found from the different methods increases - the relative error being 0.05%. Only the finite-difference (a mesh spacing of 0.01μm) and the variational method (10x15 basis functions and a mesh spacing of 0.01μm) agree closely with one another as the cut-off condition is approached. It can therefore be assumed that the use of more sophisticated numerical methods is required for the analysis of waveguides close to cut-off, because these methods take into account the field outside the waveguides everywhere rather than ignoring it in certain regions. Methods based on slab approximations may be used with confidence, when the waveguide is well above cut-off to design directional couplers [30]. This condition may be defined as being when the aspect ratio is greater than unity or the index variation between layers is large, which leads to greater confinement.

The results for the embedded waveguide representing a proton-exchanged waveguide are shown in Fig.2.6. Here, as in the previous example, the variational function fitting program is assumed to give the nearest approximation to the actual value. From Fig.2.5b the following may be deduced:

(i) for large aspect ratios and strong confinement the effective index method may be used with confidence although it overestimates the propagation constant,

(ii) for the weakly guiding condition with large aspect ratios the error in the effective index method increases but it gives a better estimate than the variable separation method, and

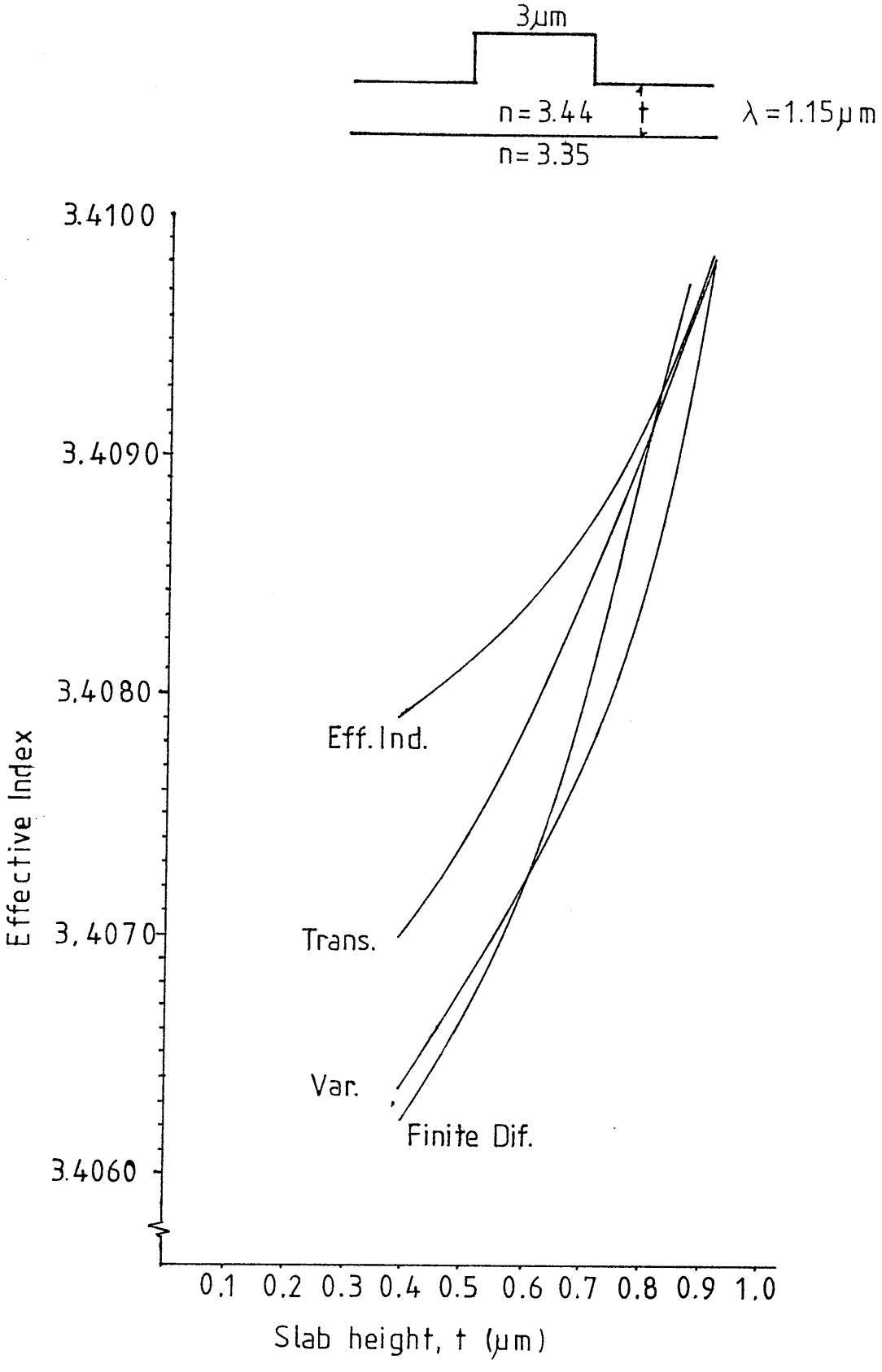

FIG.2.5. Effective index of a rib waveguide.

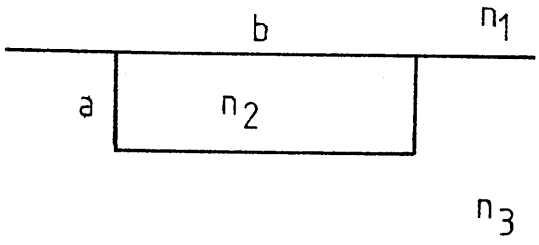

	CASE 1	CASE 2
n_1	1.0	1.0
n_2	2.2500	2.3295
n_3	2.2000	2.2000
a	0.5μm	
b	0.5,2.0μm	0.5,2.0μm
λ_o	0.633μm	

EFFECTIVE INDEX				
b(um)	0.5	2.0	0.5	2.0
Marc.	c.o.	2.2076	2.2414	2.2780
Eff. Ind.	2.2013	2.2044	2.2497	2.2799
Mod. E.I.	c.o.	2.2003	2.2488	2.2796
Wave.	c.o.	c.o.	2.2484	2.2782

FIG.2.6. Effective index of an embedded waveguide.

(iii) the modified effective index, in all cases, gives better agreement with the results obtained from the variational method.

2.6. EFFECT OF THIN METAL OVERLAYS UPON THE GUIDED OPTICAL FIELD.

The other important configuration analysed involves the modification of the propagation constant due to the proximity of a thin metallic film, which occurs, for example, in devices where the metallic electrode structure overlays the waveguide to provide active control of optical devices. The choice of the material for the metal electrode film and, indeed its thickness, has a marked effect upon the characteristics of the optical field within the waveguide.

2.6.1. INTRODUCTION.

It has been observed that a guided wave can propagate along the interface between a metallic layer and a dielectric material; this is the surface plasmon wave which arises due to the negative real part of the complex dielectric constant associated with a metal [31,32]. This particular type of wave has a TM-distribution, for an infinite dielectric layer, and decays exponentially away from the interface in both media. For metals, with a complex refractive index, the TM wave propagation is heavily attenuated.

Devices may be designed which exploit this phenomenon, e.g. mode-filters and polarisers [33,34]. The calculation of the propagation constant, in the first instance, for a slab dielectric waveguide with a thin metal overlay involves a modification to equations Equ.(2.11) and

Equ.(2.12) and has been analysed by several researchers [35,36,37,38]. However, in these papers some confusion has arisen concerning the designation of the modes in each structure and the variation of the attenuation [39].

It has been tacitly assumed that all the values for the refractive indices are real but in practice this need not necessarily be the case. The refractive index in metals must be described by both a real and an imaginary part. Care has to be taken when employing values found in the literature because several different conventions are used and the value will depend on the manner in which the metal is deposited. The most common nomenclature for the refractive index is:

$$n = n' + jk \qquad (2.35)$$

where k is the extinction coefficient and $k < 0$, which may also be written as:

$$n = n'(1 + jk') \qquad (2.36)$$

where k' is now a scaling factor.

The modification of the refractive index to incorporate the imaginary part of the dielectric constant complicates the evaluation of Equ.(2.11) and Equ.(2.12) which now involve the simultaneous solution of both the real and the imaginary parts, to give the real and imaginary components of the propagation constant. The real part of the propagation constant then corresponds to the phase constant and the imaginary part to the attenuation constant.

An important situation arises where the metal film

covering a dielectric slab waveguide is of a finite thickness comparable to the skin depth at optical frequencies. For the analysis of this four layer problem, the eigenvalue equation can be derived by applying the transverse resonance method to the structure in the Y-direction Fig.2.7. This results in the following expression given in [37]:

$$k_{x3}\,b = \arctan\left\{\frac{K_{31}\cdot j\frac{k_{x1}}{k_{x3}} - K_{32}\cdot\frac{k_{x2}}{k_{x3}}\tan k_{x2}.h}{1 + K_{21}\cdot j\cdot\frac{k_{x1}}{k_{x2}}\cdot\tan k_{x2}.h}\right\} + \arctan\left\{K_{34}\cdot j\cdot\frac{k_{x4}}{k_{x3}}\right\} + N\pi \quad (2.37)$$

where:

$$K_{ij} = \begin{cases} 1 & \text{for TE-modes} \\ \frac{\epsilon_i}{\epsilon_j} & \text{for TM-modes} \end{cases} \quad (2.38)$$

and:

$$k_{xi}^2 = k_i^2 - k_z^2$$
$$k_i^2 = n_i^2 k_o^2 \quad (2.39)$$

can be complex. Using this expression, the effects of a metal layer upon the propagation constant can readily be obtained for a range of different metals and thicknesses.

In Fig.2.8, the computed variations in the phase and attenuation constants at 0.633μm are presented for the lowest order TE- and TM- modes as a function of the metal thickness. This situation corresponds to a proton-exchanged planar waveguide in z-cut $LiNbO_3$ 0.5μm deep where the refractive indices of the film and substrate are 2.3 and 2.2 respectively. In constructing these graphs, the values of the complex dielectric constants for gold and aluminium (at 0.6328μm) were taken as -10.2-j.966 and -47-j16.41 respectively. The corresponding values at 1.15um are -128.8-j27.4 and -0.114-j7.366 respectively. There is some variation in the quoted values given by authors [40] in the literature

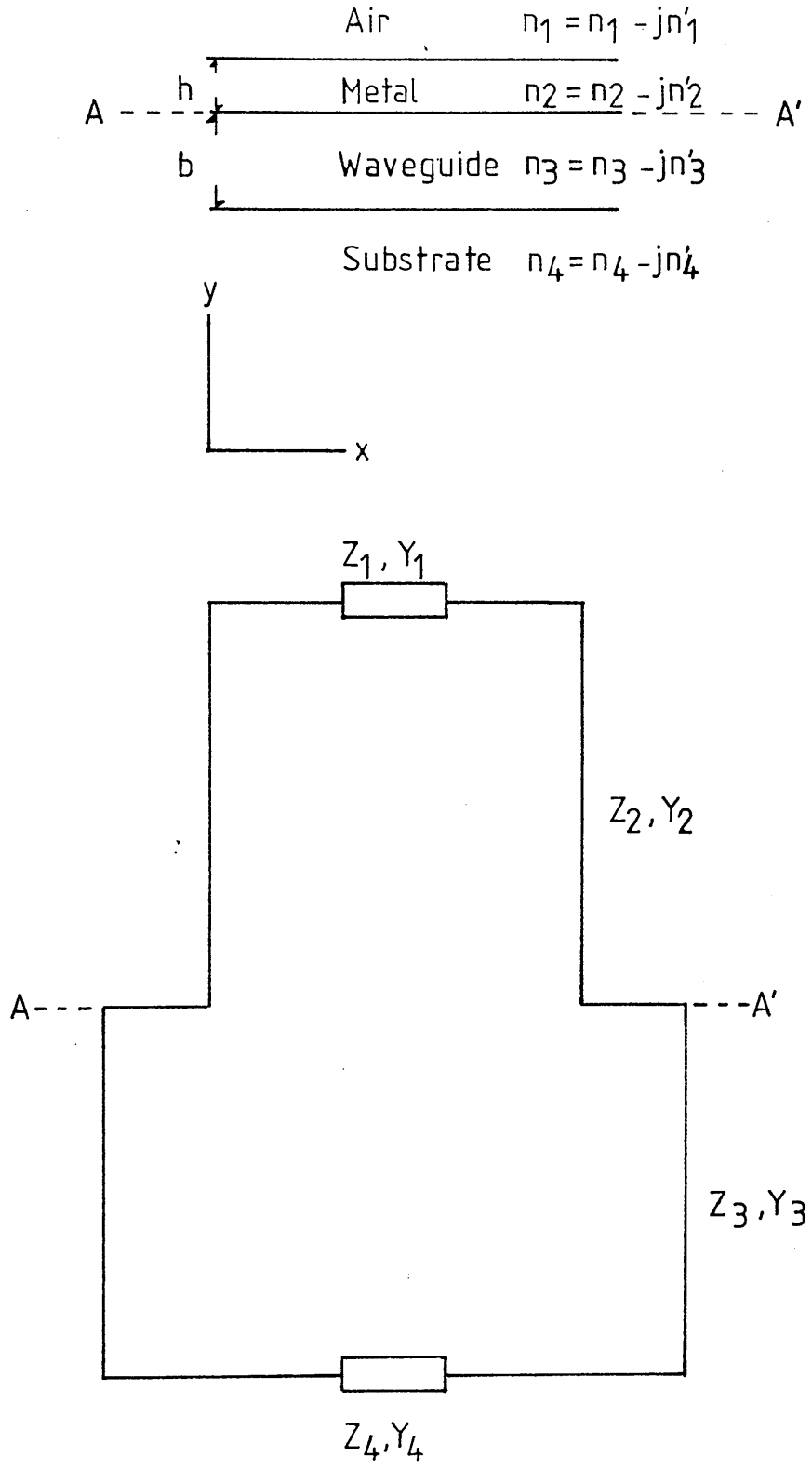

Transmission Line Represtation

FIG.2.7. The four layer dielectric slab with complex refractive indices.

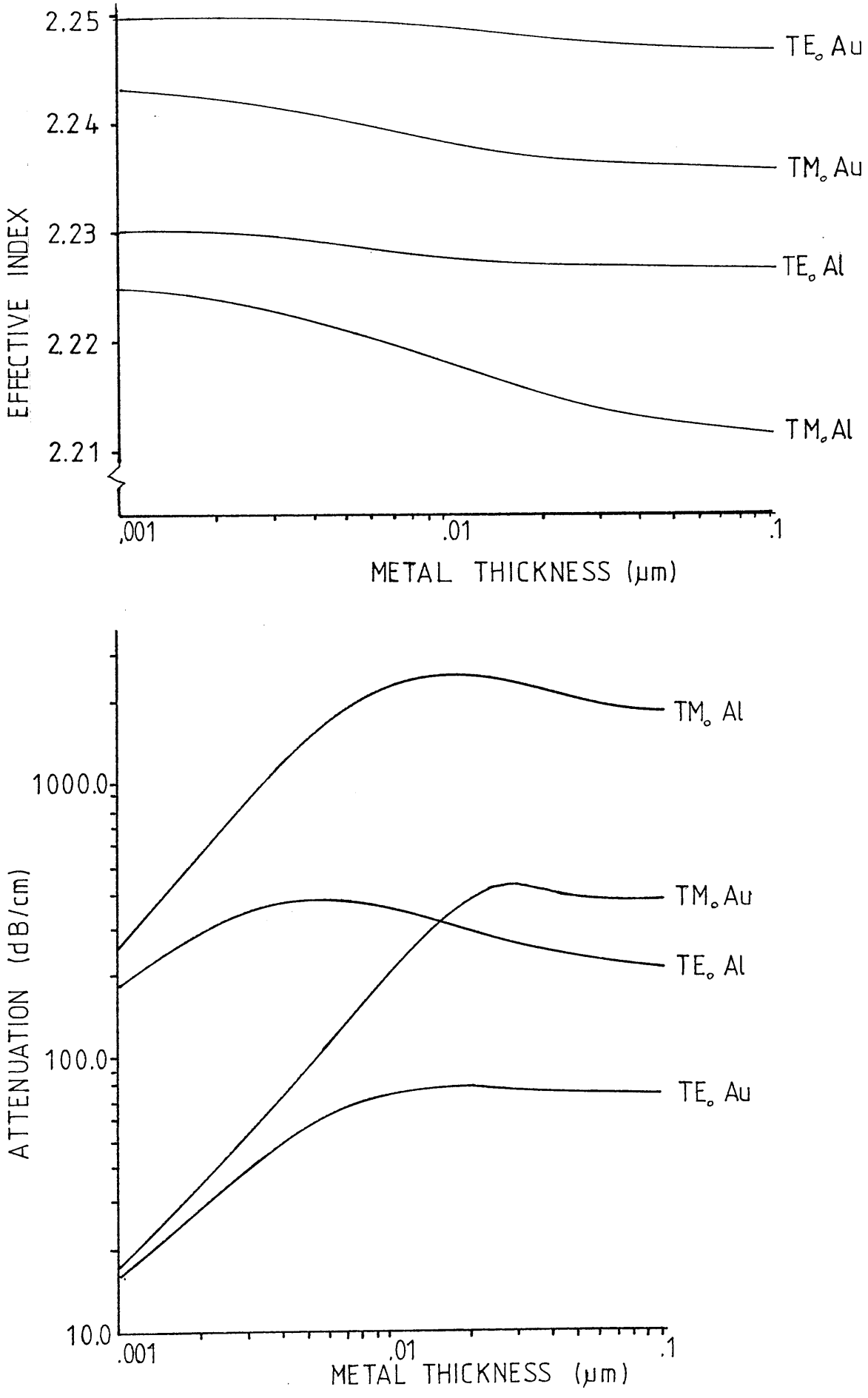

FIG.2.8. Attenuation and effective index for a metal clad dielectric slab waveguide at 633nm.

which can be attributed to the film deposition method used.

For the TM- modes, coupling can occur at the boundary between the waveguide and the metallic interface to the surface plasmon wave [32,41]. A more detailed account of this phenomenom is given in [42]. In calculating the TM-modes of the metal clad waveguide the TM_0 mode was assumed rather than the surface plasmon mode (TM_{-1}) [41] because the TM_0 mode of the unclad waveguide transforms to the TM_0 mode of the clad structure [35].

The graphs exhibit an absorption peak for both TE- and TM-modes at particular values of metal thickness (in contrast to the results reported by Polky et al. [38]). The peak may be explained by the change in the penetration of the electric field into the metal due to the modifield field profile shifting towards the substrate for increasing metal thickness. The magnitude of the peak is about an order of magnitude greater for the TM-mode than for the TE-mode. If the surface plasmon wave is excited this factor may be increased by at least an order of magnitude.

The effective index method may be applied to the analyses of rib structures and diffused waveguides [43] which have metal films deposited upon them. Two cases are common in this configuration: the first where the film is directly above the waveguide and the other where it is placed symmetrically on either side. Only the latter case will be considered here and the film is assumed to extend to infinity for the present purpose. The case of a gold overlay is taken to be representative of the results obtained from using other metals. In constructing Figs.2.9a and 2.9b the data for the

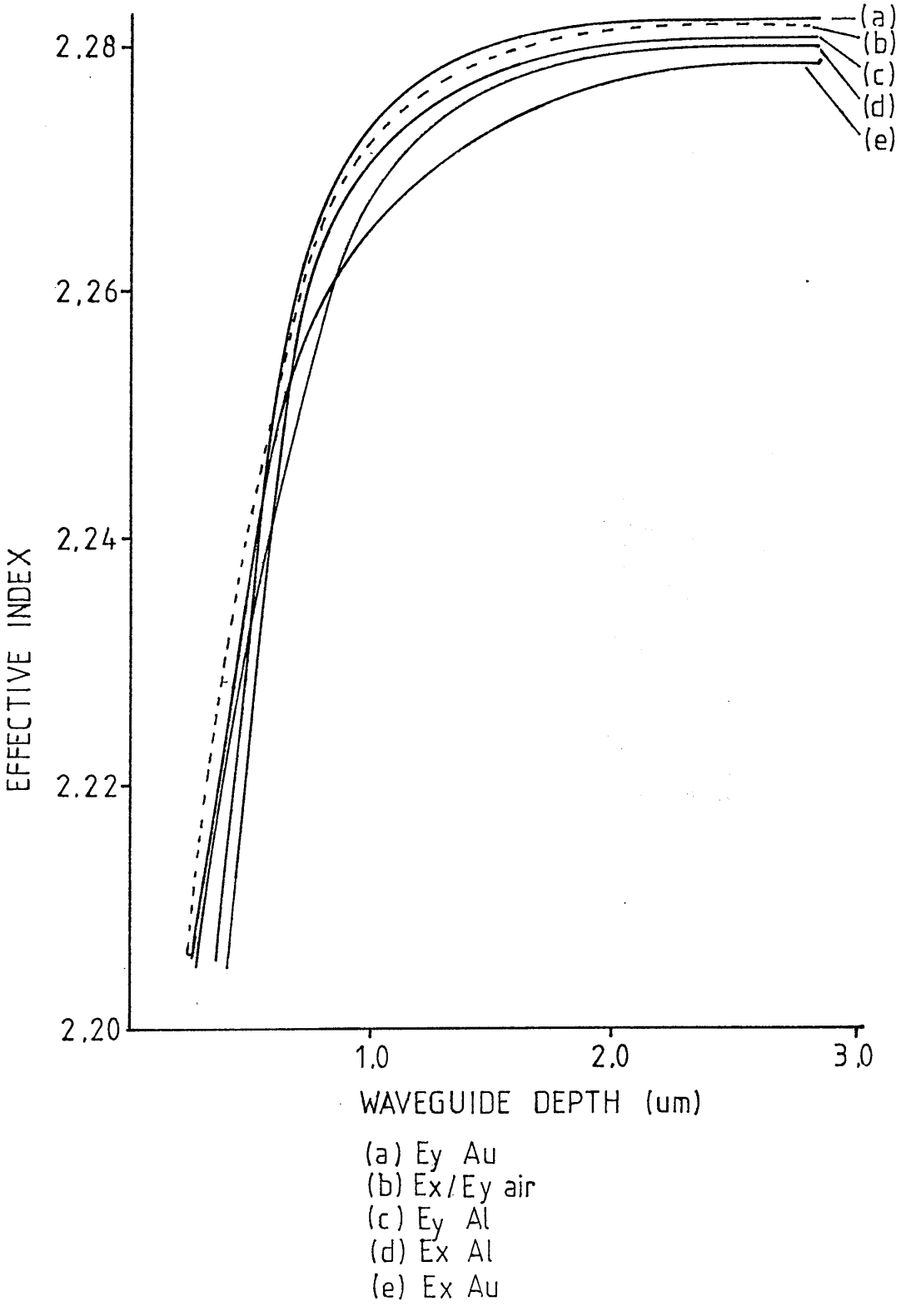

FIG.2.9a. Effective index vs. waveguide depth for 3μm wide metal clad rectangular waveguide at 633nm.

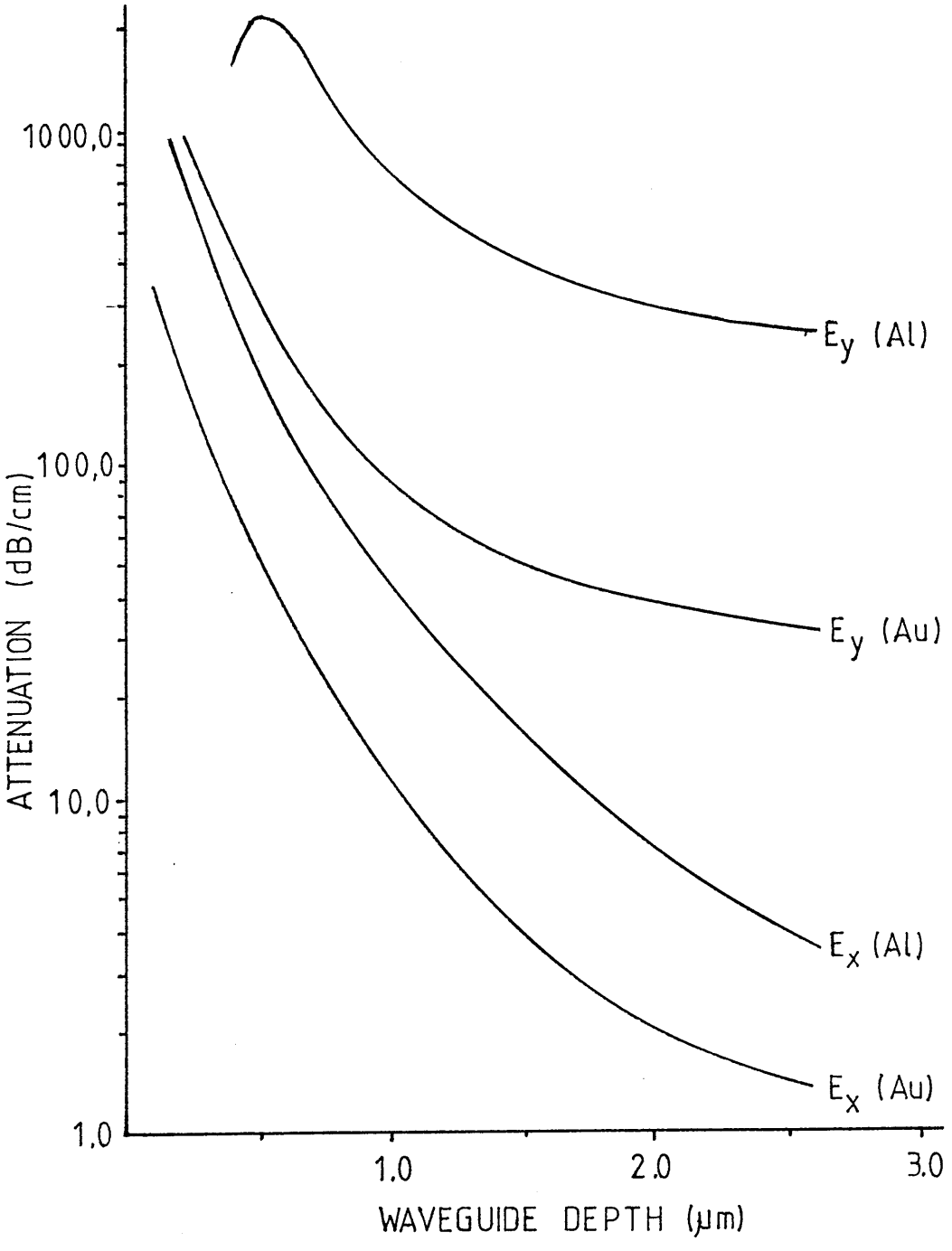

FIG.2.9b. Attenuation vs. waveguide depth for 3μm wide metal clad rectangular waveguide at 633nm.

refractive indices (at 0.633μm) given in Fig.2.5 Case 2 were used for a channel waveguide 3μm wide . It was assumed that the metal was infinitely thick which is valid for thicknesses greater than 500Å. The effect of buffer layers upon the attenuation characteristics is considered elsewhere [42].

Fig.2.9b shows that as the depth of the waveguide increases, the absorption process due to the presence of the metallic film decreases, because the peak of the electric field moves deeper into the substrate as the depth of the waveguide increases, producing a smaller field intensity at the metal interface. The effective refractive index for a confined field at a metal dielectric interface can be obtained from Otto's work and is simply [31]:

$$n_{eff} = n_s\left[\frac{\epsilon_1}{\epsilon_1 + n_s}\right]^{1/2} \qquad (2.40)$$

where n_s is the substrate refractive index and ϵ_1 is the real part of the complex dielectric constant for the metal.

The effect of the metal overlay on the propagation constant is to decrease it slightly with respect to the original unmodified waveguide. This may be of advantage in the design of directional couplers to control the evanescent field. It can also be used to define optical waveguides in a planar diffused region by etching a slot in the metal overlay to define the waveguide. It should be mentioned that the effective index method is only an approximate method for this situation because the introduction of a lossy medium destroys the orthogonality of the fields and thus the separability concept. Nevertheless, it does provide a valuable tool in the

initial stages of analysis of such a problem. Again, the accuracy of this method close to cut-off is questionable.

2.7. ANALYSIS OF ELECTRO-OPTIC MODULATION FOR A SCHOTTKY CONTACT ON A RIB STRUCTURE IN GaAs/AlGaAs.

The most typical waveguide formed in GaAs is the rib waveguide [44,45,46], although diffused [47] and stress-induced waveguides [48,49] have been reported.

For an electro-optic modulator that is designed to operate at a high frequency the only microwave waveguide that can be used conveniently in conjunction with etched rib waveguides is the stripline waveguide Fig.2.10. This structure has received considerable analysis, especially by Wheeler [50,51], who determined the characteristic impedance and attenuation constant.

Optical field confinement in the rib waveguide in the vertical direction is produced by using epitaxial layers of GaAs and AlGaAs. The refractive index of such compounds is less than GaAs and the refractive index is dependent on the Al concentration [52]. The electrical characteristics of these layers are also of great importance in order to maximise the field overlap and to reduce the free carrier absorption of the optical field. The simplest manner in which this can be achieved is to form a depleted region within the optical waveguide by forming a Schottky [53,54] contact on the rib structure. Depending on the reverse bias, the extent to which the depleted region extends underneath the rib waveguide can be controlled. The control is of significant importance for designing active directional couplers.

In analysing the depletion layer problem, because of the

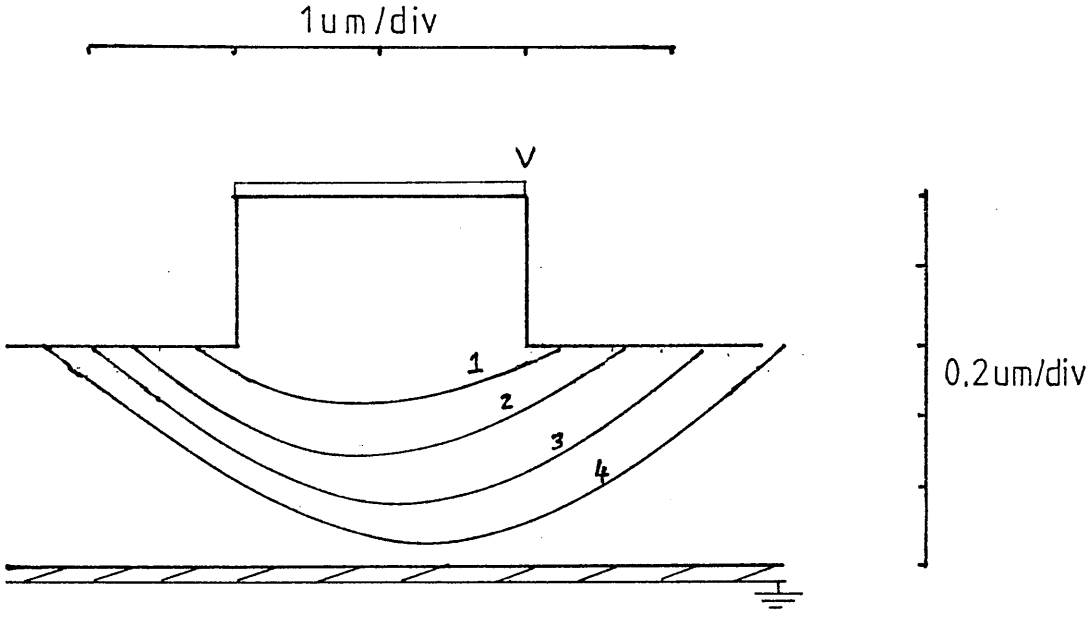

Profile	Carrier Conc (cm^{-3})	Bias (V)
1	10^{17}	-20
2	5.10^{16}	-20
3	1.10^{16}	-20
4	4.10^{15}	-3

FIG.2.10. Depletion region profile as a function of carrier concentration and reverse bias.

complexity of the waveguide geometry, the only approach available to determine the depleted region is to use a finite difference technique to solve Poisson's equation:

$$\frac{\partial^2\phi(x,y)}{\partial x^2} + \frac{\partial^2\phi(x,y)}{\partial y^2} = -\frac{\rho(x,y)}{\epsilon} \qquad (2.41)$$

where ρ is the charge distribution at each node in the discrete representation of the waveguide structure.

The numerical solution of Equ.(2.41) involves the finite difference method with the added complication of determining the depletion region profile from the field distribution. An initial guess is made for the shape of the region by defining an area free of mobile carriers i.e. a region with positive charges at each node. The field distribution is then obtained by iteration until the error between the potential from successive iterations converges to a pre-determined value [55,56].

After the new potentials have been calculated the depletion region is updated using the following criteria: if the potential at a node directly below or to the side is negative then that node is depleted of charge and given a positive voltage equal to the uncompensated charge per unit volume. If the node has been previously depleted it is left unchanged. For the case of the voltage below the node or to the sides being greater then charge is subtracted from the node if it was present in the first place. If no charge was present then the node is left unchanged. The new charge distribution is then iterated again to give a new field profile and the charge modification is repeated until there are no further updates to any of the nodes.

Fig.2.10 shows the results using this method for various epilayers of different thicknesses, carrier concentrations and reverse biases. From this information the carrier concentration has to be less than 10^{15} cm^{-3} for a rib 3μm wide etched in an epitaxial layer 1μm deep, to provide complete depletion of carriers within the waveguiding region.

For case 4 depicted in Fig.2.10, the phase change per unit length from the electro-optic effect resulting from the applied bias of -3V can be readily obtained from the expression [57]:

$$\Delta\beta = \frac{\pi \Gamma n^3 \Gamma E}{\lambda} \qquad (2.42)$$

where 'r' is the electro-optic coefficient (Appendix A) and Γ is a dimensionless number indicating the degree of overlap between the electric and optical fields and has a value between 0 and 1. Taking 'r' as $1.1.10^{-12}$m/V and Γ as 0.5 (a somewhat arbitrary value), the phase change at 1.15μm is 180 radians per metre. Therefore for a half-wave phase shift a device length of 1.8cm is necessary.

SUMMARY.

This chapter has highlighted some of the most common methods available for analysing optical waveguides. Depending upon the aspect ratio and the refractive index distribution the simple approximate methods offer reasonable accuracy when the waveguide is not close to cut-off.

The loss due to the proximity of metal films to the waveguides has also been analysed. The phase constant

is not sufficiently perturbed from the value obtained for a similar waveguide in the absence of a metal overlay. However, the attenuation of the optical field is increased substantially, with TM-modes undergoing severe attenuation. A peak is observed in the attenuation factor for both TE- and TM-modes at a certain metal film thickness. The peak arises due to a combination of the penetration into the film and a change in the field profile as it is pushed deeper into the waveguide as the film thickness increases. As the metal film increases a point is reached where the mode profile does not alter substantially thus producing little or no change in the attenuation constant. The magnitude of the final value is also dependent upon the extinction coefficient of the metals; the smallest losses are observed for metal which have a small extinction coefficient. This favours gold as the most suitable metal to form an electrode structure, in comparison with aluminium and silver at 0.633μm by a factor of approximately 10.

An attempt is made at analysing the depleted region underneath an electrode structure placed on top of an etched rib waveguide in GaAs. The variation in the depth of the depleted region as a function of the carrier concentration and applied voltage is shown.

References Chapter 2.

[1] C.Yeh,K.Ha,S.B.Dong and W.P.Brown.
Single mode optical waveguides.
Appl. Opts., Vol.18(10), 1979,pp.1490-1504.

[2] A.Wexler.
Computation of electromagnetic fields.
I.E.E.E. Trans. Microwave Theory and Tech.
Vol.M.T.T.17(8), 1969, pp.619-639.

[3] R.E.Collin.
Foundations for microwave engineering.
McGraw-Hill 1966, Chap.2.

[4] R.F.Harrington.
Time harmonic Electromagnetic Fields.
McGraw-Hill 1961, Chap.2.

[5] E.A.Marcatili.
Dielectric rectangular waveguide and
directional coupler for integrated optics.
B.S.T.J., Vol.48(3), 1969, pp.2071-2102.

[6] J.E.Goell.
Circular harmonic computer analysis of
rectangular dielectric waveguides.
B.S.T.J., Vol.48(3), 1969, pp.2133-2160.

[7] A.Kumar,K.Thayagarajan and A.K.Ghatak.
Analysis of rectangular core dielectric
waveguide: an accurate perturbation approach.
Opts. Letts., Vol.8(1), 1983, pp.63-65.

[8] R.M.Knox and P.P.Toulios.
Integrated circuits for the millimetre through optical frequency range. in Fox, J.(Ed.) "Proceedings of the MRI Symposium on submillimeter waves."
Polytech Press.
Brooklyn, N.Y. 1970
pp.497-516.

[9] D.N.MacFadyen.
Components for Gallium Arsenide integrated optics fabricatedby wet chemical etching.
Ph.D. Thesis, University of Glasgow, 1980.

[10] H.Furuta,H.Noda and A.Ihaya.
Novel optical waveguide for integrated optics.
Appl. Opts., Vol.13(2), 1974, pp.322-326.

[11] G.B.Hocker and W.K.Burns.
Modes in diffused optical waveguides of arbitrary index profile.
I.E.E.E. J. Quant. Electrs.,VolQE11(6), 1975, pp.270-276.

[12] R.E.Collin.
Foundations for microwave engineering.
McGraw-Hill, 1961, Chap.3.

[13] A.A.Oliner,H.L.Bertoni and R.C.M.Li.
A microwave network formalism for acoustic waves in isotropic media.
Proc. I.E.E.E.,Vol.60(12), 1972,pp.1501-1512.

[14] M.Koshiba and M.Suzuki.
Microwave network analysis of dielectric thin-film waveguides for millimeter waves made of dielectric strip and planar dielectric layer.
Trans. Inst. Electron. Commun. Eng. Japan.
Vol.E63, pp.340-350.

[15] M.Koshiba and M.Suzuki.
Equivalent network analysis of dielectric thin-film waveguides for optial integrated circuits.
Trans. Inst. Electron. Commun. Eng. Japan.
Vol. E64, pp.283-285.

[16] M.Koshiba and M.Suzuki.
Equivalent network analysis of dielectric thin-film waveguides for optical integrated circuits and its applications.
Radio Science, Vol.17(1), 1982, pp.99-102.

[17] N.Dagli and C.G.Fonstad.
Analysis of rib dielectric waveguide.
I.E.E.E. J. Quant. Electrs.,Vol.QE21(4),1985, pp.315-321.

[18] N.Mabaya,P.E.Lagasse and P.Vandenbulcke.
Finite element analysis of optical waveguides.
I.E.E.E. Trans. Microwave Theory and Tech.
Vol.M.T.T.29(6), 1981, pp.600-615.

[19] B.M.A.Rahman and J.B.Davies.
Finite element solution of integrated optical waveguides.
I.E.E.E. J. Light. Techn.,Vol.LT2(5), 1984 pp.682-688.

[20] B.M.A.Rahman and J.B.Davies.
Vector H finite element solution of Ga/GaAlAs rib waveguide.
I.E.E. Proc. J.,Vol.132(6), 1985, pp.349-353.

[21] H.A.Haus.
Private Communication, 1985.

[22] T.M.Benson and J.Buus.
Optical guiding in III-V semiconductor rib structures.
2nd. European Conference on Integrated Optics.
Florence, Italy, 1983.

[23] B.A.Carre.
The determination of the optimum accelerating factor for successive over relaxation.
Computer Journal, Vol.4, 1961, pp.73-78.

[24] I.A.Cermak and P.Silvester.
Solution of 2-dimensional field problems by boundary relaxation.
Proc. I.E.E., Vol.115(9), 1968, pp.1341-1348.

[25] H.E.Green.
The numerical solution of some important transmission line problems.
I.E.E.E. Trans. Microwave Theory and Tech.
Vol.M.T.T.13(5), 1965, pp.676-692.

[26] M.J.Robertson,S.Ritchie and P.Dayan.
Semiconductor waveguides: analysis of optical propagation in single rib structures and directional couplers.
I.E.E. Proc.Pt.J,Vol.132(6), 1985,pp.336-343.

[27] M.Matsuhara.
Analysis of T.E.M. modes in dielectric waveguides by a variational method.
J. Opt. Soc. Amer.,Vol.63(12), 1973, pp.1514-1517

[28] R.G.Walker.
The design of ring-resonators for integrated optics using silver ion-exchanged waveguides.
Ph.D. Thesis, University of Glasgow, 1981.

[29] M.W.Austin.
Theoretical and experimental investigation of GaAs/AlGaAS and n/n GaAs rib waveguides.
I.E.E.E. J. Light. Tech.,Vol.LT2(5),1984, pp.688-694.

[30] M.Kuznetsov.
Expressions for the coupling coefficient of a rectangular waveguide directional coupler.
Opt. Letts.,Vol.8(9),1983,pp.499-501.

[31] A.Otto and W.Sohler.
Modification of the total reflection modes in a dielectric film by one metal boundary.
Opt. Comms.,Vol.3(4), 1971,pp.254-256.

[32] A.Otto.
Excitation of nonradiative surface plasma waves in silver by the method of frustrated reflection.
Zeitshrift fur Physik,Vol.216,1968, pp.398-410.

[33] J.P.G.Bristow,A.C.G.Nutt and P.J.R.Laybourn.
Novel integrated optical polarisers using surface plasma waves and ion milled grooves in $LiNbO_3$.
Elec. Letts.,Vol.20(25/26),1984,pp.1047-1048.

[34] Y.Suematsu,M.Hakuta,K.Furuya,K.Chiba and R.Hitsumi.
Fundamental transverse electric field (TE0) mode selection for thin film asymmetric light guides.
Appl. Phys. Letts.,Vol.21(6),1972,pp.291-293.

[35] Y.Yamamoto,Y.Kamiya and H.Yanai.
Characteristics of optical guided modes in multilayer metal clad planar optical guide with low index buffer layer.
I.E.E.E. J. Quant. Electrs.,Vol.QE11(9),1975 pp.729-736.

[36] T.Takano and J.Hamasaki.
Propagating modes of a metal clad dielectric slab waveguide for integrated optics.
I.E.E.E. J. Quant. Electrs.,Vol.QE8(2), 1972, pp.206-212.

[37] S.C.Rashleigh.
Four layer metal clad thin film optical waveguides.
Opt. and Quant. Electrs.,Vol.8, 1976.
pp.49-60.

[38] J.N.Polky and G.L.Mitchell.
Metal clad planar dielectric waveguide for integrated optics.
J. Opt. Soc. Amer.,Vol.64(3),1974,pp.274-279.

[39] A.A.Oliner and S.T.Peng.
Effects of metal overlays on 3-D optical waveguides.
Appl. Opts.,Vol.17(18),1978,pp.2866-2867.

[40] J.H.Weaver,C.Krafka,D.W.Lynch and E.E.Koch.
Optical Properties of Metals.
Physics Data, Nr.12-18,Fach-Informations Zentrum, ISSN 0344-8401,1981.

[41] A.Reisinger.
Characteristics of Optical Guided Modes in Lossy Waveguides.
Appl. Opt.,Vol.12(5),1973,pp.1015-1025.

[42] J.P.G.Bristow.
Integrated optical components for optical fibre sensors.
Ph.D. Thesis, University of Glasgow,1985.

[43] T.Findakly and C.L.Chen.
Diffused Optical Waveguides with Exponential Profile: Effects of metal clad and Dielectric Overlay.
Appl. Opts.,Vol.17(3),1978,pp.469-474.

[44] J.C.Shelton,F.K.Reinhart and R.A.Logan.
Characteristics of rib waveguides in GaAs.
J. Appl. Phys.,Vol.50(11),1979,pp.6675-6687.

[45] M.W.Austin.
Theoretical and experimental investigation of GaAs/AlGaAs and n/n+ GaAs waveguides.
I.E.E.E. J. Light. Techn.,Vol.LT2(5),1984 pp.688-694.

[46] A.J.N.Houghton,D.A.Andrews,G.J.Davies and S.Ritchie.
Low loss optical waveguides in M.B.E. grown GaAs/GaAlAs heterostructures.
Opts. Comms.,Vol.46(3),1983,pp.164-166.

[47] E.Garmire,D.F.Lovelace and G.H.B.Thompson.
Diffused two dimensional optical waveguides in GaAs.
Appl. Phys. Letts.,Vol.26(6),1975,pp.329-331.

[48] P.A.Kirby.
Photoelastic waveguides and their effect on stripe geometry GaAs/$Al_xGa_{1-x}As$ lasers.
J. Appl. Phys.,Vol.50(7),1979,pp.4567-4579.

[49] T.M.Benson,T.Murotani,P.N.Robson and P.A.Houston.
Novel electro-optically controlled directional coupler switch in GaAs epitaxial layers at 1.15μm.
I.E.E.E. Trans. Electr.,Dev.,Vol.ED19(9),1982, pp.1477-1483.

[50] H.A.Wheeler.
Transmission line properties of parallel strips separated by a dielectric sheet.
I.E.E.E. Trans. Microwave Theory and Tech. Vol. M.T.T.12(2),1964,pp.280-289.

[51] Harold A. Wheeler.
Transmission line properties of a strip on a dielectric sheet on a plane.
I.E.E.E. Trans. Microwave Theory and Tech. Vol. M.T.T.25(8),1977,pp.631-647..

[52] H.Casey,D.D.Sell and M.B.Panish.
Refractive index of $Al_xGa_{1-x}As$ between 1.2 and 1.8eV.
Appl. Phys. Letts.,Vol.49(11),1978, pp.5404-5406

[53] A.Carenco,L.Menigaux,F.Alexandre,M.Abdalla and A.Branc.
Directional coupler switch in molecular-beam epitaxy GaAs.
Appl. Phys. Letts.,Vol.34(11),1979,pp.755-757.

[54] A.R.Reisinger,D.W.Bellavance and K.L.Lawley.
GaAlAs Schottky directional-coupler switch.
Appl. Phys. Letts.,Vol.31(12),1977,pp.836-840.

[55] S.Colak and E.H.Stupp.
Reverse avalanche breakdown in gated diodes.
Solid State Elect.,Vol.23,1980,pp.472-476.

[56] A.D.Sutherland.
An algorithm for treating interface surface charge in the two dimensional discretisation of Poisson's Equation for the numerical analysis of semi-conductor devices such as MOSFETs.
Solid State Elect.,Vol.23,1980,pp.1085-1087.

[57] I.P.Kaminow.
Optical Waveguide Modulators.
I.E.E.E. Trans. Microwave Theory and Tech.
Vol.M.T.T.23(1), 1975, pp.57-69.

CHAPTER 3

THEORETICAL DESIGN OF THE STANDING WAVE MODULATOR.

3.0 INTRODUCTION

This chapter introduces the theoretical development for the design of a novel modulator for integrated optics: the standing wave modulator (Fig.3.1) [1]. In contrast to the usual travelling wave modulator, this device exhibits a narrow bandwidth of a few gigahertz centred at a high frequency (~10GHz). In order to verify the design procedure, a modulator with the following design specifications was fabricated and subsequently tested. The design parameters chosen to illustrate the operation were; a resonant frequency of 10GHz with a bandwidth of approximately 1GHz, with either $LiNbO_3$ or GaAs as the substrate material.

The theory for the design stems from the familiar transmission line equations applied to lines that exhibit loss [2]. At this level, some simplification has been made by assuming that the losses are small and are due to conduction losses in the electrode conductors. In the analysis radiation losses have been neglected. The assumption of small losses is justified later from the experimental behaviour of the electrode structure.

Throughout the analysis the microwave transmission line employed for the electrode structure is not explicitly defined. The generality has been achieved simply by using the parameters common to all forms of transmission lines: principally the complex propagation constant and the characteristic impedance. It is only in the later stages that the specific form of transmission line used in the

actual experimental device is considered and analysed.

From simple loss considerations of the transmission line forming the resonant structure, the bandwidth of the device can be described by a single parameter which incorporates the propagation and attenuation constants of the line. Hence, a knowledge of the electrode losses is essential in order to predict accurately the experimental bandwidth.

Most transmission line structures employed in the electrode fabrication have been well documented and relationships are available for the propagation constant and attenuation factor. However, to model accurately the waveguide configuration employed for this particular project, a finite difference technique was developed to calculate the theoretical attenuation factor and the characteristic impedance from the physical dimensions and resistivity of the conductors. Throughout the synthesis procedure, extensive use was made of a computer to model the microwave response of the transmission line and the bandwidth of the device. The results obtained by this method are compared with those described by other authors later on.

As indicated in the introductory chapter, the standing wave modulator exhibits several advantages over the more usual forms of lumped component and travelling—wave modulator. Compared to these other modulators the key advantage of the standing wave modulator is the enhanced voltage distribution arising from its resonant mode of operation. The maximum voltage along the line can be considerably greater than the driving voltage and thereby increase the depth of modulation observed.

The phase modulation of the optical carrier as it passes through an electro-optic material, is, to a first approximation, linearly related to the locally applied electric field strength. The degree or depth of modulation as a function of frequency forms the basis for several figures of merit describing the performance of electro-optic modulators (specifically the P/Δf figure); they are not entirely applicable to the standing wave modulator, which exhibits voltage enhancement. However, this figure of merit may be suitably modified to account for this response.

3.1. THEORETICAL DEVELOPMENT.

The structure of the standing wave modulator electrode pattern is shown in Fig.3.1 [3]. The resonant section is modelled by the frequency response of two shorted transmission lines of unequal length, connected in parallel, which have a small loss component associated with them. The overall length of the combined structures is approximately equal to half a guide wavelength at the desired resonant frequency. Thus, the total length is dependent upon the desired operating frequency which is, in turn, a function of the waveguide propagation constant, the waveguide geometry and the dielectric constant of the substrate material.

3.1.1. TRANSMISSION LINE LOW LOSS APPROXIMATION.

It has been shown that microwave stripline technology may be used in conjunction with integrated optics to form high speed active devices without encountering excessive electrical loss [4]. To illustrate how the small losses associated with a transmission line can be of benefit in the design of the standing wave modulator, a description

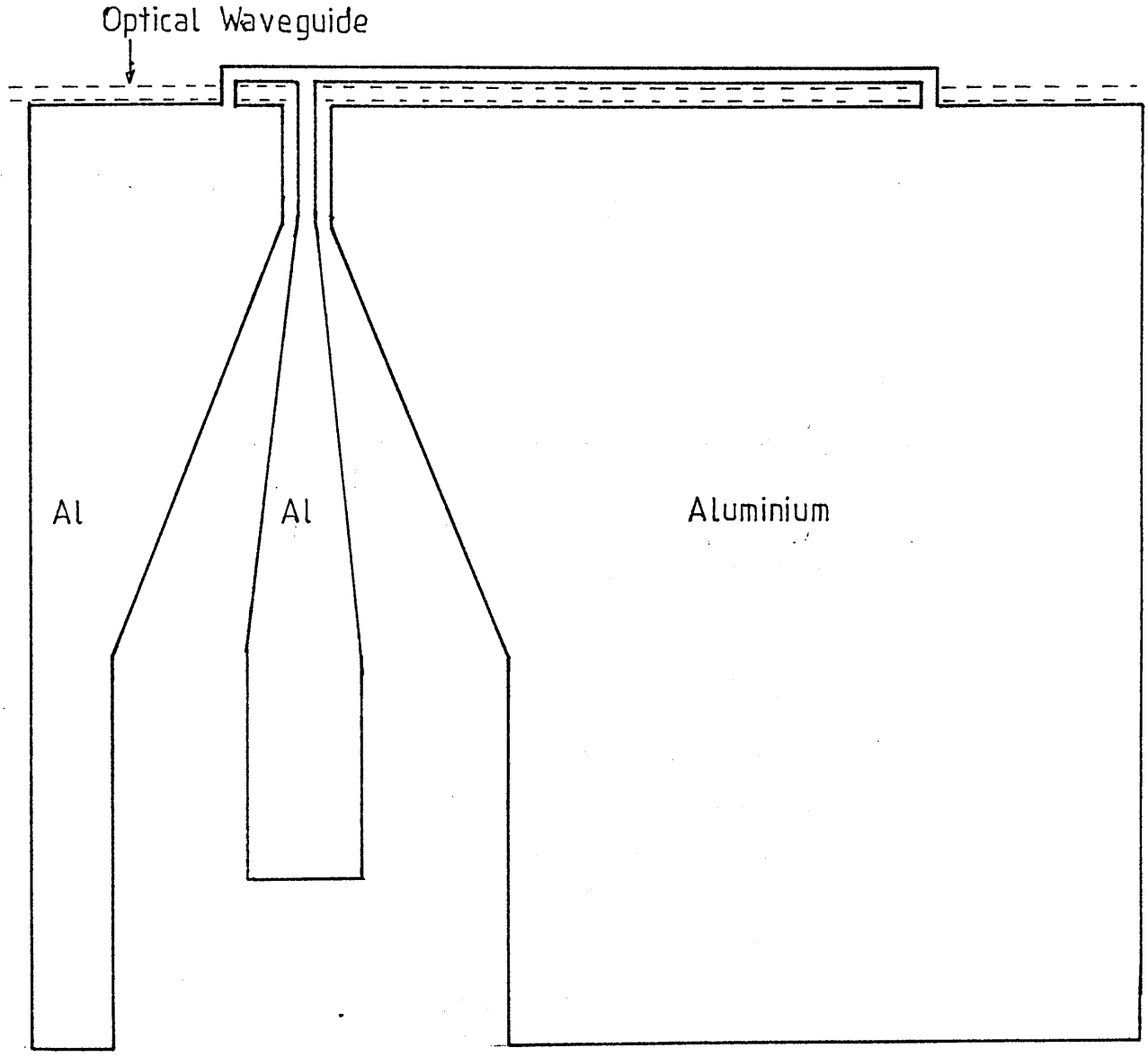

FIG.3.1. The standing wave modulator electrode pattern.

will now be given.

The variation in input admittance with distance from the plane of a short circuit is conveniently shown by means of a Smith chart (Fig.3.2). For a completely lossless line the locus of the input admittance follows a circle along the periphery of the chart. If the line possesses some loss the locus is no longer a circle but a spiral, starting from the periphery and moving towards the centre. The rate at which the locus spirals towards the centre is dependent upon the degree of attenuation. Fig.3.2 also illustrates the locus of the input admittance for various values of the normalised attenuation constant α/β .

Two points arise from this diagram, both of which influence the final design of the device. The first point is that, for a transmission line of the correct characteristic impedance, if the attenuation factor is large and/or the line length is long the transmission line appears matched. This results from the energy being entirely dissipated before it encounters the impedance mismatch terminating the line. The situation is depicted on the Smith chart by the locus spiralling towards the centre. Although the load appears matched to the generator, the losses are so excessive that this structure would not resonate.

The second point is that for a small loss the locus intercepts the g=1 conduction circle, which offers the posibility of matching the shorted line to the drive line by the principle of single stub tuning to tune out the undesired susceptance at a particular frequency. This principle, will in practice, give a specific bandwidth over which the line will appear approximately

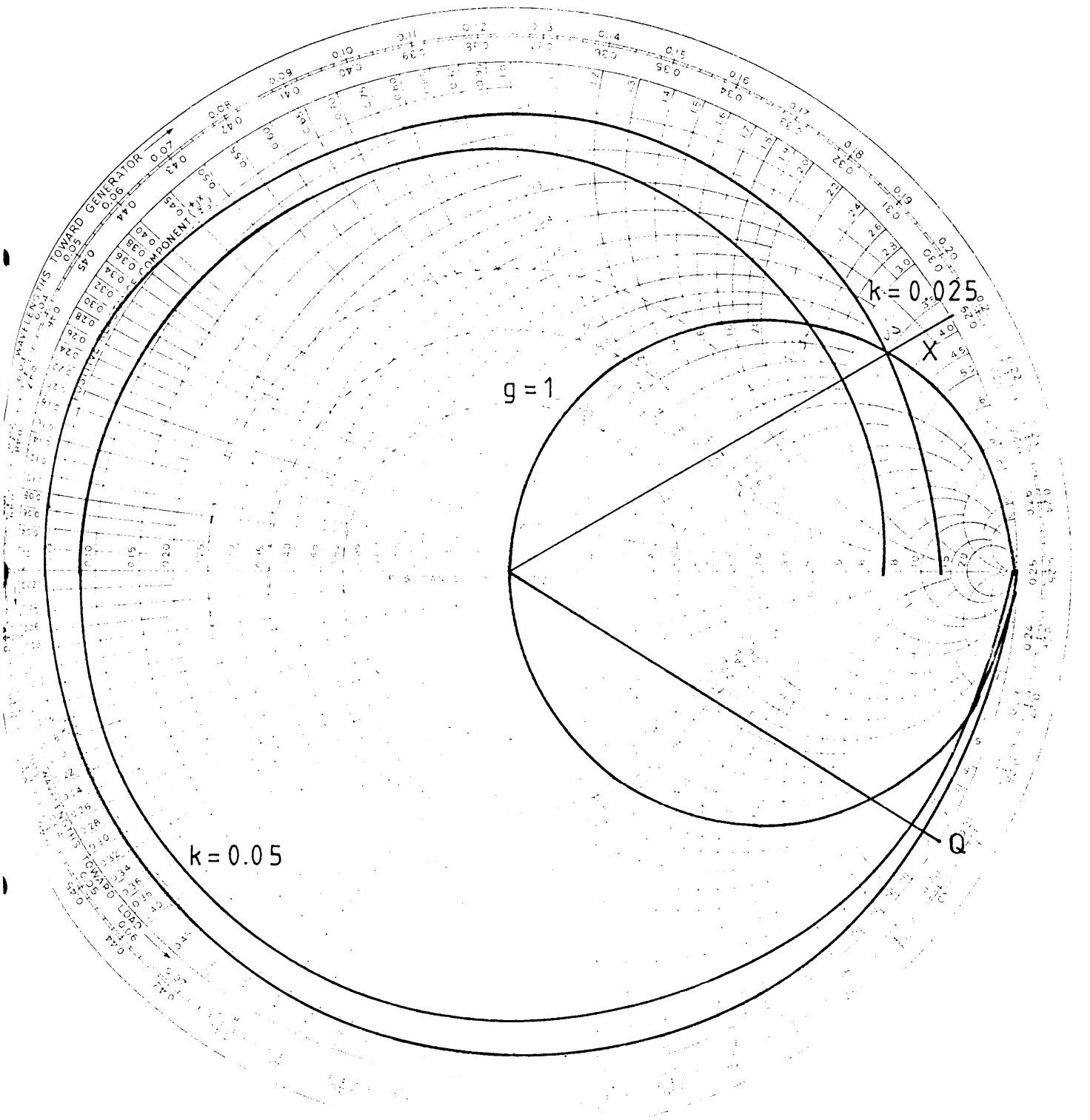

$k = \alpha/\beta$

FIG.3.2. Admittance locus for a short circuited lossy transmission line.

G_o	distributed conductance	(S/m)
Z_o	characteristic impedance	(Ω)
γ	complex propagation constant	(m^{-1})
Q	quality factor	
f_o	resonant frequency	(Hz)
ω	angular frequency	(rad/s)
ω_o	resonant angular frequency	(rad/s)
l	length of line	(m)
z	length variable	(m)
k	coupling coefficient	(m^{-1})
a	complex mode amplitude	
τ	time constant	(s)
ρ	reflection coefficient	
E	electric field strength	(V/m)
f_m	r.f. modulating frequency	(Hz)
c	speed of light in vacuo	(m/s)
n_o	optical refractive index	
n_m	microwave refractive index	
U	total enery stored	(J)
W	average energy loss	(W)
w	coplanar waveguide width	(m)
g	coplanar waveguide separation	(m)

One of the most useful parameters describing the behaviour of any resonant structure is the Q-factor [5]. The Q-factor is the ratio of the resonant frequency to the bandwidth (half power points) and can be shown to give an indication of the losses present within the resonant system. The Q-factor is derived by applying the standard definition of the ratio of the energy stored to that dissipated through losses during each cycle:

$$Q_o = 2\pi f_o U/W \qquad (3.1)$$

Before evaluating this expression, the input impedance of

two short circuited transmission lines of unequal length connected in parallel has to be found for the low loss approximation to give the voltage distribution. This is calculated from the usual equation relating the impedance at any plane along the line to the load termination. For a single line terminated with a short circuit, the impedance at any position is given by [2]:

$$Z(-\ell) = Z_o \tanh \gamma z \qquad (3.2)$$

The complex propagation constant can be expressed in terms of the distributed parameters of the line: i.e. the inductance, capacitance and resistance per unit length:

$$\gamma = \{(R_o + j\omega L_o).(G_o + j\omega C_o)\}^{1/2} \qquad (3.3)$$

and similarly the characteristic impedance may be expressed in the same terms as:

$$Z_o = \left\{\frac{(R_o + j\omega L_o)}{(G_o + j\omega C_o)}\right\}^{1/2} \qquad (3.4)$$

It can be assumed that the substrate material has negligible dielectric loss [6] (it can be used as a dielectric resonator) so that $G_o = 0$, which to a first approximation gives the characteristic impedance as:

$$Z_o = \sqrt{\frac{L_o}{C_o}} \cdot \left(1 - j\frac{R_o}{2\omega C_o L_o}\right) \qquad (3.5)$$

In practice, the quadrature term may be ignored (if $R_o << 2\omega CL$) which leaves:

$$Z_o = \sqrt{\frac{L_o}{C_o}} \qquad (3.6)$$

Applying the same simplification procedure to Equ.(3.3) produces:

$$\gamma = \omega\sqrt{L_o C_o}\left(\frac{R_o}{2\omega L_o} + j\right) \qquad (3.7)$$

from which the familiar quantities α and β are found to be given by:

$$\alpha = \frac{R_o}{2Z_o} \qquad (3.8a)$$

$$\beta = \omega\sqrt{L_o C_o} \qquad (3.8b)$$

Substituting these derivations into Equ.(3.2) and assuming the conduction losses are small, then gives for a short circuit termination, the input impedance :

$$Z(-z) = Z_o\frac{(\alpha z + j\tan\beta z)}{(1 + j\alpha z\tan\beta z)} \qquad (3.9)$$

The Q-factor may now be evaluated using the equations developed. The total energy stored and the energy dissipated can be expressed using the equations for the voltage and current distributions along the transmission line incorporating the low loss approximations for γ and Z_o . Evaluating these quantities leads to the simple expression for the Q-factor in terms of α and β i.e:

$$Q_o = \frac{\beta}{2\alpha} \qquad (3.10)$$

The above is entirely general for any resonant transmission line structure and these parameters can be easily determined experimentally.

3.2. INPUT COUPLING CONSIDERATIONS.

In this section the derivation of the necessary input coupling condition in order to achieve impedance matching

between the drive line and resonant structure is presented. It is assumed that the behaviour of the transmission line close to resonance is modelled by the lumped parallel RLC circuit shown in Fig.3.3. The values of the lumped elements depend upon the Q of the line and the resonant frequency. The equivalant circuit for the resonant line excited by an external source is also given by Fig.3.3.

The formal derivation of the coupling between the drive line and the resonant line involves energy exchange cosiderations between the resonant and the drive systems. The method presented follows that of Haus [7].

The energy stored within the resonator is expressed as the product of the normalised positive frequency mode amplitude with its complex conjugate 'a' i.e.:

$$U = \frac{1}{2} a . a^{*} \qquad (3.11)$$

where:

$$a = \sqrt{\frac{C_0}{2}} . V_0 . e^{j\omega_0 t} \qquad (3.12)$$

and therefore:

$$\frac{da}{dt} = j\omega_0 a \qquad (3.13)$$

which describes the variation in 'a' with time. The above equation can be modified to take into account the losses present within the system. This modification is characterised by the inclusion of extra terms which modify the mode amplitude so that it decays exponentially with time. The rate of decay is dependent upon the magnitude of these losses.

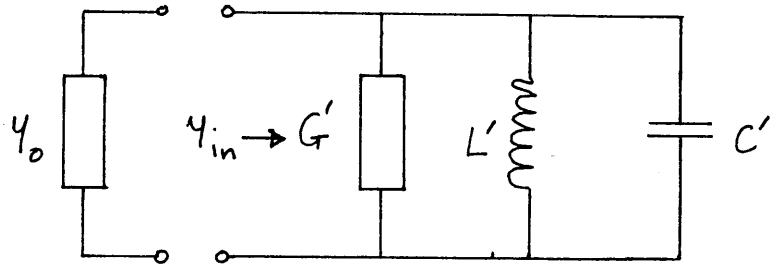

The parameters G', L', and C' may be expressed in terms of the distributed line values R_o, L_o, and C_o through α, β and Y_o where:

$$Y_{in} = G' + j\omega C' + \frac{1}{j\omega L'}$$

$$G' = \frac{(1+\tan^2\beta l_2)\,\alpha(l_1+l_2)\,Y_o}{\tan^2\beta l_2}$$

$$\omega C' = \frac{Y_o}{\tan\beta l_1}$$

$$\frac{1}{\omega L'} = \frac{-Y_o}{\tan\beta l_2}$$

At 10GHz, the values for G, C and L (taking α=23np/m and β= 873 m^{-1},) are 20.4mS, 1.12pF and 208pH.

FIG.3.3. Equivalent circuit for electrode structure close to resonance.

One loss mechanism arises from the decay of energy due to the presence of resistive losses within the resonant line:

$$\frac{du}{dt} = -\frac{2\omega_0 . u}{\tau_0} \qquad (3.14)$$

where τ_0 is the time constant from the resistive losses in the resonator. Returning to the equivalent circuit, the power dissipated through resistive losses is:

$$W = \frac{G'_e}{C'} . |a|^2 \qquad (3.15)$$

In the present situation a further modification is necessary to take into account the energy loss from the resonant line due to the coupling into a backward travelling wave away from the resonant line. This is characterised by the time constants τ_e for the external line and τ_0 for the resonant line:

$$\tau_e = \frac{C'}{Y_0} \qquad (3.16a)$$

$$\tau_0 = \frac{C'}{G'} \qquad (3.16b)$$

where Y_0 is the characteristic admittance of the driving transmission line (Fig.3.3) and:

$$G' = \frac{(1+\tan^2\beta l_2)\alpha(l_1+l_2)Y_0}{\tan^2\beta l_2} ; \quad C' = \frac{Y_0}{\omega \tan\beta l_1} ; \quad l_1+l_2 = \frac{\lambda_g}{2} \qquad (3.17)$$

where 'l_1' is the feed position from one end and the other symbols are as defined on page 60. The final equation incorporating these various factors is:

$$\frac{da}{dt} = j\omega_0 a - \left(\frac{1}{\tau_e} + \frac{1}{\tau_0}\right) a + kS_+ \qquad (3.18)$$

where s_+ is the amplitude of the driving source. The above equation has the solution:

$$a = \frac{ks_+}{j(\omega-\omega_0)+\left(\frac{1}{\tau_0}+\frac{1}{\tau_e}\right)} \qquad (3.19)$$

The only remaining parameter that is unknown is the coupling coefficient 'k'. An expresson for the numerical value of this constant can be found by considering the rate at which energy is coupled out of the resonant line. From equating the energy loss and energy input into the line the coupling coefficient can be expressed as:

$$k = \sqrt{\frac{2}{\tau_e}} \qquad (3.20)$$

When this expression for the coupling coefficient is used, the reflection coefficient ρ for the incident wave is found to be:

$$\rho = \frac{\left(\frac{1}{\tau_e}\right)-\left(\frac{1}{\tau_0}\right)-j(\omega-\omega_0)}{\left(\frac{1}{\tau_e}\right)+\left(\frac{1}{\tau_0}\right)+j(\omega-\omega_0)} \qquad (3.21)$$

which is zero when:

$$\tau_e = \tau_0 \qquad (3.22)$$

at:

$$\omega = \omega_0 \qquad (3.23)$$

i.e.: the time constant of the external circuit is equal to the time constant associated with the energy loss for the resonant line. This is equivalent to the resonant line appearing as a matched load to the transmission system at resonance or the condition of critical coupling.

After critical coupling has been achieved by virtue of the resonant line impedance being matched to the transmission system, the resonant line will exhibit a different Q value. The loaded, or overall, Q of the line will include the effects of loading by the external drive circuit. The relationship between the various Q's can be shown to be [5]:

$$\frac{1}{Q_L} = \frac{1}{Q_{ext}} + \frac{1}{Q_0} \qquad (3.24)$$

the maximum value of Q_L occurs when $Q_{ext}=Q_0$ and then:

$$\frac{1}{Q_L} = \frac{2}{Q_0} \qquad (3.25)$$

where Q_0 is the unloaded Q of the resonant line. Therefore, from the preceding section, the design Q is given by:

$$Q_L = \frac{\beta}{4\alpha} \qquad (3.26)$$

The input impedance of two unequal lengths of transmission lines terminated by short circuits and connected in parallel was found by using a computer to evaluate Equ.(3.9). The input impedance was calculated over the frequency range 8-12GHz for various values of attenuation and characteristic impedance. At resonance the input impedance should ideally be purely real and have a magnitude of 50Ω for critical coupling and hence maximum power transfer.

3.2.1. THEORETICAL INPUT RESPONSE OF RESONANT LINE.

Figs.3.4(a)-(f) illustrate the variation in the

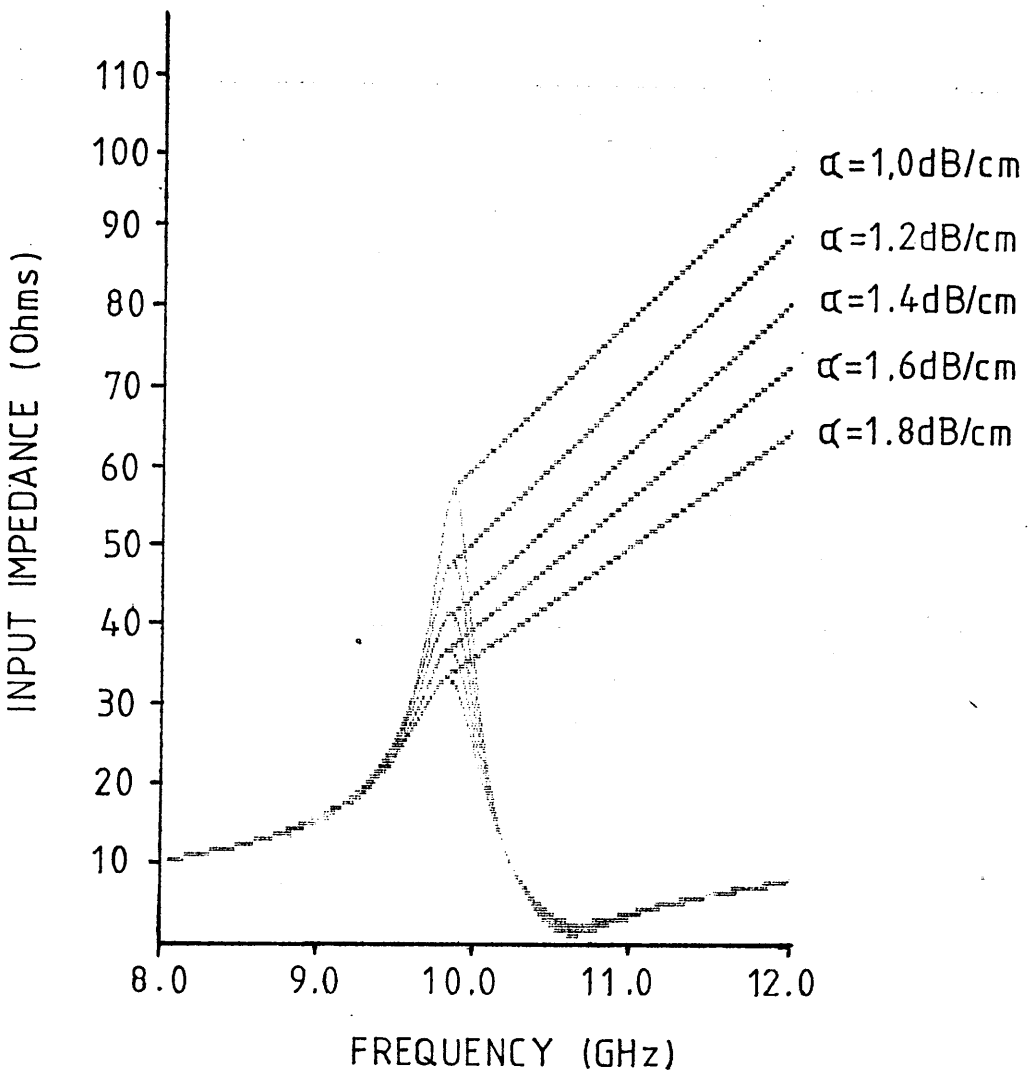

Tap position : 250um
Line length : 3600um
Z_0 : 50Ω

FIG.3.4a. Input impedance as a function of the attenuation constant.

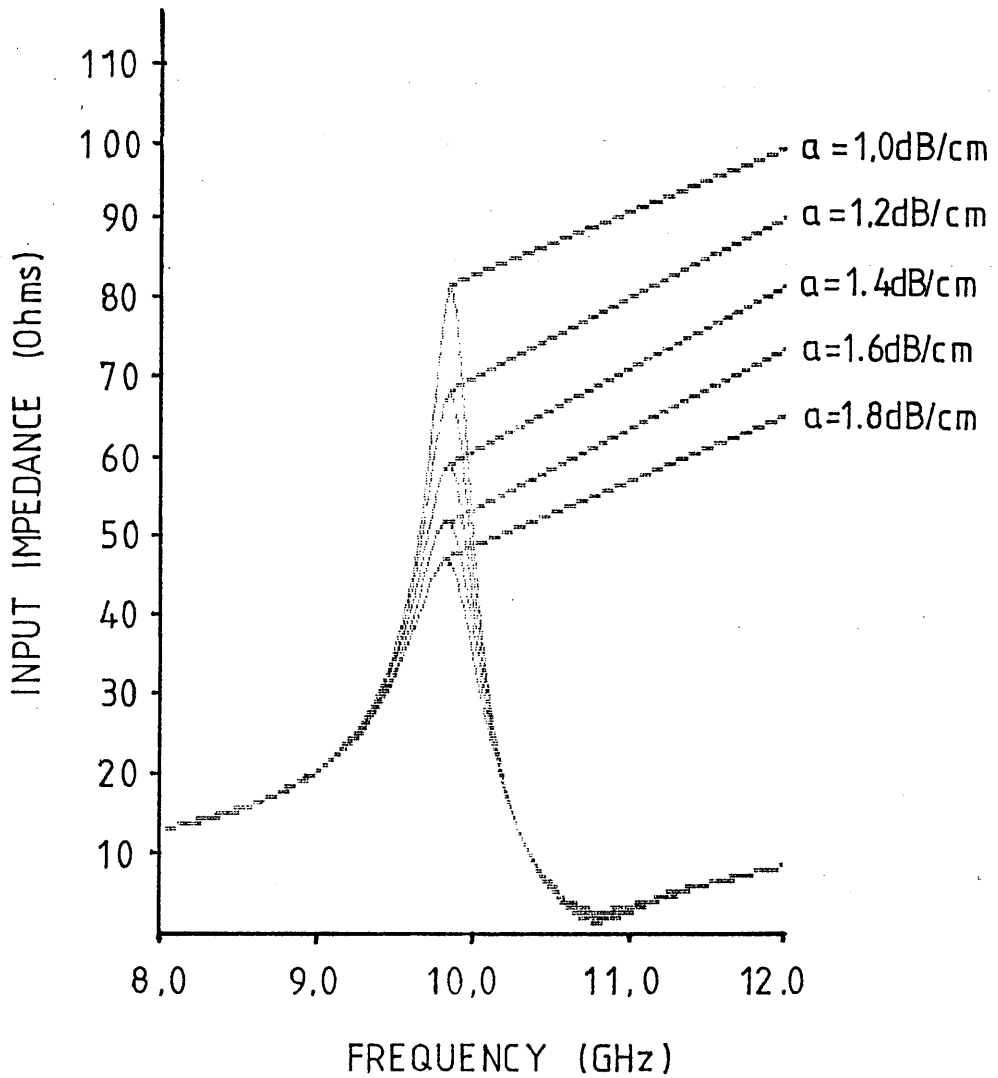

Tap position : 300um
Line length : 3600um
Z_0 : 50Ω

FIG.3.4b. Input impedance as a function of the attenuation constant.

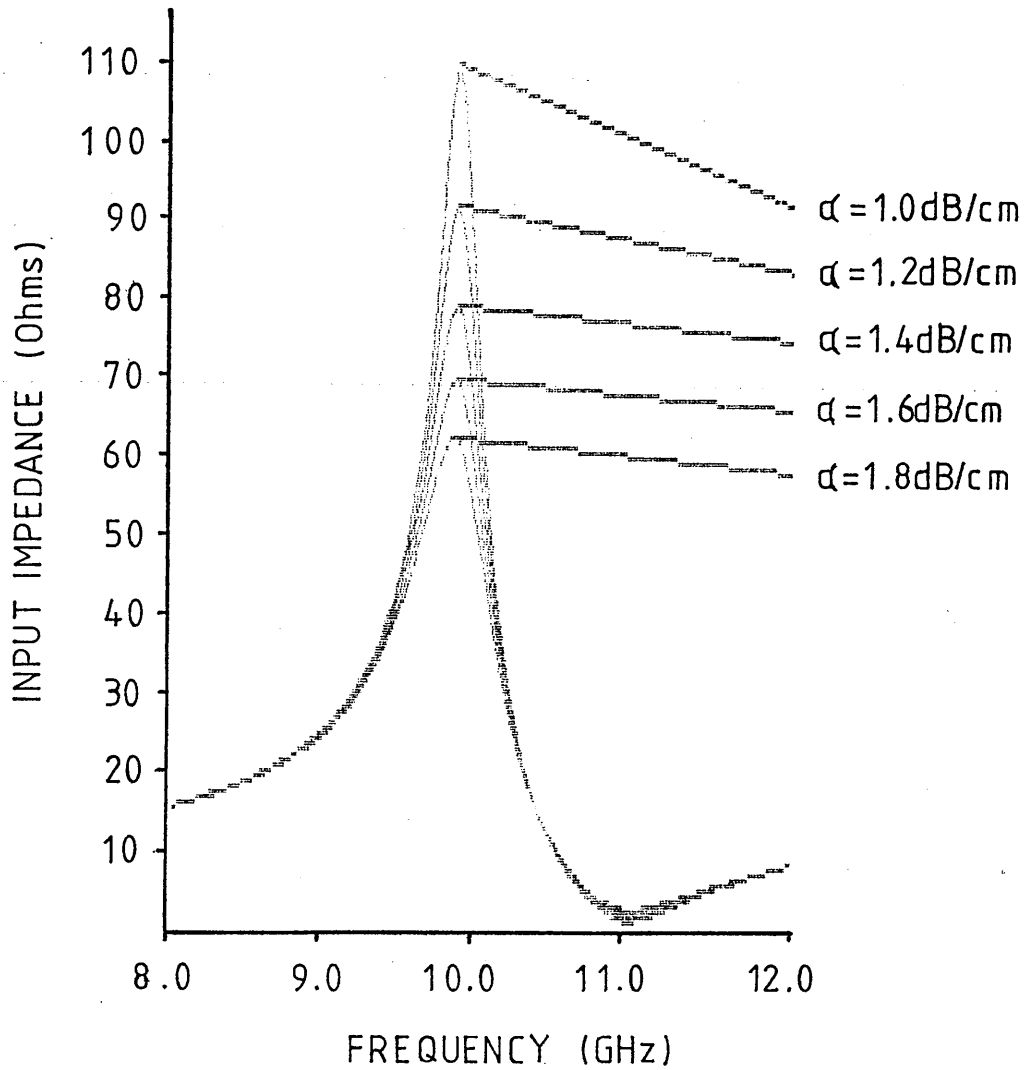

FIG.3.4c. Input impedance as a function of the attenuation constant.

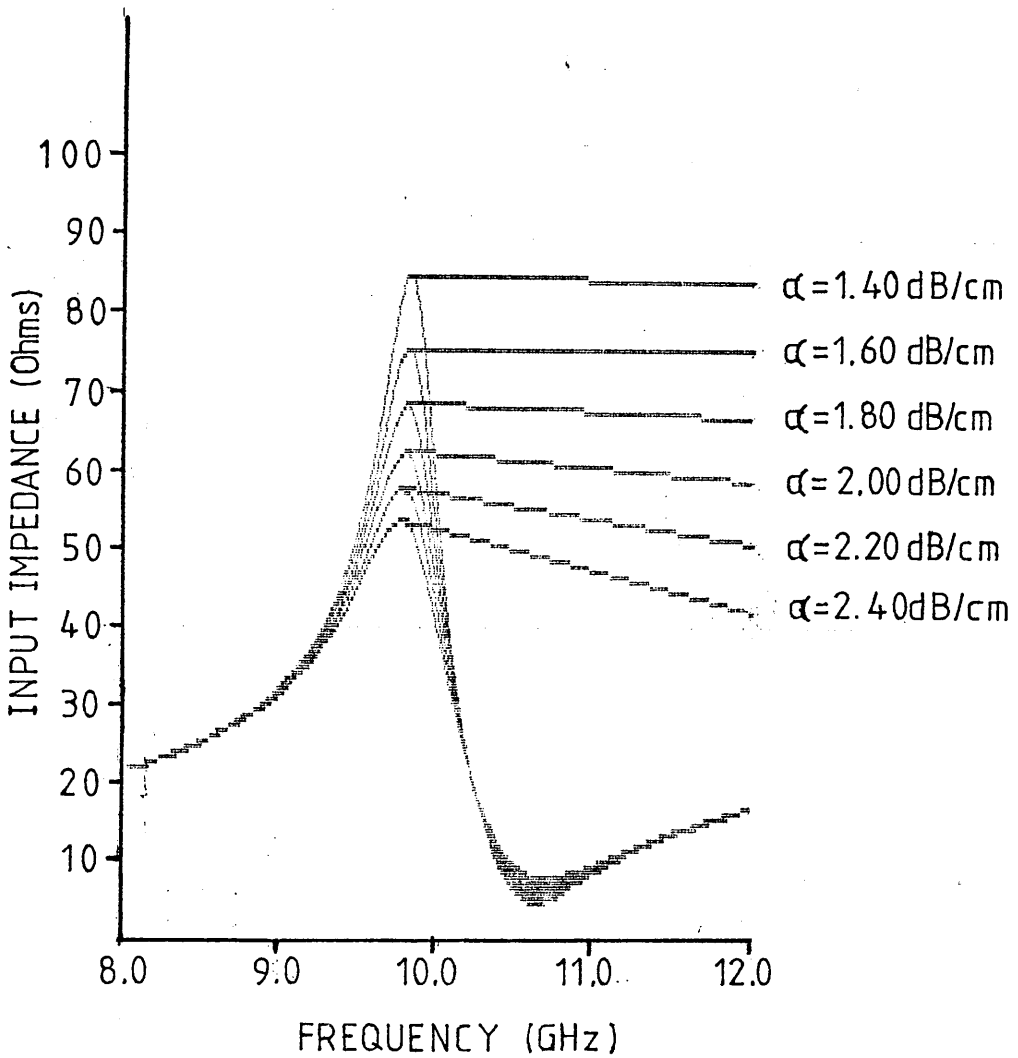

Tap position : 250 um

Line length : 3600 um

Z_0 : 100 Ω

FIG.3.4d. Input impedance as a function of the attenuation constant.

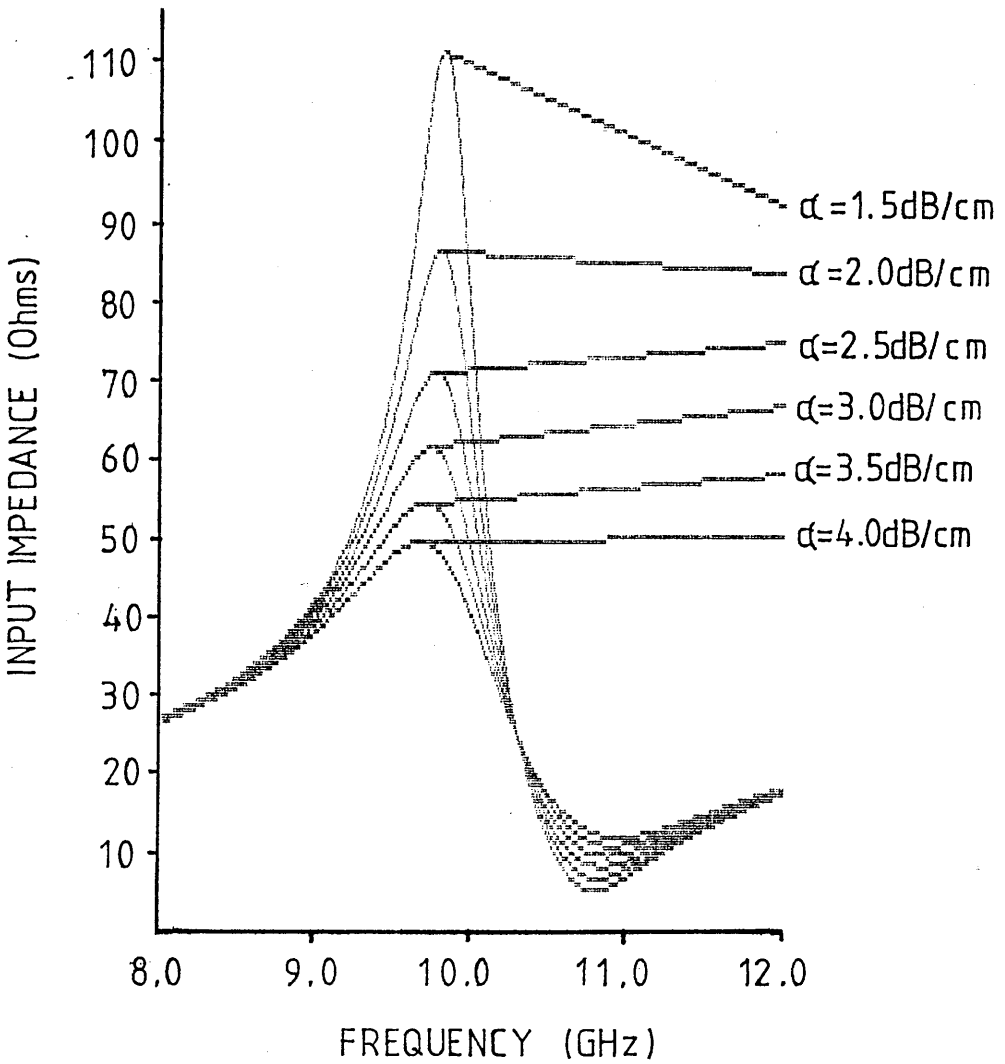

FIG.3.4e. Input impedance as a function of the attenuation constant.

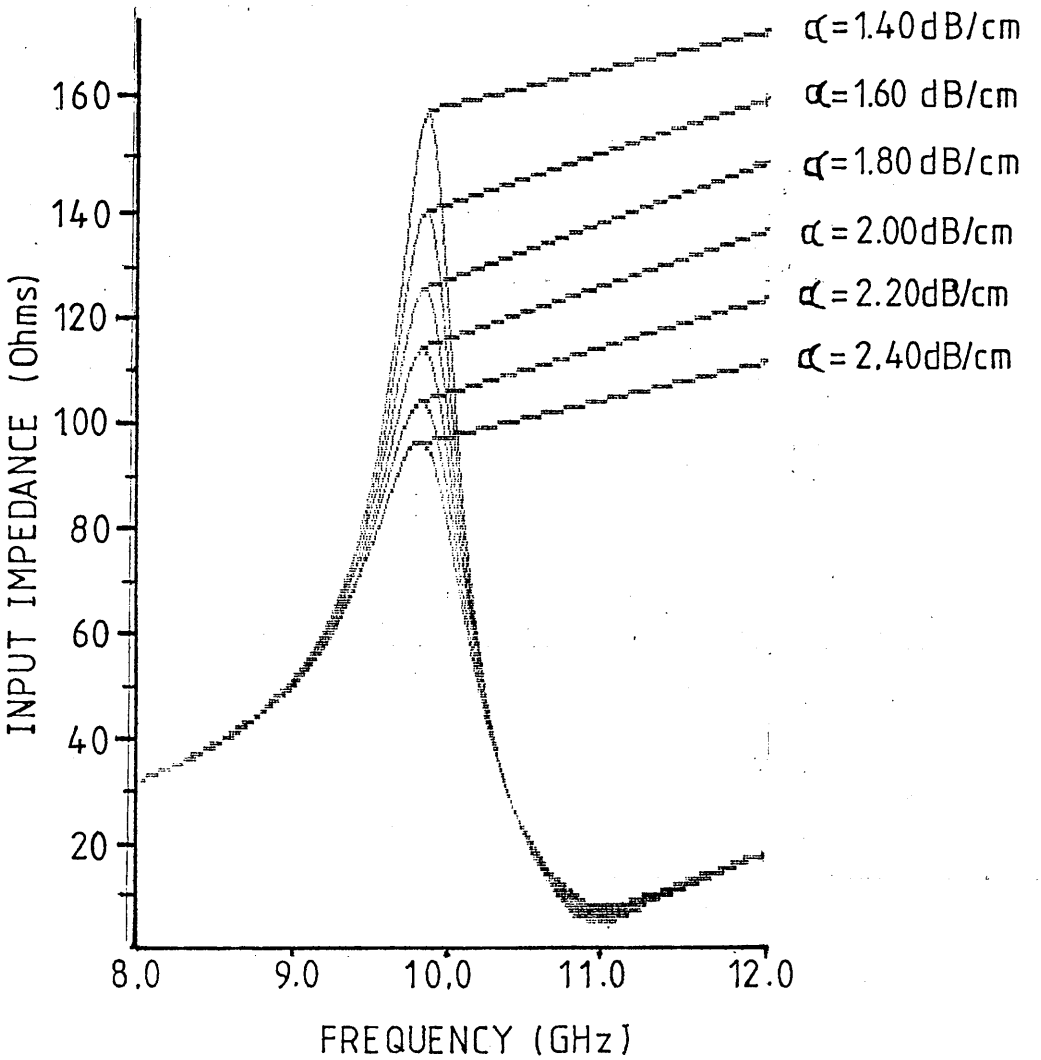

Tap position : 350um
Line length : 3600um
Z_0 : 100Ω

FIG.3.4f. Input impedance as a function of the attenuation constant.

input impedance arising from adjusting the characteristic impedance, the attenuation factor and the tap position on the resonant line.
Several points to note are :
(i) as the tap position approaches the centre the input impedance increases, however it is no longer real, and
(ii)the peak impedance decreases as the loss increases for any tap position,
(iii)the impedance also increases as the characteristic impedance increases.

The desired bandwidth and the operating frequency set the Q and therefore also define the attenuation constant and length of the device required (Equ.(3.10)). Therefore the tap position and characteristic impedance are the only variables remaining to adjust the input impedance. For a device to operate at 10GHz with a bandwidth of 1GHz (assuming that the microwave field encounters an effective dielectric constant of 17.4) the electrode structure has to be 3.6mm long and for a Q of 10 (loaded) the attenuation has to be 1.9dB/cm. The characteristic impedance of the line is chosen as 50Ω to coincide with the drive line impedance. The input impedance is then determined by varying the tap position along the resonant line to give as close a match to the drive line impedance as possible. The change in input impedance as a function of the tap position, attenuation constant and characteristic impedance of the resonant line is shown in figs.3.4. The ideal position from Fig.3.4 is about 300μm from one of the short circuits for a resonant line with a characteristic impedance of 50Ω .

3.3. PHASE MODULATION CHARACTERISTICS.

The phase characteristic of the guided optical beam is

modified through the electro-optic effect [8] (see Appendix A) produced by an applied voltage. The change in refractive index induced is directly proportional to the modulating voltage and is given to a first approximation by:

$$\Delta n = \frac{r}{2} n_o^3 . \Gamma . \frac{|V|}{g} \qquad (3.26)$$

where $\frac{|V|}{g}$ is the electric field strength across the optical waveguide and Γ is a positive number less than or equal to 1. The significance of Γ is that it describes the degree of overlap between the electric and optic fields within the optical waveguide. The factor is very dependent upon the geometry of the electrode structure and the optical field mode profile within the optical waveguide. Although various attempts have been made at computing this parameter [9], the only reliable method of evaluation is through empirical measurements. The other term appearing in Equ.(3.35) is 'r' -a general electro-optic coefficient which is dependent upon the material, waveguide orientation, guided mode polarisation and the direction of the applied electric field.

3.3.1. BANDWIDTH OF STANDING WAVE MODULATOR.

Although the device described has a narrow bandwidth (compared to the travelling wave modulator) it is important to know for design purposes if the bandwidth is limited by the microwave bandwidth or by a transit time phenomenom. Transit time mismatch becomes important for long travelling wave devices [10] at high frequency operation due to the 'walk-off' between the group velocities of the microwave and optical fields, which results in a beat-like interference between the waves. When the fields are velocity matched, an optical phase

front encountering the modulating electric field is subject to the same voltage over the entire interaction length. If the phase velocity is slightly different, the optical phase front will move relative to the voltage phase front and thus encounter a change in the modulating voltage over the interaction length. In the worst case the average voltage may be zero, with no net modification to the phase fronts of the guided beam.

For the standing wave modulator there is a spatial variation in the electric field but there is no phase variation along the length of the device at resonance. However, there will still be a variation in the average voltage encountered by the optical phase fronts, due to the transit time of these phase fronts and the time variation of the standing wave pattern. The effect may significantly reduce the effective modulating voltage to such a degree that it is the main factor limiting the device performance.

From the previous argument the transit time limitation may be important in affecting the average voltage and so this possibility will now be analysed.

Simple expressions can be derived for the average voltage along the resonant line at resonance. At frequencies other than resonance, numerical methods must be used in calculating the voltage distribution. The voltage along the line at resonance will be considered first. The electric field (for the low-loss case) in the standing wave modulator may be described by:

$$V = V_0 \cdot e^{j\omega_m t} \cdot \sin\beta z \qquad (3.28)$$

The electric field distribution may change substantially

with time as the optical phase front progresses along the length of the interaction region and is included in the analysis by replacing 't' by the transit time factor:

$$t = t_o - t_d \tag{3.29}$$

where the optical phase front initially encounters the modulating voltage at time 't_o'. Then the instantaneous field at time 't' at any point along the structure is given by:

$$V(z,t) = V_o . e^{j\omega_m t_o} . e^{-j\omega_m n_o z / c} . \sin\beta z \tag{3.30}$$

where n_o is the effective index encountered by the optical field. The expression may then used to calculate the average electric field value by integrating along the interaction length:

$$V_{av} = \int_0^l V(z,t) . dz \tag{3.31}$$

Evaluation of the integral is simplified if the complex exponential term is retained:

$$V_{av} = V_o . e^{j\omega_m t} . \int_0^l e^{-j\frac{\omega_m n_o z}{c}} . \sin\beta z . dz \tag{3.32}$$

Evaluation of Equ.(3.32) results in the following expression:

$$V_{av} = \frac{V_o . e^{j\omega_m t} . 2 . \cos\frac{\pi n_o}{2n_m} . \left[\cos\frac{\pi n_o}{2n_m} - j\sin\frac{\pi n_o}{2n_m}\right]}{\beta\left[1-\left(\frac{n_o}{n_m}\right)^2\right]} \tag{3.33}$$

On further manipulation the above reduces to :

$$|V_{av}| = \frac{V_o . 2 . \cos\frac{\pi n_o}{2n_m}}{\beta . \left[1-\left(\frac{n_o}{n_m}\right)^2\right]} \tag{3.34}$$

The behaviour of the $\cos(\frac{\pi}{2}x)/(1-x^2)$ terms for different values of the ratio n_o/n_m is depicted in Fig.3.5. From this plot the maximum value, at resonance, of the $\cos(\frac{\pi}{2}x)/(1-x^2)$ term occurs when x tends to zero i.e. $n_m >> n_o$. An indication that for the standing wave modulator the degree of modulation is enhanced by a mismatch between the effective indices of the optical and microwave fields.

The reduction in the average voltage as a function of the transit time delay away from resonance can be determined easily by applying Equ.(3.9) to the resonant structure and evaluating the combined impedance of two shorted transmission lines connected in parallel at different frequencies at every point along the line. The voltage distribution is then obtained by scaling the combined impedance to the actual input impedance at the feed-point (assuming a normalised voltage of 1), taking the quadrature component into account. The average voltage is then evaluated by simply performing a numerical integration along the whole length of the resonant line.

The transit time factor is then included by multiplying the voltage at each point by the factor $\cos(\omega_m n_o d/k)$ where 'd' is the distance from one end of the electrode structure. The variation in the average voltage is shown in Fig.3.6 for a resonant line length of 3.6mm for several different values of attenuation constant.

From Fig.3.6 the bandwidth at which the phase modulation is down by a factor of 0.707 (which is directly proportional to the average voltage) is not transit time limited. The bandwidth is simply given by the bandwidth of the resonant structure itself. This fact

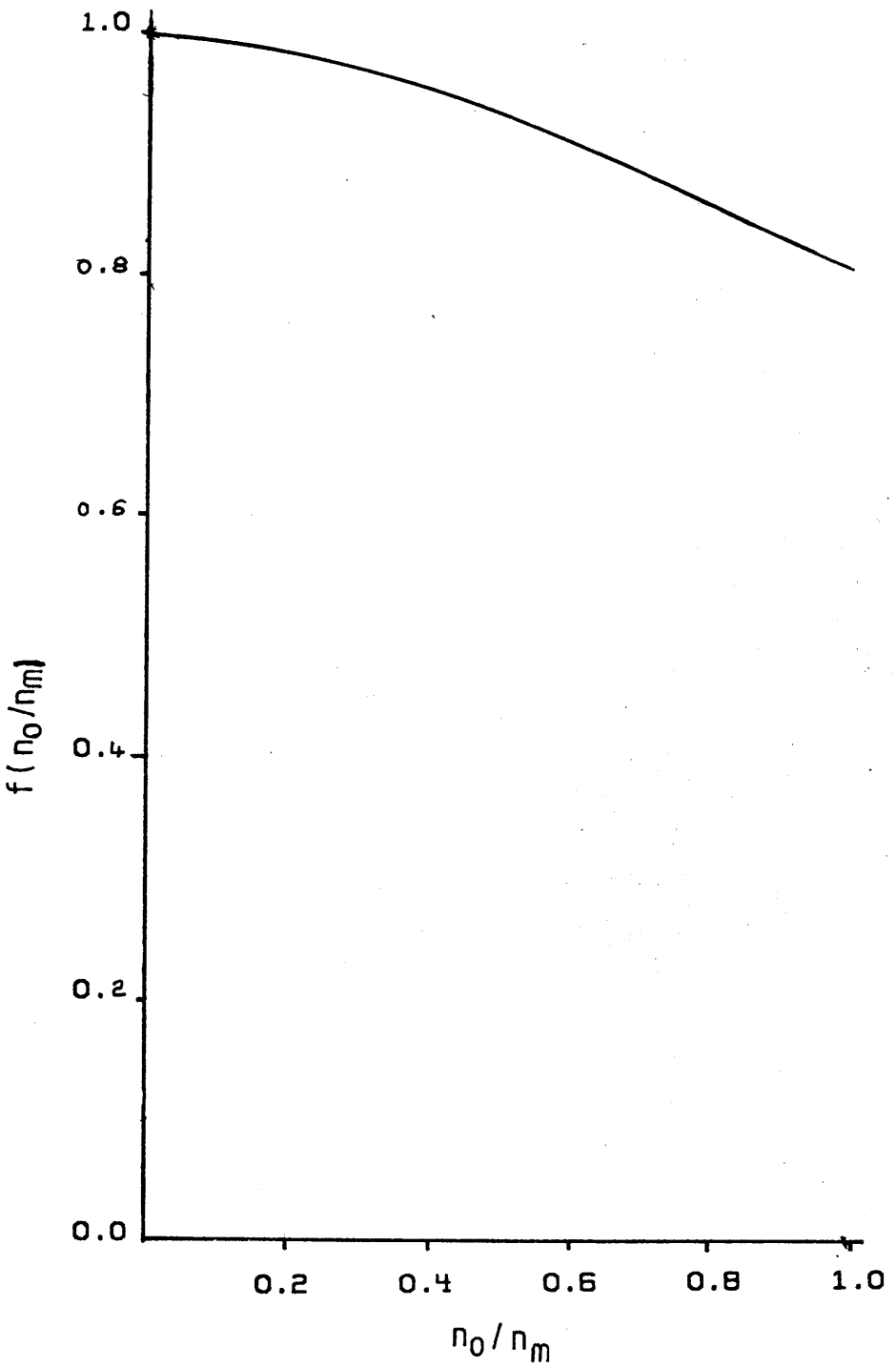

FIG.3.5. Transit time reduction factor.

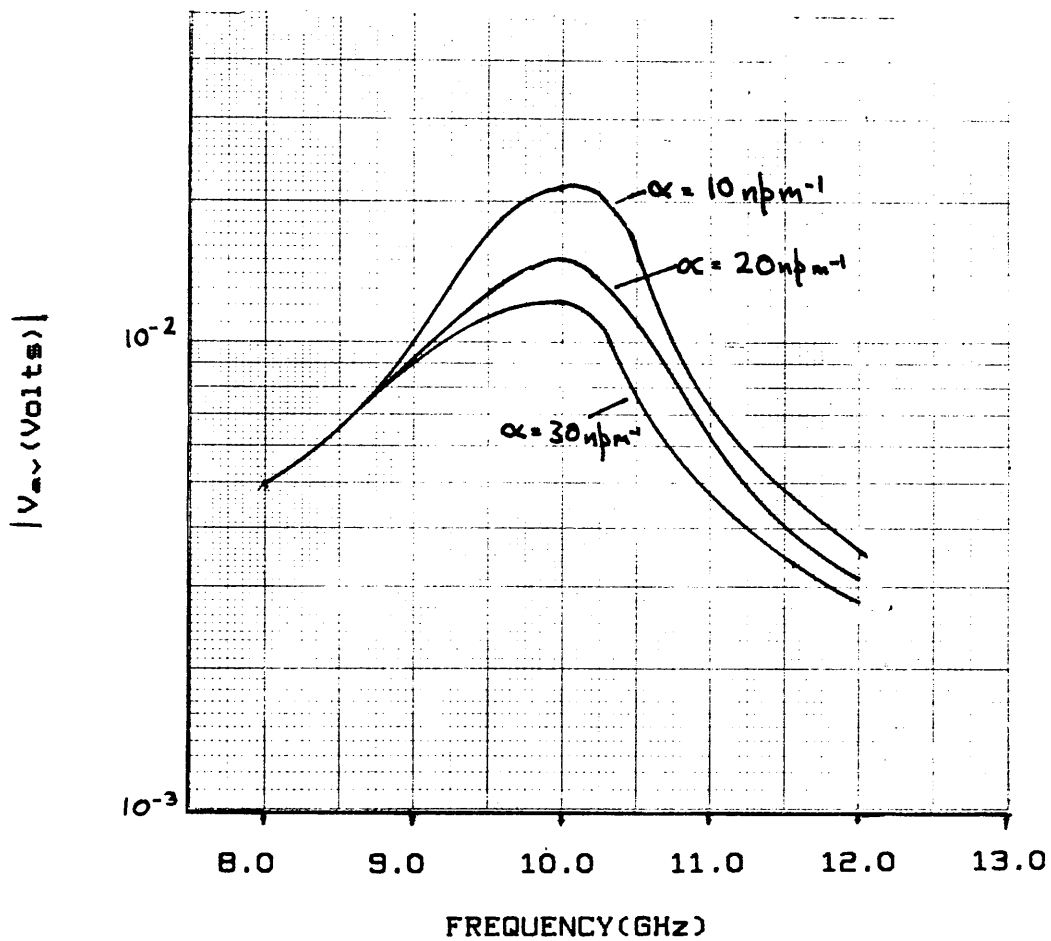

FIG.3.6. Average modulating voltage as a function of frequency and attenuation for the standing wave modulator.

allows the P/Δf figure to be calculated easily.

3.3.2. FIGURE OF MERIT FOR STANDING WAVE MODULATOR.

A useful figure of merit in characterising the performance of electro-optic modulators is the P/Δf figure [11], which gives the drive power per unit bandwidth to obtain a certain degree of modulation. The bandwidth is usually taken as the point where the modulation index has decreased by either 2 or $\sqrt{2}$ depending upon the convention used.

For the standing wave modulator the usual P/Δf figure is misleading in that it does not incorporate the voltage enhancement present in such a device. A more accurate figure of merit is the $(Vav)_{max}/\Delta f$ figure which does take into account this voltage gain.

The average voltage variation as a function of frequency calculated for the standing wave modulator is shown in Fig.3.6. The average voltage for the travelling wave structure may be readily calculated by simple integration of the voltage distribution along the electrodes. The voltage distribution along the travelling wave structure is [12]:

$$V(z,t_o) = V_o \cdot \sin\left[\frac{2\pi f_m n_m}{c}\left(1-\frac{n_o}{n_m}\right)z - 2\pi f_m t_o\right] \qquad (3.35)$$

where n_o and n_m have their usual definitions and t_o is the time at which a particular optical phase front enters the device. The average voltage is found by integrating Equ.3.35 along the electrode length i.e.:

$$V_{av}(z,t_o) = V_o \int_0^l \sin\left[\frac{2\pi n_m f_m}{c}\left(1-\frac{n_o}{n_m}\right)z - 2\pi f_m t_o\right] dz \qquad (3.36)$$

or:

$$V_{av}(z,t_0) = V_o \cdot \frac{\sin X \cdot l}{X} \cdot \sin[2\pi f_m t_0 - X] : X = \frac{\pi f_m l n_m}{c}\left(1 - \frac{n_o}{n_m}\right) \qquad (3.37)$$

The second sine term may be replaced by 1. This expression includes transit time limitations as well.

In contrast to the case of a small P/Δf figure, a small Vav/Δf indicates a small modulating voltage and/or a large bandwidth. When using this alternative figure the bandwidth definition used must be stated clearly.

Evaluating Equ.3.37 with l=3.6mm, $n_o/n_m \sim .53$ and f=0 gives Vav=$3.6.10^{-3}$ for the travelling wave modulator. The frequency at which this parameter is reduced by 0.707 is approximately 19GHz, producing a Vav/Δf of $1.9.10^{-13}$V/Hz. Using Fig.3.6 the corresponding value for the standing wave modulator is $1.6.10^{-11}$V/Hz which is some 84x better. The equivalent P/Δf values are 2.10^{-11}W/Hz and 10^{-12}W/Hz for the standing and travelling wave devices respectively. This clearly illustrates the variation in comparisons for different figures of merit.

The phase change for both devices is given by:

$$\Delta\beta = -\frac{\pi n_o^3 r \Gamma V_{av}}{\lambda g} \qquad (3.38)$$

where V_o in Equ.3.35 is a normalising factor related to the microwave drive power and g is the separation between conductors.

3.4.0. MICROWAVE WAVEGUIDE ANALYSIS.

At this point it is necessary to consider the type of

microwave transmission line employed in forming the electrode structure. The main prerequisite for the electrode structure is the ease in which external circuit elements, such as short circuits, can be readily realised. For the short circuited line discussed here, the most useful form of microwave frequency waveguide is the symmetric and asymmetric coplanar waveguide structure, where the centre conductor and ground conductor are in the same plane, as illustrated in FIG.3.7a. Asymmetric coplanar waveguide structures have received considerable attention, yet there is still some uncertainty over the correct dimensions to obtain 50Ω and the theoretical attenuation constant. For example, Izutsu et al. [13] state that a conductor width to separation ratio of 0.6 is necessary to achieve 50Ω with asymmetric coplanar waveguide. Gee et al. [14] and Kubota et al. [15] predict values between 0.5 and 1 for the ratio. Molter-Orr et al. [1] failed to achieve a 50Ω match at all.

In order to resolve these ambiguities and to estimate the conduction losses, the waveguide structure was analysed by a numerical method and results compared with those for the methods used by other researchers i.e. conformal mapping techniques [16,17,18].

The characteristic impedance is calculated by assuming a T.E.M. field distribution and then applying conformal mapping techniques [16,17] to the electrode structure. The Schwartz-Christoffel transformation is used to map the electrode structure onto the sides of a regular polygon in the transformed plane from which the capacitance may be calculated. It also assumes that the conductors are infinitely thin. Although the quasi-static T.E.M. field distribution is not entirely

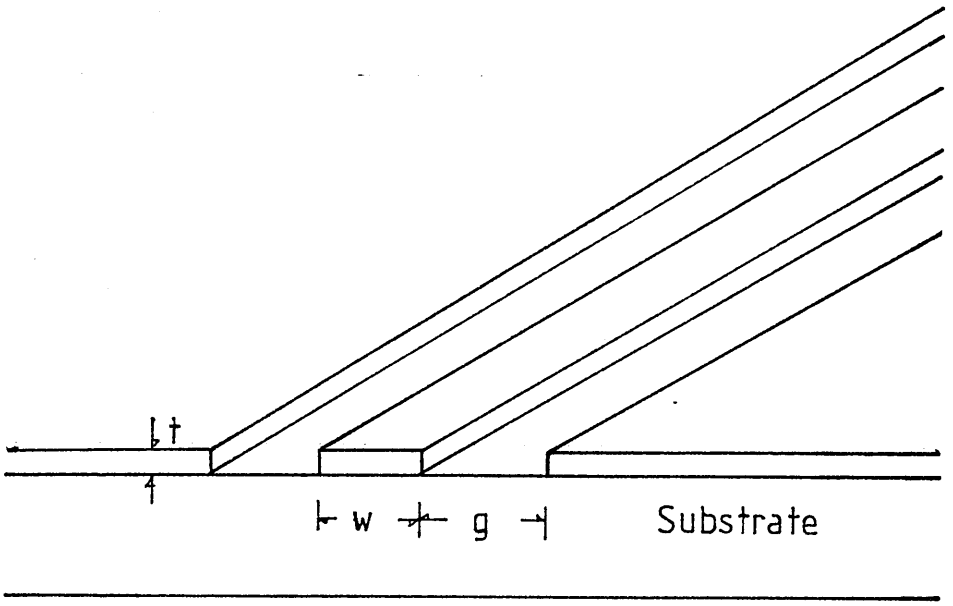

Symmetric Configuration

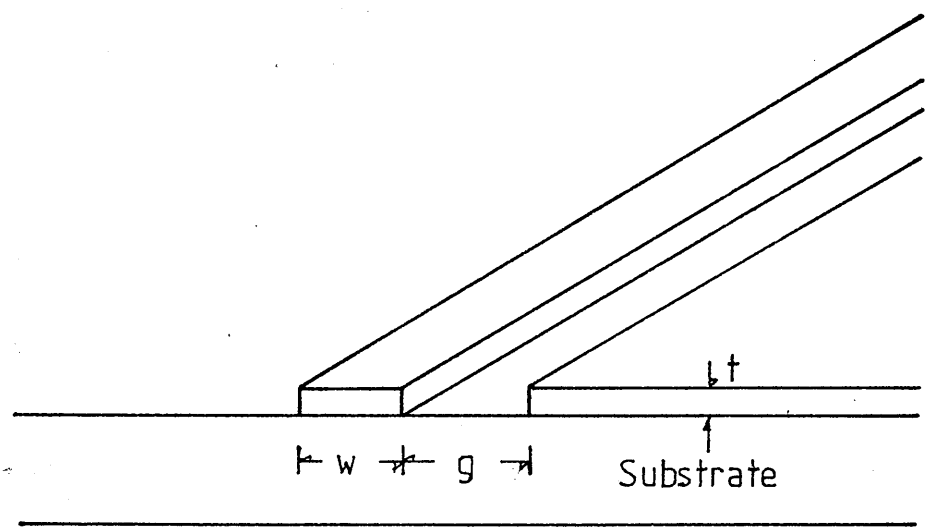

Asymmetric Configuration

FIG.3.7a. Symmetric and asymmetric coplanar waveguide (C.P.W.) geometries.

rigorous for a wave propagating along this structure at frequencies above 4GHz, the difference between the theoretical and experimental values does not warrant any complex modification to the theory [19]. The characteristic impedance is then given by:

$$Z_o = \frac{1}{C_o v_{ph}} \qquad (3.39)$$

Where V_{ph} is the phase velocity and C_o is the distributed capacitance.

In both waveguide configurations the characteristic impedance is governed by the ratio of two elliptic functions (obtained from the transform procedure):

$$Z_o = \frac{30\pi . K'(k_s)}{\sqrt{\frac{\epsilon_r+1}{2}} . K(k_s)} \qquad (3.40a)$$

for the asymmetric case and:

$$Z_o = \frac{240\pi . K(k_a)}{\sqrt{\frac{\epsilon_r+1}{2}} . K'(k_a)} \qquad (3.40b)$$

for the symmetric case where:

$$k_s = 1/(1+\frac{2g}{w}) \qquad (3.41a)$$

$$k_a = [1/(1+2\frac{w}{g})]^{-1/2} \qquad (3.41b)$$

$$K'(a) = K(\sqrt{1-a^2}) \qquad (3.41c)$$

K(x): elliptic integral of the first kind.

w: central electrode width.

g: spacing between central electrode and ground plane.

ϵ_r: dielectric constant of $LiNbO_3$.

For a characteristic impedance of 50Ω throughout, the ratio w/g for the asymmetric case has to be approximately 0.6 (in agreement with Izutsu et al. [13]) while that of the symmetric configuration is approximately 0.7. In fact, the characteristic impedances of both configurations are reasonably insensitive to variations in the ratio w/g close to 1, as Fig.3.7b illustrates. As the characteristic impedance is solely a function of the ratio between the electrode width and the separation, it is possible to maintain the same impedance by using a tapered structure on the same substrate. This facilitates the scaling of the external microwave dimensions to those of the planar resonant electrode dimensions. This technique was used to taper the dimension of the semi-rigid coaxial cable (centre core diameter .085in) down to 15μm.

The final parameter that has to be derived is the attenuation factor α for the asymmetric coplanar waveguide. No formal solutions are available for calculating the attenuation factor although numerous empirical formula based on experimental observations do exist.

To calculate the theoretical attenuation constant for the asymmetric coplanar waveguide a computer program using the finite difference technique was written to solve Laplace's equation [20].

$$\frac{\partial^2\phi}{\partial x^2} + \frac{\partial^2\phi}{\partial y^2} = 0. \qquad (3.42)$$

This is similar in some respects to the conformal mapping method in that it assumes a quasi-static T.E.M. approximation for the guided wave.

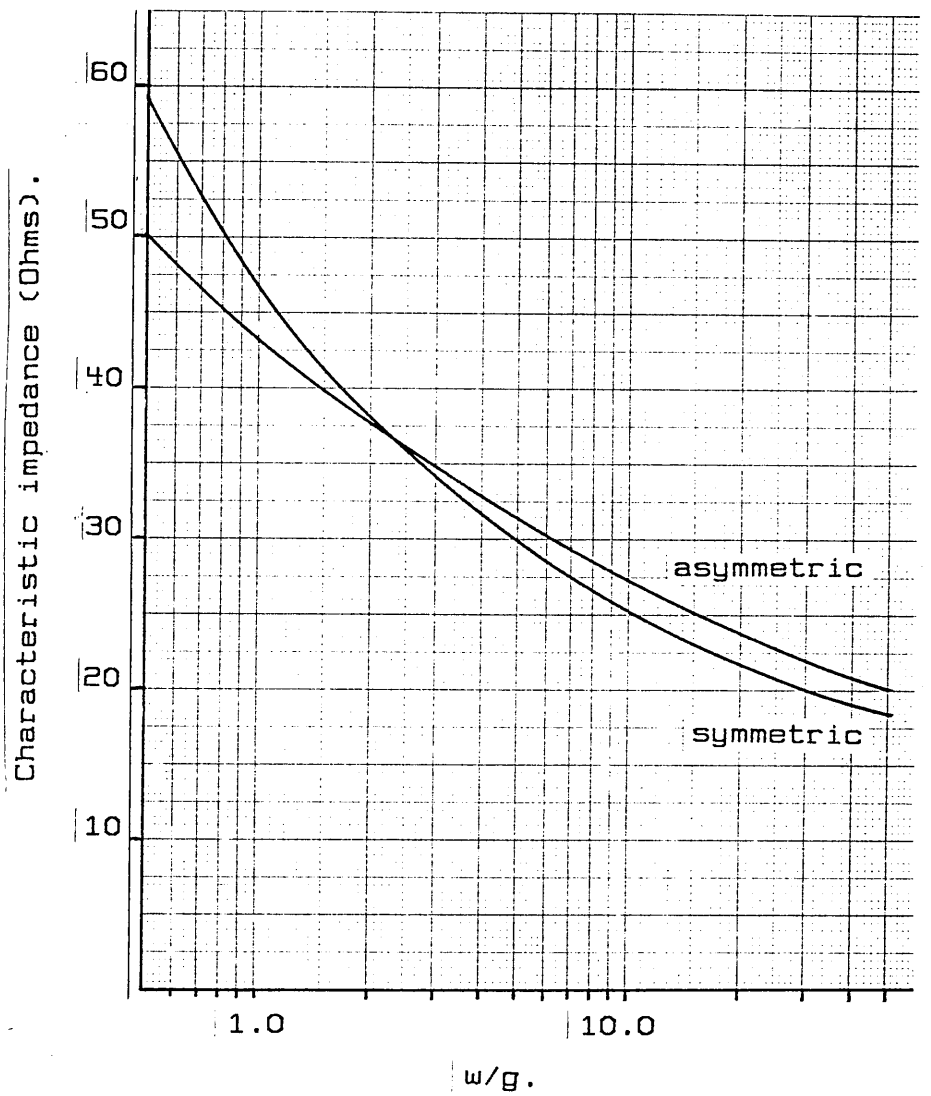

FIG.3.7b. Characteristic impedance of symmetric and asymmetric C.P.W. calculated by conformal mapping.

The numerical solution of Laplace's equation is a boundary value problem: the field or potential distribution within a closed region is sought subject to the potentials present on the boundaries. Once the field distribution has been obtained, the capacitance, surface current and hence the attenuation constant can be found.

The problem modelled is shown in Fig.3.8, where the boundaries are sufficiently far removed from the electrode that the fields may be taken as approximately zero. If this is not entirely true, the continuity of the first derivative of the field across the boundary is used. The right hand vertical boundary acts as a reflection plane in calculating the parameters for the symmetric coplanar waveguide. For the asymmetric case this boundary is removed from the central electrode until it is at a point sufficiently far away for the field to be approximately zero.

The field distribution is found by dividing the region into a mesh of discrete points. The potentials at the boundaries and conductors are assigned the relevant values and an iterative process is carried out to find the field at each point. (The finite-difference method is described in greater detail in Chapter 2 Section 5.1). This procedure is repeated until convergence is achieved. An acceleration factor is usually employed to give successive over-relaxation which decreases the number of iterations required.

The iterative procedure is initially performed on a coarse mesh which is subsequently refined around the area of particular interest. A mesh size of 50x50 was used to analyse the waveguide structure of Fig.3.8. The

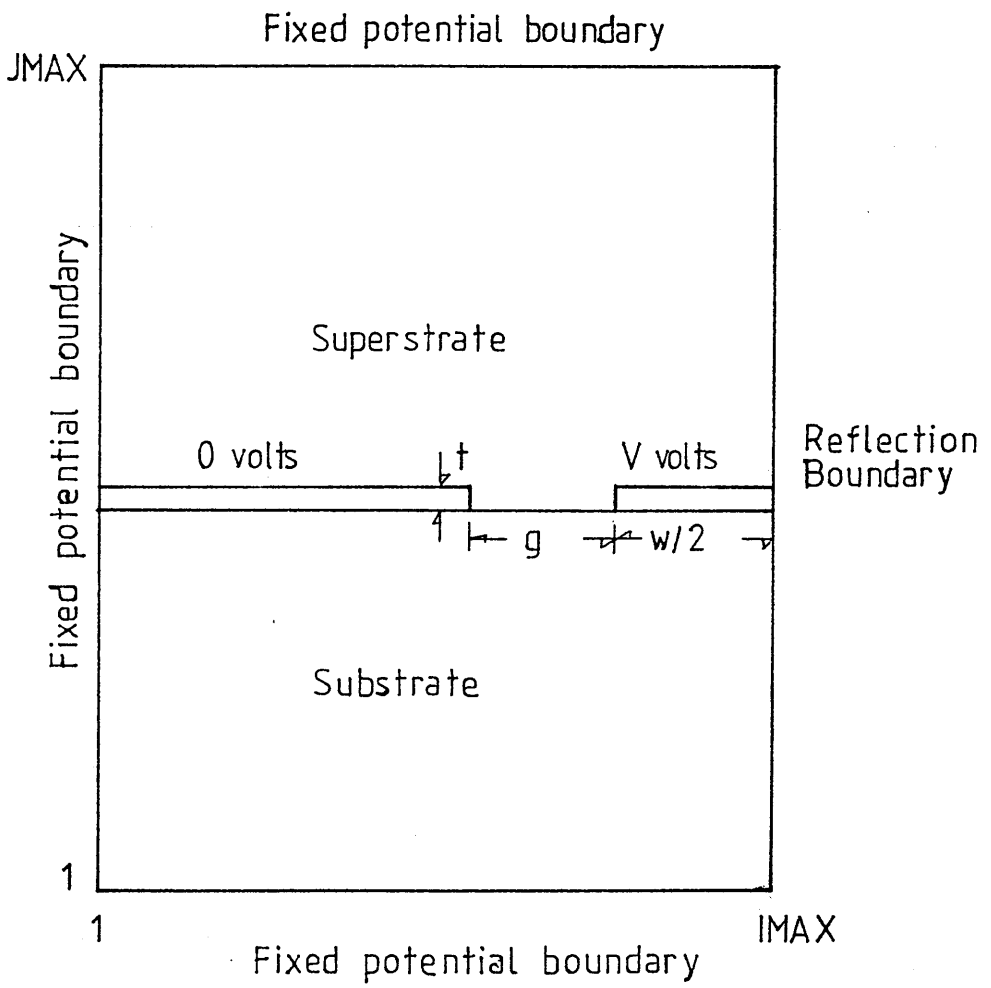

FIG.3.8. Region of space for numerical analysis of coplanar waveguide.

capacitance was then found by applying Gauss's law to a closed contour around the central electrode to obtain the total charge:

$$Q_T = \sum_n^1 Q_n = \sum_n^1 D_n A_n \qquad (3.43)$$

from which the capacitance per unit length may be calculated:

$$C_T = \sum_n^1 \frac{Q_n}{V} \qquad (3.44)$$

In a similar manner the surface currents can be found by using the T.E.M. approximation:

$$I = \sum_n^1 A_n D_n \cdot /(Z_0 C_T) \qquad (3.45)$$

and then the effective resistance per unit length is:

$$R_{s\,eff} = \frac{2R_s}{I^2}\left[\sum_n^1 A_n \cdot \left(\frac{D_n}{Z_0 C_T}\right)^2\right], \qquad (3.46)$$

from which α may be found (Equ.3.8a).

Values obtained by this method are shown in Fig.3.9 and 3.10 for the characteristic impedance and the attenuation constant. The results obtained for the characteristic impedance using both techniques coincide for t/g=0, although some fluctuation was observed due to the choice of mesh spacing. It is evident from these graphs that a ratio for w/g has to be achieved which both minimises the attenuation constant and optimises the characteristic impedance. A further constraint is imposed by maximising the overlap between the electric and optical field, which limits the gap separation to approximately the same dimension as the optical waveguide [13].

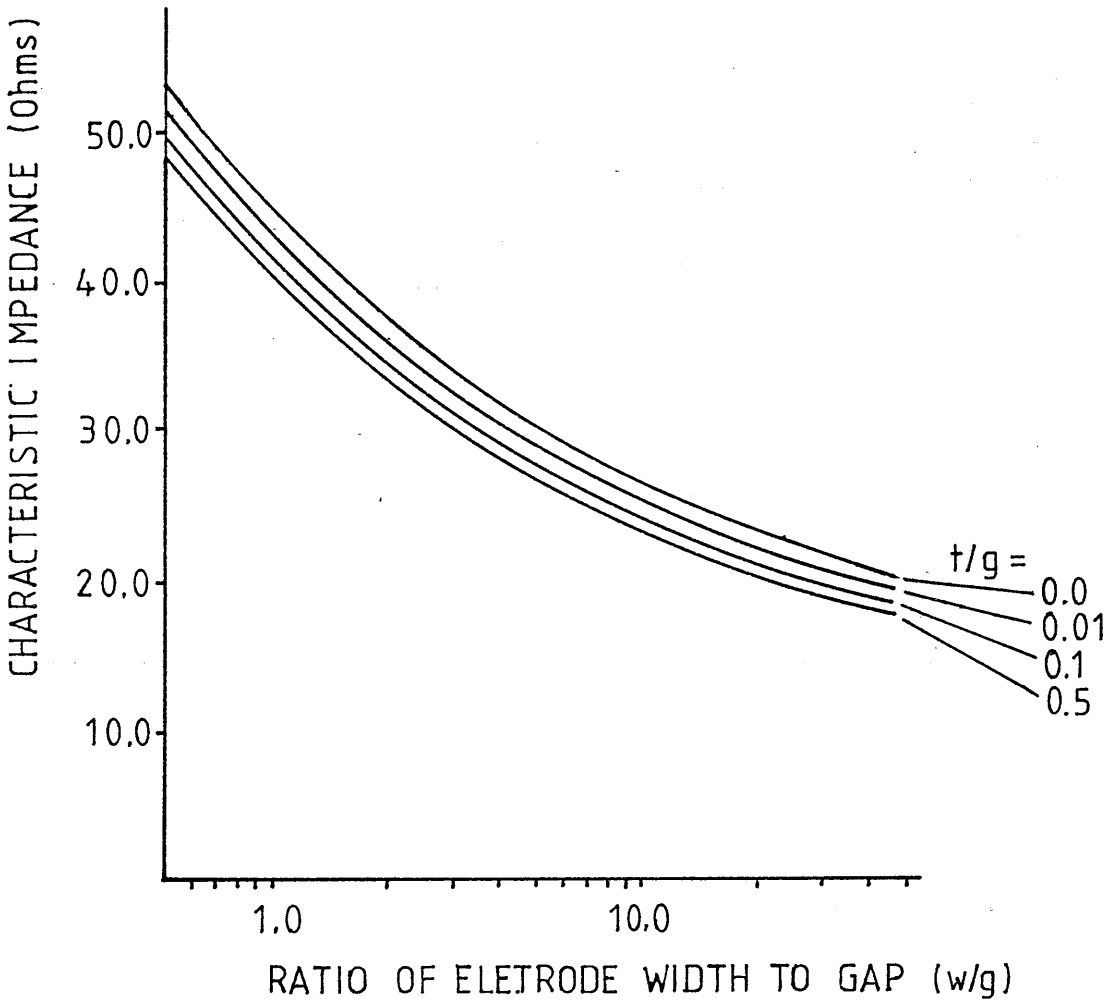

FIG.3.9. Characteristic impedance for asymmetric C.P.W. as a function of w/g and t/g (ϵ_r=18).

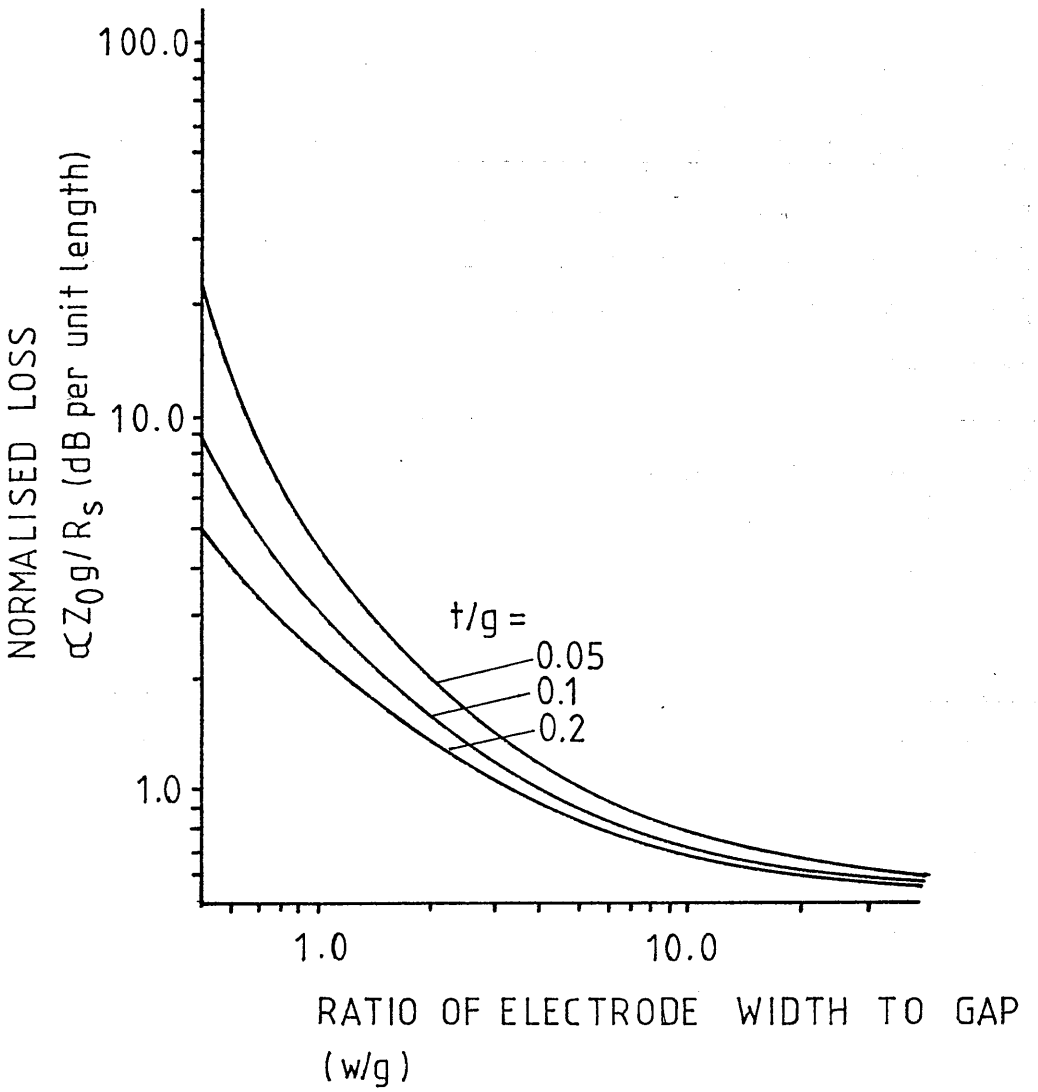

FIG.3.10. Normalised loss for asymmetric C.P.W. as a function of w/g and t/g (ϵ_r=18).

With these limitations, the ratio w/g was taken as 1 which, from Fig.3.9, gives a characteristic impedance of 46Ω . Trying to achieve 50Ω would involve reducing w/g, which in turn would dramatically increase the attenuation. The attenuation constant for w/g=1 is approximately 2dB/cm but this value can be altered somewhat by adjusting the metal thickness. The characteristic impedance is also influenced by the metal thickness but it is not as sensitive as the attenuation constant. For an aluminium thickness of 1.8μm, (assuming that the high frequency surface resistivity can be expressed as 0.0326$\Omega/\square$) corresponding to a t/g value of 0.2 gives an attenuation constant of 1.9dB/cm. The dimensions of the structure are therefore set at a central conductor width of 10μm, separated from the ground plane by 10μm. The thickness of the evaporated film would need to be greater than 1.5μm. Of course films with a gretaer surface resistivity can be used but the ease of evaporating aluminium dismisses these. With these values for the attenuation and propagation constant Equ.3.10 predicts a Q value of 10.

From this section, values calculated for the attenuation factor are used in Appendix B to derive the theoretical heating effects associated with r.f. attenuation along each electrode structure. A comparison is also included between the drive power requirements for travelling and standing wave modulators for the same induced optical phase change of π radian at λ=0.633μm. The value of 0.5mW in the standing wave case compares very favourably with the 300mW required for the travelling wave case.

SUMMARY

The object of this chapter was to provide the basic principles involved in the design of the standing wave modulator. The analysis throughout has been kept as general as possible to facilitate applications to other electrode configurations and operating frequencies. The basic conclusion to be reached was that the modulator bandwidth is dependent upon the characteristics of the microwave transmission line only. In contrast to the travelling wave modulator, a mismatch between the effective indices of the microwave and optical fields enhances the overall average voltage encountered in a standing wave modulator.

In general the response is principally dictated by the metal film thickness used for the electrode Equ.2.34. In comparison with the travelling wave modulator the standing wave modulator offers a somewhat lower $P/\Delta f$ figure. It has been shown that a more applicable figure of merit is the $V_{av}/\Delta f$ figure which indicates the increase in the maximum induced phase change by the resonant mode of operation. A method for analysing coplanar waveguides and for calculating the transmission line parameters has been presented and this has been compared with other reported results.

References Chapter 3.

[1] L.A.Molter-Orr, H.A.Haus and F.J.Leonberger.
20GHz Optical Sampler.
I.E.E.E. J. Quant. Electrs.,VolQE19(12),1983.
pp. 1877-1883.

[2] Ramo, Whinnery and Van Duzer
Fields and waves in communications electronics.
John Wiley and Son, 1965.
Chapter 1.

[3] D.F.Clark, A.C.G.Nutt, M.R.S.Taylor and
R.M.De La Rue.
Design procedure and experimental
characterisation of a standing-wave electrode
electro-optic modulator.
I.E.E. Colloquium, London, January 1986.

[4] M.Izutsu, Y.Yamane and T.Sueta.
Broadband travelling wave modulator using a
$LiNbO_3$ optical waveguide.
I.E.E.E. J. Quant. Electrs.,Vol.QE13(4),1977.
pp.287-290.

[5] E.L.Ginzton.
Microwave Measurement.
McGraw Hill, 1957.
Chapter 9

[6] A.Rauber.
Chemistry and physics of Lithium Niobate.
Current topics in material science.
Vol. 1, Chapter 7.
F.Kaldis, ed.

[7] H.A.Haus.
Waves and fields in Optoelectronics.
Prentice-Hall, 1984.
Chapter 7.

[8] A. Yariv.
Introduction to Quantum Electronics.
Holt, Reinhart and Wilson, 1976.
Chapter 1

[9] D. Marcuse.
Optimal electrode design for integrated optics modulator.
I.E.E.E. J. Quant. Electrs.,Vol.18(2),1982.
pp.393-398.

[10] R.C.Alferness.
Waveguide electro-optic modulators.
I.E.E.E. Trans. Microwave Theory and Tech.
Vol.M.T.T.30(8), 1982, pp.1121-1137.

[11] M.Izutsu, Y.Yamane and T.Sueta.
Travelling wave modulator with optical waveguide.
1977 Int. Conf. Integrated Optics and Optical Fibre Communications.
A 9-2 Tokyo July, 1977.

[12] R.C.Alferness, S.K.Korotky and E.Marcatili.
Velocity matching techniques for integrated optic travelling wave switch/modulators.
I.E.E.E. J. Quant. Electrs.,Vol.QE20(3),1984.
pp.301-309.

[13] M.Izutsu, T.Itoh and T.Sueta.
10GHz bandwidth travelling wave $LiNbO_3$ optical waveguide modulator.
I.E.E.E. J. Quant. Electrs.Vol.QE14(6),1978.
Vol.QE-14(6).

[14] C.M.Gee, G.D.Thurmond and H.W.Yen.
Travelling wave electro-optic modulator.
Appl. Opt.,Vol.22(13),1983.
pp.2034-2037.

[15] K.Kubota J.Noda and O.Mikami.
Travelling wave optical modulator using a directional coupler $LiNbO_3$ waveguide.
I.E.E.E. J. Quant. Electrs.,Vol.QE16(7),1980.
pp.754-760.

[16] O.G.Ramer.
Integrated optic electro-optic modulator electrode analysis.
I.E.E.E. J. Quant. Electrs.,Vol.QE13(4),1977.
pp.152-158.

[17] Pao-Lo Liu.
Bandwidth, field distribution and optimal electrode design for waveguide modulators.
J. Appl. Phys.,Vol.53(10),1982.
pp.6681-6686.

[18] C.P.Wen.
Co-planar waveguide: a surface strip transmission line suitable for non-reciprocal gyromagnetic device applications.
I.E.E.E. Trans. Microwave Theory and Techs.
Vol.M.T.T.17(12), 1969, pp.1087-1090.

[19] Gupta, Garg and Bahl.
Microstrip lines and slotlines.
Artek Press, 1982.

[20] K.Koshiji, E.Shu and S.Miki.
Simplified computation of co-planar waveguide with finite conductor thickness.
I.E.E. Proc. H., Vol.130, 1983.
pp.315-321.

CHAPTER 4.

OPTICAL WAVEGUIDE DEVICE FABRICATION IN $LiNbO_3$ AND GaAs.

4.0. INTRODUCTION

Integrated optical 'circuits' may eventually become a routine part of any optical network and to this end the behaviour of optical waveguides for different waveguide fabrication conditions has to be characterised. The characterisation is necessary to ensure reproducibility between production runs and to determine the sensitivity of device performance to each of these different parameters. The dependence of the device performance upon fabrication conditions is best observed by altering only one condition between each production cycle. From the difference observed in the experimental behaviour, the manifestation of a particular characteristic due to changing this parameter will be easily recognisable, and this may then be explained through a simple theoretical model.

The most widely used material to date for the manufacture of integrated optic devices is $LiNbO_3$ [1]. This has arisen due to the numerous advantageous physical properties that the crystal exhibits. The most potentially useful properties for integrated optics are the piezoelctric effect [2], the large electro-optic effect [3], optical non-linearities [4], the pyroelectric [5] and photovoltaic effects [6]. It is also optically transparent from 0.35μm upto 5μm [7], but its usefulness at visible wavelengths (~0.633μm and shorter) is limited by the photovoltaic effect, which is the main cause of optical damage at visible wavelengths for low powers ($<10 Wcm^{-2}$).

Several methods are available for forming optical waveguides in $LiNbO_3$, the most common of which is the in-diffusion of titanium [8,9,10,11] into $LiNbO_3$ for fabricating low loss optical waveguides with losses less than ~0.2dB/cm. The incorporation of titanium atoms into the crystal lattice during the diffusion process leads to a localised increase in the local refractive index. The diffusion process is usually carried out at an elevated temperature below the Curie temperature i.e. ~1000°C. Waveguides may also be formed by the out-diffusion of lithium from a region below the surface to produce a high index region [12,13] or by proton implantation [14].

Another method has recently emerged in which optical waveguides are formed by an exchange process carried out at a very much reduced temperature ~200°C [15]. This is the proton-exchange method and will be described in greater detail in Chapter 5. It is thought to be basically an ion exchange process between lithium atoms in the crystal lattice and protons present in the melt to produce the localised increase in the refractive index.

In general, the overall performance of an optical waveguide is very sensitive to variations during manufacture. For titanium in-diffused waveguides these include variations in the thickness and edge quality of the pre-diffusion titanium stripe layer. During diffusion, these irregularities are then diffused into the substrate replicating in some measure the original titanium film variation although, to a certain extent, the diffusion process smooths these irregularities out. These irregularities may lead to a degradation in the overall optical performance of the waveguide by providing width variations and scattering centres. Energy

propagating within the waveguide will be scattered, exciting other guided or substrate modes and leading to a lossy waveguide. This propagation loss will be over and above the intrinsic absorption loss of the material itself. In practice the most significant parameters affecting the overall propagation characteristics are the initial titanium thickness and the diffusion conditions.

For proton-exchanged waveguides the most sensitive fabrication aspects are the diffusion temperature and the exchange time. Methods do exist whereby the sensitivity to the exchange conditions is decreased. These other techniques involve using either proton-exchange in conjunction with titanium in-diffused waveguides or performing the exchange for a shorter time in either a dilute or concentrated melt followed by post-exchange annealing. The purity of the proton source and the number of samples exchanged in the same melt can all lead to a variation between runs. The other methods of forming optical waveguides in $LiNbO_3$ are beyond the scope of this thesis.

For active devices, metallic overlays for electrodes must be accurately positioned relative to the optical waveguide for the efficient utilisation of the desired electro-optic coefficients. Over and above the problems of alignment of the electrode pattern, in particular for the standing wave modulator the electrical properties of the metal film have to be considered to give the desired attenuation required for the particular bandwidth application. Any deviations from parallelism between the optical waveguide and the electrode structure will lead to mode conversion and to a reduction in the overall modulation efficiency.

The remainder of this chapter will be devoted to the experimental methods involved in the fabrication of passive devices (optical waveguides) and active devices (the standing wave modulator) along with a description of the modification to existing photolithographic techniques for developing the technology to pattern thick (~2μm) aluminium films.

4.1. WAVEGUIDE FABRICATION PROCEDURE.

The fabrication procedure required for the manufacture of optical waveguides formed by titanium in-diffusion can be conveniently described by the list below which is shown schematically in Fig.4.1. As a consequence of the physical dimensions of the devices the processing had to be carried carried out in a dust-free environment. The procedure is outlined below:

1. generation of the photolithographic pattern.
2. sample/substrate preparation.
3. pattern delineation using positive photoresist.
4. Ti deposition.
5. lift-off.
6. Ti diffusion.
7. end polishing.

For waveguides fabricated by other technologies (e.g. proton/ion exchange) this process has to be modified from step 3) onwards as follows (Fig.4.2):

3. Aluminium film deposition.
4. pattern delineation using positive photoresist.
5. etching of patterned aluminium.
6. immersion in a proton/ion source.

1. Clean substrate.

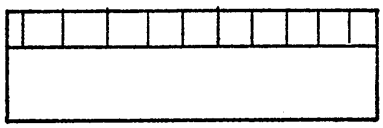

2. Coat with photoresist.

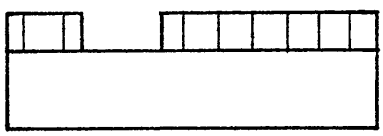

3. Expose and develop phototresist.

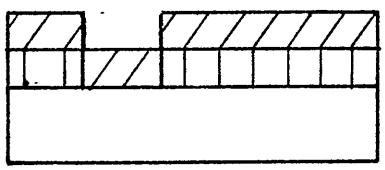

4. Evaporate titanium.

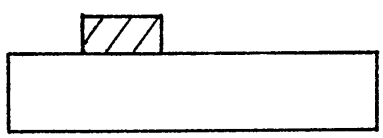

5. Lift-off unwanted metal.

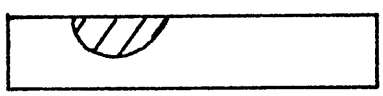

6. Diffuse at high temperature.

FIG.4.1. Fabrication stages for a titanium in-diffused waveguide.

After the waveguide had been fabricated by the particular process, the production of an active device required an additional metal evaporation process to define the electrode pattern. During the course of this work the usual lift-off procedure had to be modified for this additional stage to allow the evaporation and patterning of thick metal films. The modification will be described in greater detail in sect. 4.4.

4.1.1. MASK FORMATION.

The optical quality of the finished waveguide is strongly dependent upon the quality of the original master pattern, and the subsequent transfer of the pattern from the chromium mask onto the sample. The waveguide and electrode patterns were first cut from a sheet of 'Rubylith' stripping film on a flat cutting table. The resulting pattern was then stripped of the opaque film and evenly illuminated from the rear. A 20x. reduction was made by projecting the pattern onto a photographic plate through a lens capable of very high resolution. The plate was subsequently developed and a further reduction of x10 was carried out by projecting the image of the plate through a Micro Tropel lens onto a pre-coated Balzers 2x2" chrome mask. With this technique the minimum line width obtainable was on the order of 1.25μm over a distance of 18mm. In general, the waveguide widths required were between 4 and 10μm over a distance of approximately 10mm, thus avoiding the need for more sophisticated methods such as electron-beam lithography [10,16].

4.1.2. SUBSTRATE PREPARATION.

The lithium niobate substrates used were of optical

quality, manufactured by Barr & Stroud Ltd.. These substrates were nominally 1mm thick and had dimensions of 45x47mm with one of the large faces polished to an optical finish. The substrates were then cut using a diamond saw to provide samples approximately 10x15mm in size. X-, Y- and Z- cut substrates were all used in the course of making the standing wave modulator to exploit the advantages offered by the different fabrication methods i.e. the Ti:in-diffusion and proton-exchange technologies.

4.1.3. SUBSTRATE CLEANING PROCEDURE.

Regardless of the specific fabrication technique employed, the subsequent success in forming waveguides was primarily determined by the care taken in preparing the sample prior to the various photolithographic processes. The physical size of the waveguides dictated that the surface of the substrates had to be both dirt and grease free. The presence of any dirt or dust particles could form breaks in the titanium stripes or irregularities in the diffused waveguide. Some time was therefore spent in developing a cleaning procedure that was both efficient in time and which produced a surface free from large dust paticles (i.e. >1μm) to which the photoresist and titanium would adhere. The problem of dust particle adhesion was further compounded by the ferro-electric nature of the lithium niobate and the large static charges that may build up [17].

By adhering to the following cleaning procedure the proportion of samples which had acceptable waveguides could approach 80%. The procedure developed is described in detail below:

1. All beakers and implements to be used were thoroughly cleaned with soapy water in an ultrasonic bath. They were then rinsed in de-ionised water and then left in a methanol bath for 10 minutes.

2. The lithium niobate substrates were hand scrubbed in soapy water and then placed in a clean beaker of Decon diluted with de-ionised water to give a 5% solution and left in the ultrasonic bath for 10 minutes.

3. They were then rinsed again with de-ionised water.

4. This was followed by placing the samples in a methanol bath and leaving them in an ultrasonic bath for 5 minutes.

5. The methanol was replaced by trichloroethylene and the sample was ultrasonically agitated for 5 minutes.

6. The trichloroethylene was replaced by methanol with 5 minutes of ultrasonic agitation.

7. The methanol was replaced by acetone with a further 10 minutes of ultrasonic agitation.

8. The final rinse was in a methanol bath for a period of 20 minutes, with frequent changes of solvent and occasional ultrasonic agitation.

9. The samples were then stored in methanol until they were about to be coated with photoresist.

10. Before applying the photoresist the samples were quickly dried by spinning on a vacuum chuck and leaving in a de-humidifying cupboard for 10 minutes.

4.1.4. PHOTORESIST PATTERNING.

The photoresist was applied to the sample surface through a syringe with a 0.2μm filter. The photoresist used was Shipley AZ1350J positive resist. However, AZ1450J was also employed for the fabrication of the standing wave modulator electrode pattern where a thick even coat of resist was necessary. A few drops of resist were applied to the surface of the sample mounted on a vacuum chuck semiconductor wafer spinner. The speed and time of rotation governed the eventual resist thickness and in general the spin time was set at 20 seconds with a spin speed 3200 r.p.m. which usually gave a thickness of 1.8μm for AZ1350J. The samples were then placed in a pre-heated oven set at a temperature of between 80 and 85°C for approximately 30 minutes to evaporate the remaining solvent present in the photoresist.

During the baking period the chromium mask with the waveguide pattern was thoroughly cleaned. This procedure followed the same steps as those for cleaning the lithium niobate substrates. The only major change was that after the final rinse the mask was blow-dried with filtered dry nitrogen and placed in a dust tight container. Once the photoresist baking period had elapsed the pattern was formed on the sample by simple contact printing. The photoresist coated surface of the substrate was placed in close contact with the chromium mask and exposed to an ultra-violet lamp for several seconds. The exact exposure time was found to be critical and therefore before each production run, a test sample had to be used to find the optimum exposure time. These times were typically from 20 to 30seconds and were dependent upon the aging characteristics of the ultra-violet source and the

initial thickness of the photoresist film.

The exposed photoresist was then developed in Shipley AZ developer diluted in a 1:1 volumetric ratio with de-ionised water. The development time was nominally 70 seconds but this was affected by the room temperature and the thickness of the resist film. To stop development, the sample was placed in a stream of flowing water to wash away all remaining traces of developer. The sample was then blow-dried with filtered nitrogen and examined underneath an optical microscope, to check the integrity of the waveguide patterns. If the pattern possessed no flaws and was intact it was then ready for titanium deposition.

4.1.5. TITANIUM DEPOSITION.

The initial thickness of titanium deposited upon the sample had a marked effect on the final waveguiding characteristics of the waveguide [18]. Therefore, accurate control of the film thickness and subsequent diffusion processess had to be achieved in order to obtain reproducible results. In some situations, variations in the metal thickness of the order of ~10Å [17] could result in a waveguide supporting several modes, where only a monomode device was envisaged. Usually the titanium thickness was between 200 and 300Å to produce monomode waveguides at 0.633μm.

An electron beam evaporation source was used to deposit high purity titanium (99.97%) onto the sample mounted on a glass slide for ease of handling. The evaporation was performed at a base pressure of less than 8.10^{-6} Torr. As the titanium was being evaporated the thickness of the deposited layer was continuously monitored by a

crystal film thickness monitor. On completion of the deposition, a further measurement of the film thickness was made using a Talystep which provided an accuracy of ~5Å. This measurement was performed on the glass slide that was used to support the substrate inside the evaporation chamber. Generally, the values obtained by the two different methods agreed to within 10% for film thicknesses in the range 250 to 300Å which was necessary to form single mode waveguides.

4.1.6. METAL LIFT-OFF.

On removal from the vacuum deposition chamber, the lift-off technique was performed on the sample, leaving the required titanium stripe waveguide pattern. The sample was placed in a bath of acetone and gently agitated. The acetone dissolved the remaining exposed photoresist and therefore removed any titanium that had been evaporated on top of it, leaving the titanium that adhered to the surface of the sample. Care had to be exercised to ensure that the solvent covered the entire surface of the sample completely. If due regard was not paid to this aspect of the procedure, then the unwanted titanium would be redeposited onto the surface as the solvent evaporated and could be extremely difficult to remove thereafter. As the resist dissolved, the titanium evaporated on top of it flaked away. Depending upon the intricacies of the pattern, a soft camel hair brush was sometimes used to gently swab the unwanted titanium away between adjacent stripes if the separation was small (<2μm). As a final preparation prior to diffusion, the sample was given a brief rinse in methanol and then blow-dried.

4.1.7. TITANIUM IN-DIFFUSION.

The increase in the localised refractive index necessary to produce optical waveguiding was achieved by diffusing the thin titanium stripes forming the waveguide pattern into the substrate at an elevated temperature [8]. In the course of this work the diffusion conditions were standardised to a diffusion temperature of about 1025°C for a period of nine hours. The nine hour diffusion time was preceded by a one hour heat up time to the required temperature and a natural cool down time of some twelve hours on completion of the prescribed diffusion period.

Several methods were adopted during the diffusion process with the objective of eliminating the process of out-diffusion which can give rise to a surface guiding region for light polarised parallel to the c-axis [12]. The diffusion of titanium into $LiNbO_3$ is a complicated process involving the formation of various compounds and phases at different temperatures. Several different mechanisms have been reported to be involved in the diffusion [19] process, but the most systematic study to date has been carried out by Armenise et al. [19,20,21], who have analysed the formation of the different phases present by a variety of micro-analytical techniques (RBS, SIMS, Electron micro-probe) to show that four distinct stages occur during the diffusion process. They have also found that the formation of Li-Ti-O compounds suggested elsewhere [22,23] is unlikely. There is, of course, some overlap between the manifestation of these distinct stages. The different phases will now be described.

The deposited titanium initially undergoes an oxidation

process by reacting with the oxygen present in the atmosphere and available from the $LiNbO_3$ during the course of warm up. This process is relatively rapid at temperatures up to 500°C. At the same time Li_2O occurs which leads to the formation of a Nb rich region directly underneath the titanium oxide layer. After the complete oxidation of the titanium film has occurred, growth of the $LiNb_3O_8$ compound takes place at temperatures greater than 600°C due to the rich Nb layer. The extent of formation of this phase is dependent upon the ambient temperature and the dwell time of the sample at the ambient temperature. It does not grow in the presence of water vapour. This phase continues to grow and subsequently decomposes at temperatures greater than 900°C when the $(Ti_{1-x}Nb_x)O_2$ compound forms by consuming the TiO_2 layer at temperatures above 950°C.

Once the titanium oxide layer has disappeared, the titanium drive-in period commences with the exchange of titanium for lithium in the bulk of the substrate. The growth of $LiNb_3O_8$ at the surface only occurs in a dry atmosphere. It is eventually replaced by the regrowth of $LiNbO_3$ irrespective of the presence of titanium. The mobile Li_2O compound quickly diffuses through this layer and produces a guiding layer below the surface [12].

In order to reduce the effect of this slab-like waveguiding region arising from the out-diffusion of lithium, several methods have been proposed whereby the out-diffusion of lithium atoms is minimised. The methods employed vary greatly in complexity ranging from a simple closed system [24] to diffusion in an atmosphere of a wet inert gas [25,26]. The easiest method reported [24] involves diffusion in a closed atmosphere rich in Li_2O produced by the presence of some congruent $LiNbO_3$ powder.

A partial pressure of Li_2O is produced inhibiting the out-diffusion of lithium from the surface of the sample. Although according to Armenise et al. [20] this does not inhibit the growth of the $LiNb_3O_8$ layer but it does inhibit the out-diffusion of Li_2O. This type of quasi-closed system approach was adopted for the formation of waveguides in the present work, because it was the simplest and produced the most consistent results.

Other arguments suggest that the diffusion should be carried out in an atmosphere of wet argon to minimise the oxidation effects at the surface [25]. One possible method that has received little attention for $LiNbO_3$ waveguide formation is the deposition of an inert layer onto the surface, forming a cap, which has proved popular for use in the semiconductor industry - especially in the manufacture of GaAs M.I.C.'s. Of course, the capping layer would have to exhibit passivity and impermeability to Li_2O for temperatures upto 1000°C, and be easily removed without affecting the substrate surface.

On completion of the prescribed diffusion period, the sample was removed from the furnace and given a thorough clean in methanol agitated in an ultrasonic bath. At this stage any particles of $LiNbO_3$ powder loosely adhering to the surface would be removed.

4.1.8. SUBSTRATE END-FACE POLISHING.

The optical modes of the waveguide were excited by coupling light by the 'end-fire' technique [18]. This method was employed in preference to fibre coupling methods as it provided more freedom in the selection of

waveguides and modes excited. For both methods to exhibit the optimum coupling of power into the waveguide, the endfaces of the sample had to be polished to a very high degree. A brief explanation of the polishing method will be given for completeness.

It was only in very rare instances that the mask pattern ran right to the end of the sample. In all other cases there were usually two or three millimetres between the end of the waveguide and the edge of the substrate, as the mask pattern was usually only 10mm long. The excess material at either end was cut away by a diamond rotary saw. The sample was then mounted on a quartz holder using melted Shellac. Care had to be taken to ensure that the bottom of the quartz holder was parallel with the edge of the substrate.

The sample was then ready for the first stage of the polishing preparation. The edge was roughened down to remove the cutting striations by using a grit of ~12μm particle size. The sample was cleaned and then a sequence of diamond pastes becoming progressively finer were used on a solder plate to semi-polish the surface. The final polish consisted of an abrasive mechano-chemical etch for some twelve hours using Syton W15 until the end appeared mirror-like underneath an optical microscope.

The substrate was reversed in the quartz holder and the whole process repeated on the other edge. Throughout the entireprocedure, a certain degree of perpendicularity of the end with respect to the direction of the waveguide was maintained to within two degrees. After removal from the quartz holder, the samples were thoroughly cleaned in methanol and trichloroethylene to remove any

remaining vestiges of wax.

4.2. FABRICATION OF PROTON-EXCHANGED WAVEGUIDES.

For the fabrication of proton-exchange waveguides [15], the substrates underwent the same cleaning preparation as used for making titanium in-diffused waveguides. However, after the final rinse associated with the cleaning procedure, a thin film of aluminium (99.97% pure, approximately 1000Å thick) was immediately evaporated onto the surface. In this case the waveguide pattern was formed by opening up diffusion apertures in the aluminium by etching through a photo-resist mask replicating the desired waveguide pattern. The aluminium etchant used was Phosphoric acid, Nitric acid and water in the volumetric proportions 85%:5%:10%. The process is shown in Fig.4.2.

Once the desired pattern had been defined by etching the aluminium film, the sample was then placed in a small P.T.F.E. holder which was completely immersed in a 250ml stainless steel beaker containing sufficient molten Benzoic acid to cover the sample. The temperature of the oil and of the Benzoic acid was stabilised by placing it in a thermostatically controlled oil bath capable of providing accurate control to within 0.5°C. The temperature was also externally measured with a thermo-couple. The time of immersion varied from several minutes to a few hours, depending upon the optical characteristics required (see Chapter 5). The temperature range was again set by the desired optical characteristics but was always between the melting and boiling points of the acid i.e. between 180°C and 220°C.

On completion of the exchange period, the samples were carefully removed from the acid and allowed to cool

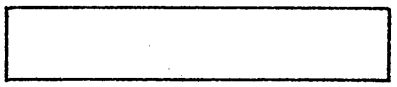

1. Clean substrate.

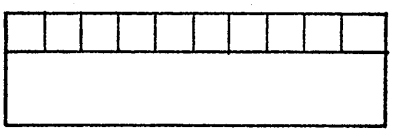

2. Evaporate aluminium.

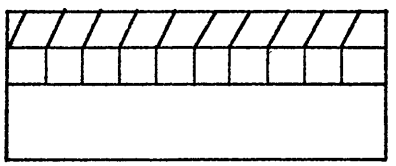

3. Coat with phototresist.

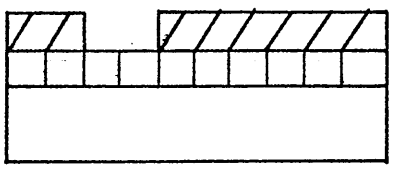

4. Expose and develop.

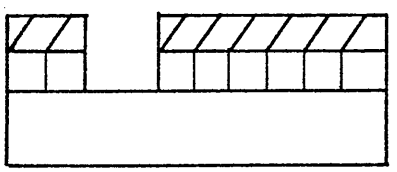

5. Etch aluminium.

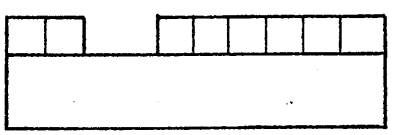

6. Remove resist and proton exchange.

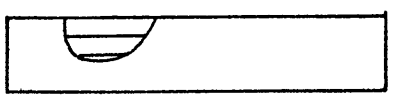

7. Remove excess aluminium.

FIG.4.2. Fabrication stages for a proton-exchange waveguide.

naturally. The excess acid that crystallised on the substrate was dissolved away by ultrasonic agitation in a methanol bath. After cleaning, the samples were end-polished following the description given in 4.2.8. Depending on the proposed application of the waveguide the remaining aluminium was left intact or etched completely off. For active devices the aluminium was usually left intact on the surface to provide the basis of the electrode fabrication process.

Proton-exchange in a dilute melt involved the addition of some lithium benzoate to the melt. The proportion of lithium benzoate was usually between 0.5 and 2% molecular weight of the melt. The lithium benzoate was added to the acid after it had become molten and was then thoroughly mixed in. Annealing was performed after the exchange process had been completed in either the concentrated melt or the diluted melt. The annealing was carried out either in a wet or a dry atmosphere by passing a gas over the sample situated in a large bore silica tube surrounded by a heating element. The wet atmosphere was produced by passing the gas through a flask of water at a temperature of between 60 and 70°C.

4.3. PATTERNING OF THICK METAL FILMS BY LIFT-OFF.

The final part of this description of the experimental procedure is dedicated to the formation of the standing wave electrode pattern on the substrate. After the waveguides had been fabricated using one of the two technologies described earlier the samples were again thoroughly cleaned.

From the theory presented in Chapter 3 it is clear that the performance of the modulator is dependent upon the

thickness of the aluminium that forms the electrode pattern. This dependence implies a requirement that the metal film thickness has to be at least 1μm thick. As the electrodes have also to be accurately positioned with respect to the waveguide and possess square edges, an etching technique was deemed unsuitable as undercutting of the metal structure would occur, greatly affecting the verticality of the edges and, therefore, the current distribution in the coplanar waveguide. Therefore the lift-off method was favoured, but the standard process suffered from the drawback that only film thicknesses of up to ~2000Å could give consistent results.

The lift-off procedure for patterning metal thicknesses up to a few hundred nanometres worked consistently because the ratio of photoresisit height to the metal thickness was large, typically in the range from 10 to 100 times. To use lift-off for thicker metal layers, the edge verticality of the photoresist becomes important. If the edges did not exhibit verticality but sloped outwards then the metal would also adhere to this portion of photoresist, inhibiting penetration of the acetone into metal coated photoresist areas Fig.4.3. To alleviate this problem a method was investigated which produced sufficient undercutting of the photoresist to leave a masked area.

Descriptions of the method reported in [27,28], indicated that the metal thickness in the lift-off process could be increased by an order of magnitude by soaking the photoresist in chlorobenzene from 1 to 20 minutes either prior to or after exposure. The modification was investigated to obtain the ideal fabrication conditions for delineating the electrode

1 μm markers

Fig 4.3. S.E.M. photograph of untreated photoresist

pattern in ~1.8μm of aluminium.

The chlorobenzene immersion process chemically modified the top few 100nm of the photoresist so that it exhibited differential developing characteristics in comparison with the bulk photoresist. In order to maximise the difference in the development characteristics, a series of experiments were performed to ascertain the ideal conditions for lift-off of 1.8μm of aluminium. The soaking process could be performed either before or after exposure and both methods were therefore investigated.

In the treatment prior to exposure, AZ1450J photoresist was spun on the substrate at a speed of 1800 r.p.m. for 20 seconds. to give a resist layer of ~2.8μm thick. The sample was then baked at 75°C for a period of 15 minutes. On completion of this bake period, the sample was fully immersed in a beaker of chlorobenzene at room temperature in a fume cupboard. The soaking times ranged from 5 to 30 minutes. After the soaking period the sample was then rebaked for a further 15 minutes after which the usual exposure process was performed. Some increase in the exposure was found to be necessary to compensate for the modified photoresist characteristics; typically a 20% increase. The development time was fixed at the standard 70 seconds. for AZ developer diluted in a 1:1 volumetric ratio with de-ionised water. The sample was finally rinsed in running de-ionised water to stop development.

The sample then had a film of aluminium evaporated upon it and the lift-off was carried out by covering the sample completely with acetone and leaving it immersed for 12 hours. This was usually sufficient to dissolve the photoresist but limited use of an ultrasonic bath removed stubborn areas.

The degree of undercutting was found to be dependent on the soak time and the optimum time was found to be 15 minutes.

For the second treatment process, the photoresist was baked for 15 minutes at 75°C, but on completion of this baking period it was exposed immediately. After exposure the sample was soaked in chlorobenzene for between 5 and 20 minutes and baked for a further 15 minutes and then developed. A substantial increase in the development time was found to be necessary; up to 4 minutes. With the post-exposure soak Fig.4.4 the degree of undercutting was found not to be as marked as for the pre-exposure soak case as is shown in Fig.4.5.

Once this process had been perfected it was applied to the fabrication of the electrode pattern over an optical waveguide. However, due to the initial thickness of the photoresist required for this process, it was impossible to obtain sufficient alignment between the electrode mask pattern and the optical waveguide using the mask aligner. The problem was solved by initially using a thin layer of resist (~1μm) and performing lift-off with a very thin layer of aluminium <200Å to delineate the electrode pattern. The thin layer then acted as a template for alignment of the mask pattern with the thick layer of photoresist and gave sufficient reflectivity contrast to enable accurate alignment.

The extra stage required is shown in Fig.4.6 and a photograph of the final electrode structure fabricated is shown in Fig.4.7.

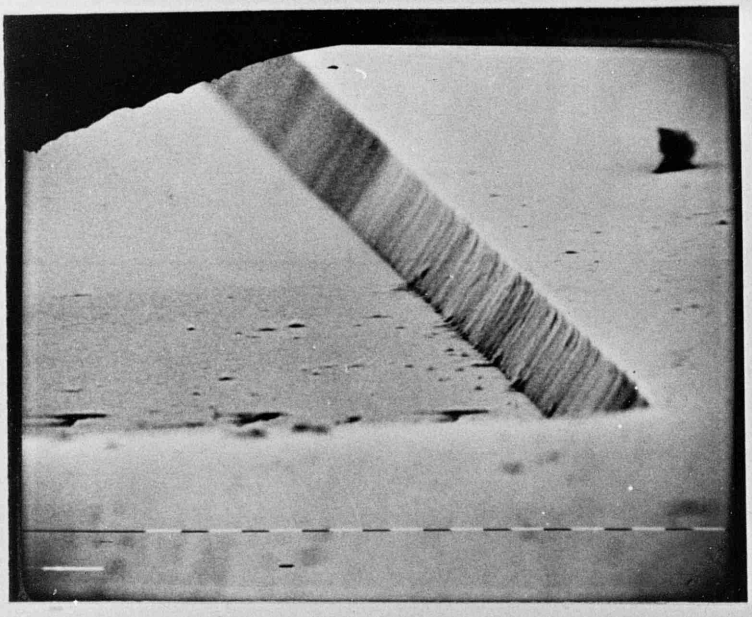

1 μm markers

Fig 4.4 S.E.M. photograph of post-exposure soaked photoresist in chlorobenzene

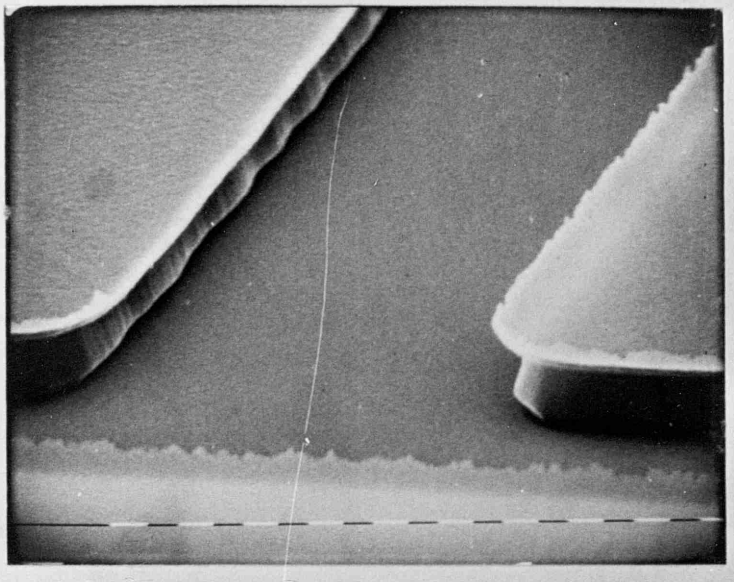

1 μm markers

Fig 4.5 S.E.M. photograph of pre-exposure soaked photoresist in chlorobenzene

1. Form optical waveguide.

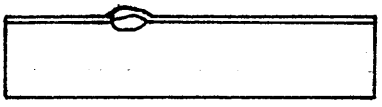

2. Evaporate thin film of aluminium.

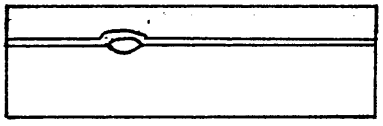

3. Coat with thick layer of photoresist and soak in chlorobenzene.

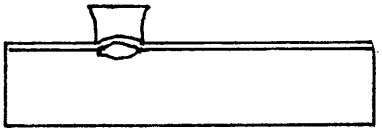

4. Expose and develop.

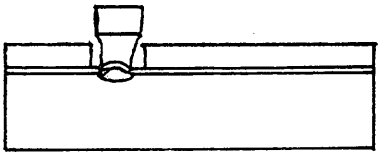

5. Evaporate thick film of aluminium and perform lift-off.

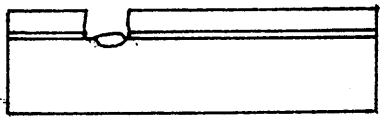

6. Brief etch in aluminium etch to remove initial thin film in unwanted areas.

FIG.4.6. Alignment technique to define electrode position.

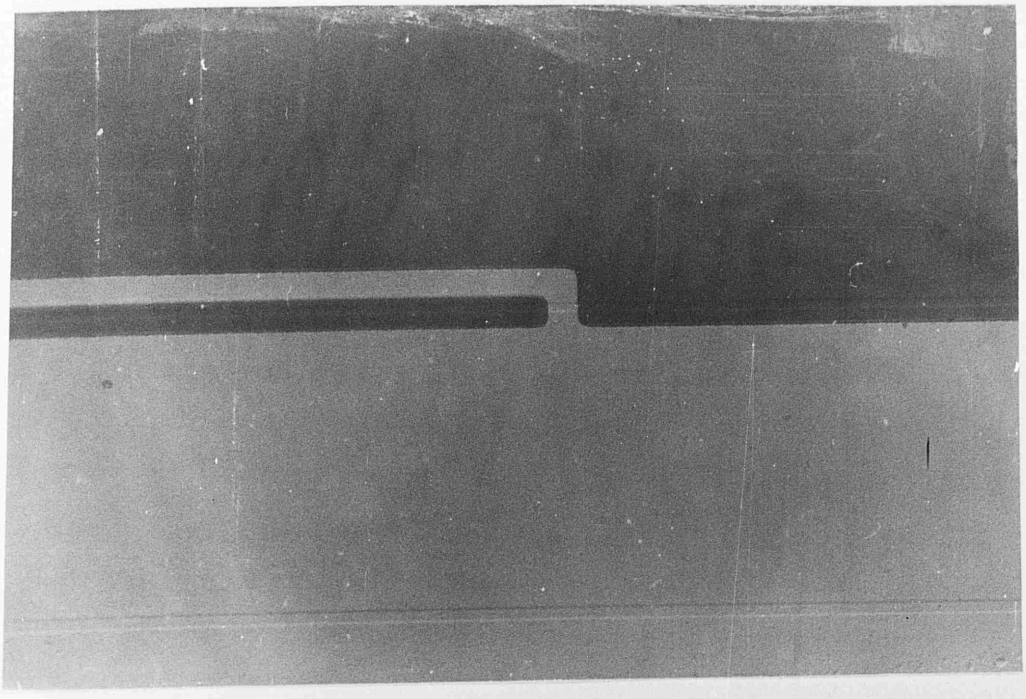

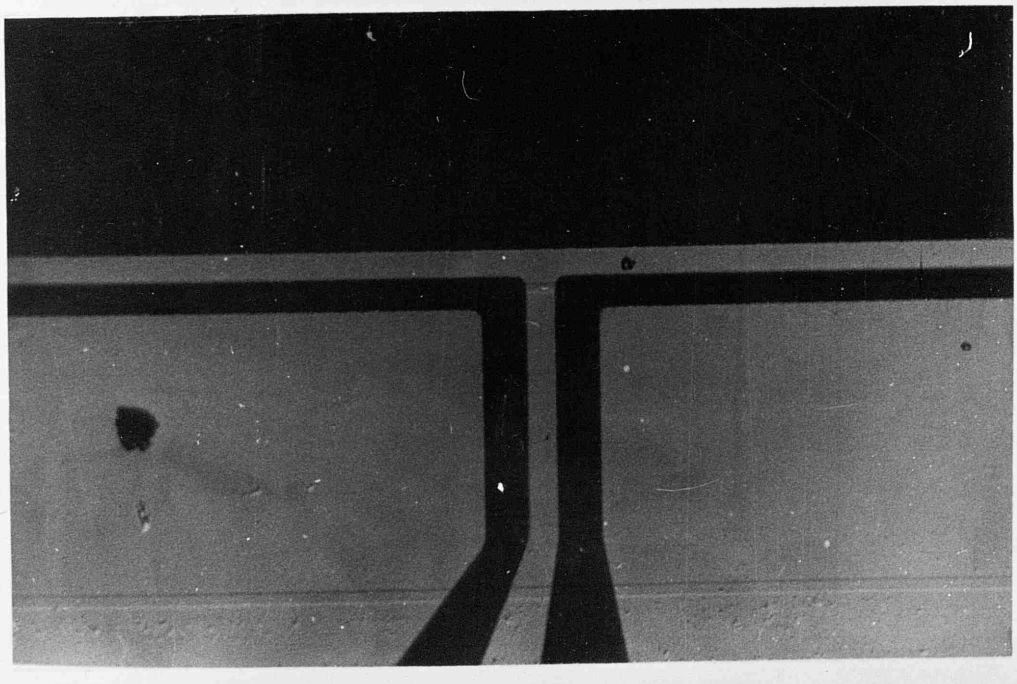

FIG.4.7. Photograph of aluminium electrode pattern.

4.4. WAVEGUIDE FORMATION USING GaAs/GaAlAs TECHNOLOGY.

The feasibility of forming optical waveguides in semiconductor materials takes the concept of monolithic integrated optics one step closer to realisation [29]. This has arisen as semiconductors already play an important part as the base material for the sources and detectors used in communications systems - in contrast to $LiNbO_3$ where it is difficult or impossible to form such devices with any kind of useful performance. To benefit from the low material dispersion loss of silica fibres these sources must operate between 1.3μm and 1.55μm. The variation in operating wavelength is achieved easily by lattice matched heterostructures formed by quaternary materials GaInAsP where the operating wavelength may be continuously varied between .85μm and 1.55μm, depending on the proportions of the constituent elements. Most device fabrication has initially been done on GaAs, but InP based devices are gradually being reported due to the requirement of operation at wavelengths of 1.3μm.

Optical waveguides and other components for integrated optical systems can be formed in these materials: for example modulators [30,31], directional couplers [32-36] and bistable devices [37]. Although,compared with $LiNbO_3$, GaAs has a much smaller electro-optic coefficient. However it is in the field of phase matched travelling wave devices that the true strength of GaAs lies, in terms of the power bandwidth requirements. The physical and chemical properties of GaAS are described in the comprehensive review article by Blakemore [38]. The formation of both optical and electronic devices using GaAs has given rise to the integration of several devices on one chip [39]. However the different electrical and optical characteristics required by the

range of active devices have reduced the initial optimism about the possibility of full scale optoelectronic integration.

Several different techniques have been established for the formation of optical waveguides in III-V materials. Light confinement was first observed by Yariv et al. [40] in the carrier depleted region of a p-n junction formed by diffusing a p-type dopant into GaAs. Due to the band gap of GaAs low absorption loss light guiding can only be achieved in the infra-red i.e. at wavelengths greater than about 0.9μm. Other guiding configurations may be formed by closely lattice-matched epitaxial layers of AlGaAs in which the refractive indices depend on the aluminium/gallium ratio present [41]. A difference in carrier concentration due to dopant diffusion or proton-implantation between regions of the same material may also lead to a sufficient index difference to produce confinement [42].

Lateral confinement is then achieved through etching rib waveguides in the top epilayer which can be grown by a variety of methods e.g. Molecular Beam Epitaxy [43], Metal Organic Chemical Vapour Deposition [44] and Liquid Phase Epitaxy [45]. Work on such guides has been reported by a number of researchers [30-37]. Etching may be performed by a variety of techniques ranging from a purely wet chemical method [46] to a purely ion bombardment abrasive or sputtering method [47]. Etching has gained acceptance over diffusion because the losses associated with etched waveguides are lower than for diffused ones.

Between these extremes in etching lie several other processes incorporating the characteristics of chemical

and abrasive etching to various degrees. These range from the most chemically orientated through to the most abrasive; plasma etching [48,49], reactive ion etching [50], reactive ion beam etching [48], ion etching [48]. These different methods are described in greater detail elsewhere along with their possible future application in Integrated Optics [51].

The processing of these materials to form acceptable waveguides requires that the side walls are of a very smooth quality. Any variation in the wall profile over a distance comparable with the guide wavelength would lead to excitation of other modes. To be able to analyse these waveguides accurately it is also desirable that the walls are vertical. With a view to optimising these conditions in a single process, only dry etching of the guide structures was investigated.

The preparation of the samples prior to coating with photoresist was nearly identical to that used for cleaning $LiNbO_3$, the only difference being a reduction in the time that the samples were in the ultrasonic baths. It was observed that GaAs cleaved very easily along the [110] plane when cleaned ultrasonically. This sometimes led to the complete disintegration of the sample. Once the sample had been cleaned and coated with photoresist it was then exposed and developed. With dry etching the resist served as the masking material. A brief description of a typical dry etching process will be given here for completeness.

Ion milling is the process whereby charged ions are extracted from a low pressure plasma and accelerated towards the target. The acceleration is produced by a grid plate at a negative potential with respect to the

ions and as these ions pass through the grid a hot wire filament produces electrons to give a neutral beam.

As the ions impinge on the sample surface their kinetic energy is transferred to the top atoms and dislodges them from the surface. This process gradually etches away the exposed surface at a rate determined by the incident ion energy and their angle of incidence at the surface. The masking material also undergoes the same process but it is desirable that the etch rate is several times slower. In practice it is found that a layer of photoresist provides sufficient masking. The relative difference in etch rates is related to the manner in which the atoms bond within the material.

Once the samples had been patterned they were etched in an Oxford Applied Research ion beam machine. The system was pumped down to a base pressure of 2.10^{-6} Torr and then an easily ionised gas (in this case Argon) was leaked into the chamber until the pressure reached 5.10^{-3} Torr. The gas was then ionised in the plasma chamber and the ion beam extracted. The energy of the beam was dependent upon the accelerating potential and this was usually of the order of between 500eV and 1500eV depending on the etch rates and depths required.

To ensure even etching over the entire surface of the sample, it was placed on a water-cooled rotating stage. The angle of the surface with respect to the incident ions could also be altered to minimise the effects of trenching and redeposition [52] to produce smooth vertical walls. Fig.4.8 illustrates the edge definition that may be achieved with ion milling using photoresist that has been baked at $90^{o}C$ for 25 minutes for the mask.

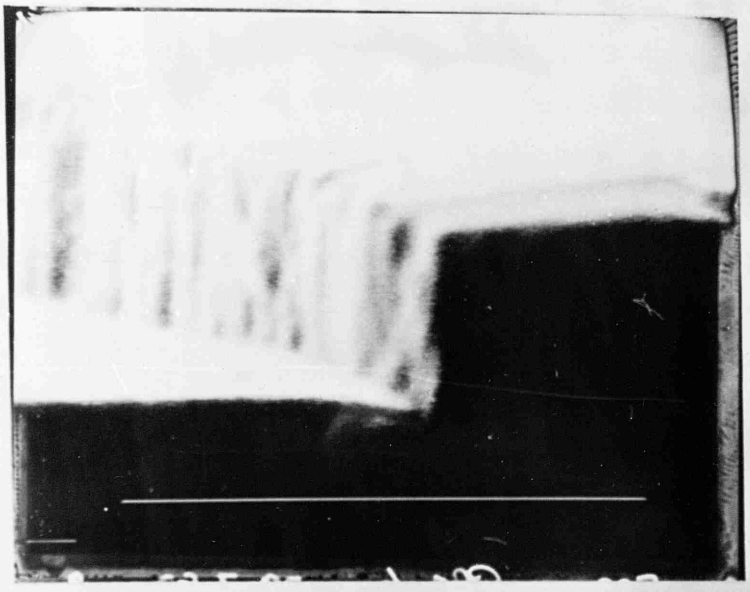

1μm markers.

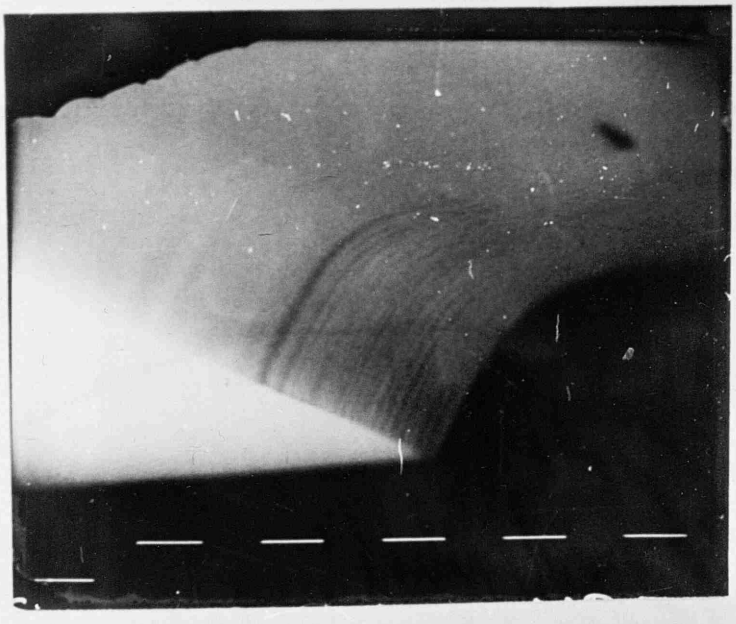

(b)

FIG.4.8. Edge definition of ion milled (a) groove using photoresist for the mask (b).

After etching the sample was removed from the vacuum chamber and cleaned thoroughly in acetone to remove all traces of the photoresist. The sample was prepared for end-fire coupling by scribing the ends with a diamond scribe and breaking off the unwanted section on a sharp edge.

4.5. SUMMARY.

This chapter has outlined the steps involved in preparing substrates for the fabrication of optical waveguides in either $LiNbO_3$ or GaAs. To ensure the successful formation of waveguides, time had to be spent in developing a cleaning procedure. A brief description of the various technologies available for forming optical waveguides has also been given. A method reported for performing lift-off on thick metal films was investigated and successfully applied to making an electrode structure 1.8μm thick. The method proved to be simple and gave consistent results after the optimum treatment time in the chlorobenzene had been found.

References Chapter 4.

[1] A.Rauber.
Chemistry and Physics of Lithium Niobate.
Current Topics in Materials Science.
Vol.1, Chap.7,
F.Kaldis Rd.,1978

[2] A.A.Ballman.
Growth of piezoelectric and ferroelectric materials by the Czochralski technique.
J. Am. Cera. Soc.,Vol.48(3),1965,pp.113-115.

[3] G.E.Peterson,A.A.Ballman,P.V.Lenzo and P.M.Bridenbaugh.
Electro-optic properties of $LiNbO_3$.
Appl. Phys. Letts.,Vol.5(3),1964,pp.62-65.

[4] G.D.Boyd,R.C.Miller,K.Nassau,W.L.Bond and A.Savage.
$LiNbO_3$:an efficient phase matchable nonlinear optical material.
Appl. Phys. Letts.,Vol.5(3),1964,pp.234-236.

[5] A.Savage.
Pyroelectricity and spontaneous polarisation in $LiNbO_3$.
J. Appl. Phys.,Vol.37(8),1966,pp.3071-3072.

[6] A.M.Glass,D. von der Linde and T.J.Negram.
High voltage bulk photovoltaic effect and the photorefractive process in $LiNbO_3$.
Appl. Phys. Letts.,Vol.25(4),1974,pp.233-235.

[7] D.R.Bosomworth.
Far infrared optical properties of $LiNbO_3$.
Appl. Phys. Letts.,Vol.9(9),1966,pp.330-331.

[8] R.V.Scmidt and I.P.Kaminow.
Metal diffused optical waveguides in $LiNbO_3$.
Appl. Phys. Letts.,Vol.25(8),1974,pp.458-461.

[9] W.K.Burns,P.H.Klein,E.J.West and L.E.Plew.
Ti diffusion in Ti/$LiNbO_3$ planar and channel optical waveguides.
J. Appl. Phys.,Vol.50(10),1979,pp.6175-6182.

[10] L.W.Stulz.
Titanium indiffused optical waveguide fabrication.
Appl. Opts.,Vol.18(12),1979,pp.2041-2044.

[11] R.C.Alferness,R.V.Schmidt and E.H.Turner.
Characteristics of Ti-diffused lithium niobate optical directional couplers.
Appl. Opts.,Vol.18(23),1979,pp.4012-4016.

[12] J.R.Carruthers,I.P.Kaminow and L.W.Stulz.
Diffusion kinetics and optical waveguiding properties of outdiffused layers in lithium niobate and lithium titanate.
Appl. Opts.,Vol.13(10),1984,pp.2333-2342.

[13] I.P.Kaminow and J.R.Carruthers.
Optical waveguiding layers in $LiNbO_3$ and $LiTaO_3$.
Appl. Phys. Letts.,Vol.22(7),1973,pp.326-328.

[14] J.M.Naden and B.L.Weiss.
Ion implanted optical waveguides in lithium niobate.
Radio and Elect. Eng.,Vol.54,1984,pp.227-230.

[15] J.L.Jackel,C.E.Rice and J.J.Veselka.
Proton exchange for high index waveguides in $LiNbO_3$.
Appl. Phys. Letts.,Vol.41(7),1982,pp.607-608.

[16] J.E.Goell.
Electron-Resist Fabrication of Bends and Couplers for Integrated Optical Circuits.
Appl. Opts.,Vol.12(4),1973,pp.729-736.

[17] A.D.McLachlan.
Theoretical and experimental investigations of titanium diffused lithium niobate waveguides.
Ph.D. Thesis.,Glasgow University,1981.

[18] B.Bjortorp.
Active and passive devices in lithium niobate by single and double diffusion.
Ph.D. Thesis.,Glasgow University,1983.

[19] M.N.Armenise,C.Canali,M. De Sario,A.Carnera, P.Mazzoldi and G Celotti.
Ti compound formation during Ti diffusion in $LiNbO_3$.
I.E.E.E. Trans. Components, Hybrids & Manufacturing Techn.
Vol.CHNT-5(2).,1982,pp.212-216.

[20] M.N.Armenise,C.Canali,M. De Sario,A.Carnera, P.Mazzoldi and G Celotti.
Characteristics of TiO_2, $LiNb_3O_8$ and $(Ti_{0.65}Nb_{0.35})O_2$ compound growth observed during Ti:$LiNbO_3$ optical waveguide fabrication.
J. Appl. Phys.,Vol.54(11),1983,pp.6223-6231.

[21] M.N.Armenise,C.Canali,M. De Sario,A.Carnera, P.Mazzoldi and G Celotti.
Characterisation of $(Ti_{0.65}Nb_{0.35})O_2$ compounds as a source for Ti diffusion during Ti:$LiNbO_3$ optical waveguide formation.
J. Appl. Phys.,Vol.54(1),1983,pp.62-70.

[22] W.K.Burns,P.H.Klein,E.J.West and L.E.Plew.
Ti diffusion in Ti/$LiNbO_3$ planar and channel optical waveguides.
J. Appl. Phys.,Vol.50(10),1979,pp.6175-6182.

[23] R.L.Holman,P.J.Crossman and J.A.Anderson.
Practical aspects of efficient tapered gap prism coupling to diffused $LiNbO_3$ waveguides.
Ferroelctrics,Vol.27(1-4),1980,pp.77-81.

[24] R.J.Esdaile.
Closed tube control of out-diffusion during fabrication of optical waveguides in $LiNbO_3$.
Appl. Phys. Letts.,Vol.33(8),1978,pp.733-734.

[25] J.L.Jackel,V.Ramaswamy and S.P.Lyman.
Elimination of out-diffused surface guiding in titanium diffused $LiNbO_3$.
Appl. Phys. Letts.,Vol.38(7),1981,pp.509-511.

[26] Ber-uei. Chen and A.C.Pastor.
Elimination of Li_2O out-diffusion waveguide in $LiNbO_3$ and $LiTaO_3$.
Appl. Phys. Letts.,Vol.30(11),1977,pp.570-571.

[27] M.Hatzakis,B.J.Canavello and J.M.Shaw.
Single step optical lift-off process.
I.B.M. J. Res. Develop.,Vol.24(4),1980,
pp.452-460.

[28] Pao-Lo Liu.
$LiNbO_3$ waveguide modulator with 1.2um thick electrodes fabricated by lift-off technique.
I.E.E.E. J. Quant. Electrs.,Vol.QE18(10),1982,
pp.1780-1782.

[29] S.E.Miller.
Integrated optics: An introduction.
B.S.T.J.,Vol.48(7),1969,pp.2059-2069.

[30] F.K.Reinhart and R.A.Logan.
Monolithically integrated AlGaAs double heterostructure optical components.
Appl. Phys. Letts.,Vol.25(10),1974,pp.622-624.

[31] F.K.Reinhart and B.I.Miller.
Efficient GaAs-$Al_xGa_{1-x}As$ double hetrostructure light modulators.
Appl. Phys. Letts.,Vol.20(1),1972,pp.36-38.

[32] A.Carenco and L.Menigaux.
GaAs homojunction rib waveguide directional coupler switch.
J. Appl. Phys.,Vol.52(3),1980,pp.1325-1327.

[33] J.P.Donnelly,N.L.De Meo and G.A.Ferrante.
Three-Guide optical couplers in GaAs.
I.E.E.E. J. Light. Techn.,Vol.LT1(2),1983,
pp.417-423.

[34] J.C.Campbell,F.A.Blum,D.W.Shaw and K.L.Lawley.
GaAs electro-optic directional coupler switch.
Appl. Phys. Letts.,Vol.27(4),1975,pp.202-204.

[35] K.Tada and H.Yanagawa.
New coupled waveguide optical modulators with
Schottky contacts.
J. Apll. Phys.,Vol.49(11),1978,pp.5404-5406.

[36] A.R.Reisinger,D.W.Bellavance and K.L.Lawley.
GaAlAs Schottky directional coupler switch.
Appl. Phys. Letts.,Vol.31(12),1977,pp.836-838.

[37] A.Carenco and L.Menigaux.
Optical bistability using a directional coupler
and a detector monolithically integrated GaAs.
Appl. Phys. Letts.,Vol.37(10),1980,pp.880-882.

[38] J.Blakemore.
Semiconducting and other major properties of GaAs.
J. Appl. Phys.,Vol.53(10),1982,pp.R123-R181.

[39] J.L.Merz,R.A.Logan and A.M.Sergent.
GaAs integrated optical circuits by wet chemical
etching.
I.E.E.E. J. Quant. Electrs.,Vol.QE15(2),1979,
pp.72-82.

[40] A.Yariv and R.C.C.Leite.
Dielectric waveguide mode of light propagation in p-n junction.
Appl. Phys. Letts.,Vol.2(3),1963,pp.55-57.

[41] H.C.Casey,D.D.Sell and M.B.Panish.
Refractive index of $Al_xGa_{1-x}As$ between 1.2 and 1.8eV.
Appl. Phys. Letts.,Vol.24(2),1974,pp.63-65.

[42] E.Garmire,H.Stoll and A.Yariv.
Optical waveguiding in proton implanted GaAs.
Appl. Phys. Letts.,Vol.21(3),1972,pp.87-90.

[43] Molecular Beam Epitaxy.
L.L.Chang and K.Ploog, eds.
NATO Advanced Science Institute Series
Nijhoff, Dordrecht,1985.

[44] Metal Organic Vapour Phase Epitaxy.
J.B.Mullin,S.J.C.Irvine,R.H.Moss,P.N.Robson and D.R.Wight, eds.
North Holland, Amsterdam, 1984.

[45] GaAs Processing Techniques.
R.E.Williams.
Artech House, Dedham, MA, 1984.

[46] S.Adachi and K.Ôe.
Chemical etching characteristics of (001) GaAs.
J. Electrochem. Soc.:Sol State. Sci. and Tech.
Vol.130(12),1983,pp.2427-24335.

[47] P.G.Gloersen.
Ion Beam Etching.
J. Vac. Sci. Technol.,Vol.12(1),1975,pp.29-35.

[48] C.J.Mogab.
Ion beam, plasma and reactive ion etching.
Inst. Phys. Conf. Ser.,No.53,1980,pp.37-54.

[49] R.G.Poulson.
Plasma etching in Integrated Circuit manufacture.
J. Vac. Sci. Technol.,Vol.14(1),1977,pp.266-274.

[50] L.M.Ephrath.
Reactive ion etching for VLSI.
I.E.E.E. Trans. Electr. Dev.,Vol.ED28(11),1981,
pp.1315-1319.

[51] S.Somekh and H.C.Casey.
Dry processing of high resolution and high
aspect ratio structures in GaAs-$Al_xGa_{1-x}As$ for
integrated optics.
Appl. Opts.,Vol.16(1),1971,pp.126-136.

[52] A.P.Webb and C.D.W.Wilkinson.
Ion beam etching of GaAs for Integrated
Optic applications.
Vacuum,Vol.34,1984,pp.159-162.

CHAPTER 5.

PROTON-EXCHANGED WAVEGUIDES.

5.0. INTRODUCTION.

As stated in Chapter 4, titanium in-diffused waveguides were, until recently, the only type of low propagation loss optical waveguides that could be formed in $LiNbO_3$. However, a possible alternative technology has emerged which may offer practical advantages over other $LiNbO_3$ waveguide fabrication technologies i.e. titanium in-diffusion [1], proton-implantation [2] and lithium out-diffusion [3]. The advantages offered by proton – exchange are a substantial refractive index increase (typically 0.12) and an increased resistance to optical damage [4] compared to titanium in-diffused waveguides (damage occurs at power densities $>10W/cm^2$).

Waveguides formed by proton-exchange were first reported by Jackel et al. [5,6] during their investigation into the formation of the $NbO_2(OH)$ compound by complete exchange of $LiNbO_3$ in mineral acids (in particular nitric acid). They also found that incomplete exchange could occur with other acids where there was not a significant concentration of hydrated H+ ions present e.g. $Mg(NO_3)_2 6H_2O$ or $C_7H_6O_2$. Using the weaker acids produced a high refractive index exchange region which behaved as an optical waveguide. High index guides are desirable for the design of several integrated optic components; for small radius curves in ring-resonators and in the design of efficient modulators with improved optical field confinement.

Several undesirable properties soon became apparent in

waveguides formed by this method. The most important property being that the refractive index change only occurred along the extra-ordinary axis, a phenomenon usually associated with lithium out-diffused waveguides [7]. The change limits the usefulness of these waveguides because only modes of one particular polarisation are supported i.e. TE- modes in waveguides formed in X- and Y- cut $LiNbO_3$ and TM-modes in waveguides formed in Z- cut $LiNbO_3$. However Y- cut $LiNbO_3$ undergoes severe surface damage if exchanged for any significant length of time in benzoic acid (more than 5 minutes [8]).

These restrictions have not appeared to limit the diversity of devices that have been reported using this new technology, which include both active and passive devices: ring resonators [9], second harmonic generators [10], high efficiency diffraction gratings [11], Mach-Zehnder interferometers [12], temperature sensors [13], frequency translators [14], mode polarisers [15] and acousto-optic devices [16] as well as lenses [17] and also a combination of proton-exchange and titanium in-diffusion [18] to give guiding of both polarisations. These have all been fabricated using the different cuts of $LiNbO_3$ available.

Among the undesirable characteristics of proton-exchanged waveguides which have been reported, is the gradual decrease of the film refractive index with time to a new lower value. This effect was first noted by Yi-Yan [19] and will be discussed later in this chapter along with methods of stabilising this phenomenon. Other undesirable features to emerge are a reduction in the electro-optic effect [12] in proton exchanged regions and a d.c. extinction effect [20] of the optical waveguide.

This chapter describes the results of an investigation into proton-exchanged waveguides carried out to assess their optical characteristics and their suitability for use in fabricating the standing wave modulator. Methods will be described whereby the refractive index may be stabilised and the bulk electro-optic coefficient maintained.

A great deal of research is currently being undertaken in a systematic study of the optical and other physical properties of proton-exchanged waveguides in $LiNbO_3$. Explanations of the anomalous behaviour of these waveguides due to the changes in the lattice structure has been attempted using micro-analytical methods such as Rutherford Back Scattering [21], X-ray analysis [22], infra-red absorption [23], hydrogen profiling [24] and chemical analysis. Other methods include electron micro-probe techniques [25] and S.I.M.S. [26] to determine the lithium concentration. The results obtained by these methods are not exhaustive but are sufficient to indicate the manner whereby the protons reside in the host lattice. This will be described in section 5.5.

5.1 FORMATION OF PROTON-EXCHANGED WAVEGUIDES.

The optical characteristics of the exchanged waveguides were found by performing a series of experiments on the different major axis cuts of $LiNbO_3$ for a wide range of exchange times and temperatures. The experimental arrangement was described in detail in Chapter 4. The immersion times for the samples ranged from 20 minutes to several hours at melt temperatures of between 180°C and 220°C.

The optical characteristics of the waveguides, such as the depth of the exchange layer and the film refractive index were found using the standard two prism coupling technique [27]. In the calculation of these parameters, certain assumptions had to be made a priori about the index profile. It was assumed that the refractive index had a step-like distribution [28] to which the mode effective indices obtained for each waveguide were superimposed by altering successively the waveguide depth and film refractive index.

The mode effective indices obtained for a wide range of fabrication conditions were used as the input to a computer program which then found the waveguide depth and refractive index. The program used was based on the normalised waveguide dispersion equations of Kogelnik and Ramaswamy [29] which express the waveguide depth and the effective index as normalised quantities V and b respectively where:

$$V = k_o a (n_1^2 - n_2^2)^{1/2} \qquad (5.1)$$

and:

$$b = \frac{n^2_{eff} - n_1^2}{n_1^2 - n_2^2} \qquad (5.2)$$

n_1 : exchange region refractive index

n_2 : substrate refractive index

n_{eff} : effective index

a : exchange region depth

k_o : free space propagation constant

The relationship between V and b is then given by:

$$V(1-b)^{1/2} = m\pi + \arctan\left(\frac{b}{1-b}\right)^{1/2} + \arctan\left(\frac{c+b}{1-b}\right)^{1/2} \qquad (5.3)$$

	FILM REFRACTIVE INDEX	
	X-cut	Z-cut
0.633μm	2.3290	2.3284
1.15μm	2.2477	2.2472
	SUBSTRATE REFRACTIVE INDEX	
0.633μm	2.2025	
1.15μm	2.1517	

FIG.5.1. Film refractive indices for X- and Z- cut $LiNbO_3$.

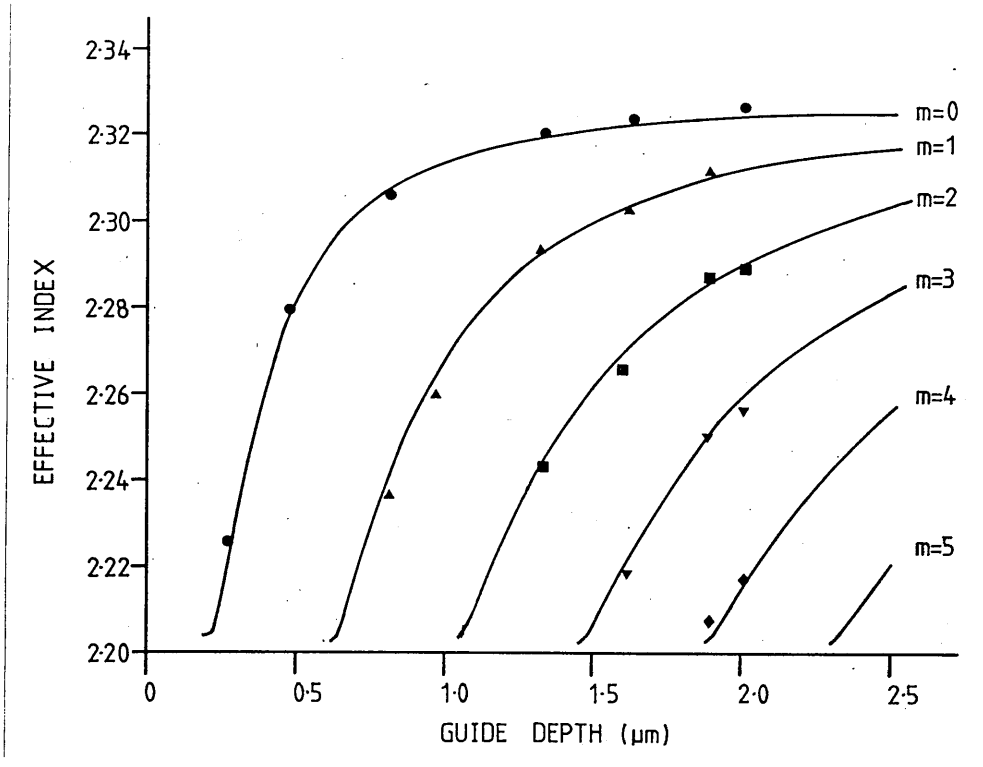

(a)

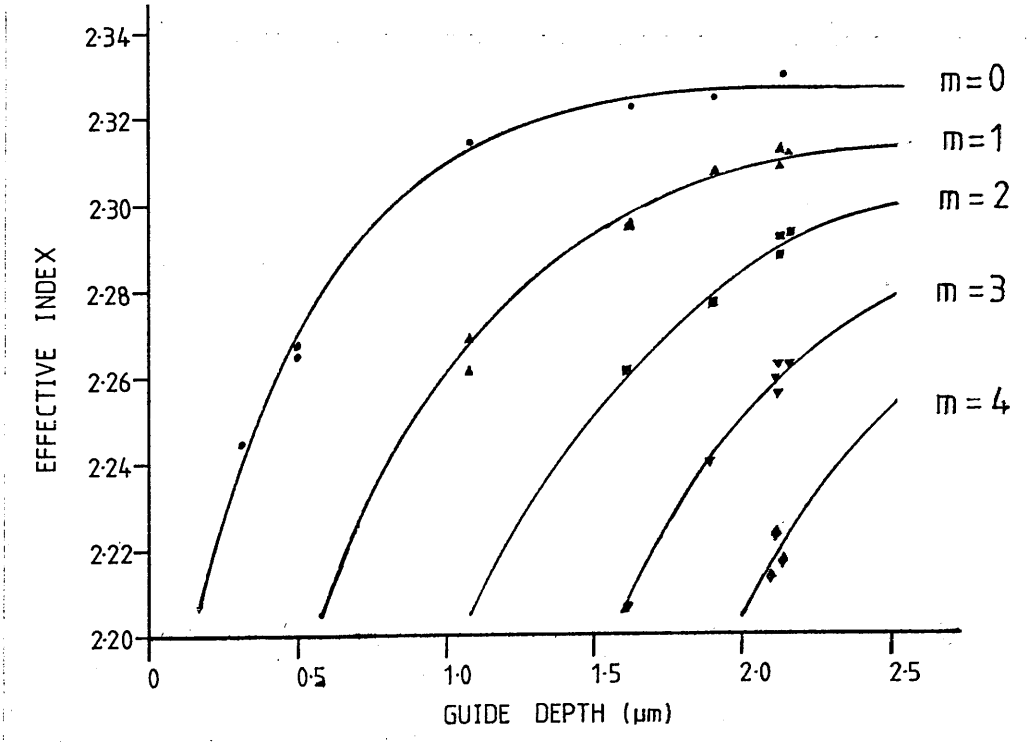

(b)

FIG.5.2. Dispersion curves for (a) TM- and (b) TE- modes in a planar proton-exchanged waveguide.

where c is the asymmetery factor and is defined by the following for TE- and TM- modes:

$$C = \frac{n_2^2 - 1}{n_1^2 - n_2^2} \quad \text{for TE} \; ; \quad C = \left(\frac{n_2 - 1}{n_1^2 - n_2^2}\right) . n_1^4 \quad \text{for TM.}$$

In the program V was gradually incremented between limits set by the number of modes observed in the experimental measurement of the waveguide. The corresponding values of b for each incremented value of V were calculated through the above equation and the corresponding magnitude of n_1 found. This procedure was repeated until the deviation for n_1 obtained for each mode effective index was minimised. Results were obtained in this manner for the waveguides excited at free space wavelengths of 0.633μm and 1.15μm.

A series of planar waveguides in X- and Z- cut $LiNbO_3$ were fabricated by proton-exchange at temperatures in the range from 160°C to 210°C for periods between 30 minutes and 5 hours. From prism-coupler measurements of the optical waveguide modes, the waveguide depths and guiding layer refractive index were found. The values obtained for the guiding layer refractive index (at 0.6328μm) are shown in Fig.5.1. With these values of the guiding layer refractive index, theoretical dispersion curves for TE- and TM- modes in proton-exchange waveguides were constructed and are shown in Fig.5.2. Experimental results are also shown superimposed upon these plots. The values for the mode cut-off thicknesses for both TE- and TM- modes are found when b=0 in Equ.(5.2) and are given in Fig.5.3 at wavelengths of 0.633μm and 1.15μm.

Once the depths of the waveguides had been obtained , they were related to the exchange time and

	Cut-off Depth (μm)			
	X-cut		Z-cut	
	0.633μm	1.15μm	0.633μm	1.15μm
0	0.15	0.35	0.18	0.38
1	0.57	1.23	0.62	1.28
2	1.00	2.12	1.03	2.18
3	1.42	3.00	1.46	3.03
4	1.82	3.89	1.88	3.94

FIG.5.3. Mode cut-off depths for proton-exchanged waveguides in X- and Z- cut $LiNbO_3$.

temperature through the Arrhenius Law [30]:

$$D(T) = D_o . \exp\left(-\frac{Q}{R_o T}\right) \qquad (5.4)$$

where Q is the activation energy in J/mole, T is the absolute temperature in degrees Kelvin at which the exchange was carried out, R_o is the universal gas constant and D_o is a diffusion constant for the process. The depth found from the experimental assessment was related to the temperature dependent diffusion constant through the standard expression:

$$d = 2.(t \times D(T))^{1/2} \qquad (5.5)$$

The activation energy for the exchange conditions was determined by constructing a plot of logD(t) vs. 1/T and measuring the gradient of the line. From Equ.(5.4) the gradient of the line was equal to Q/R.

Values obtained for the temperature dependent diffusion constant for both X- and Y- cut $LiNbO_3$ are given in Fig.5.4.,from which the pre-exponential term was found at the point it intersected the vertical axis at 1/T=0. These values were $4.3.10^{8}um^2/nr$ and $1.8.10^{9}um^2/hr$ and the corresponding activation energies were 84kJ/mol and 94kJ/mol respectively for X- and Z- cut $LiNbO_3$. During this calculation it was assumed that the melt temperature was at the same temperature as the oil. However, a two degree variation in the temperature could lead to a 10% variation in the calculation of the activation energy. Ideally D(t) should be calculated over a far greater temperature range with the actual temperature of the substrate being monotored.

Incorporating the expressions for the diffusion

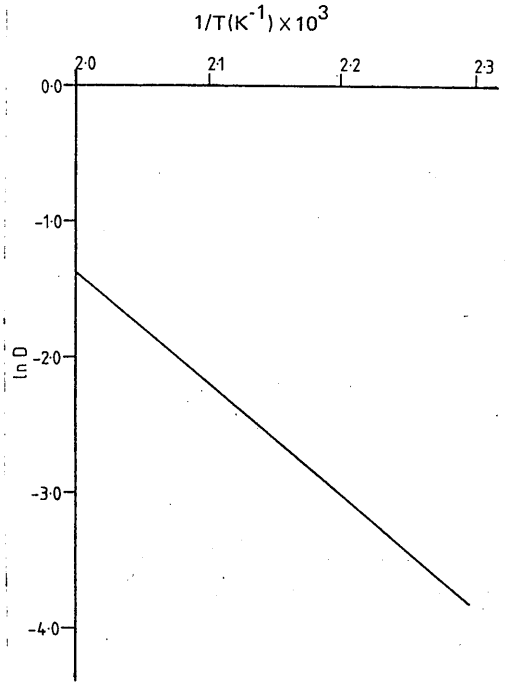

(a)

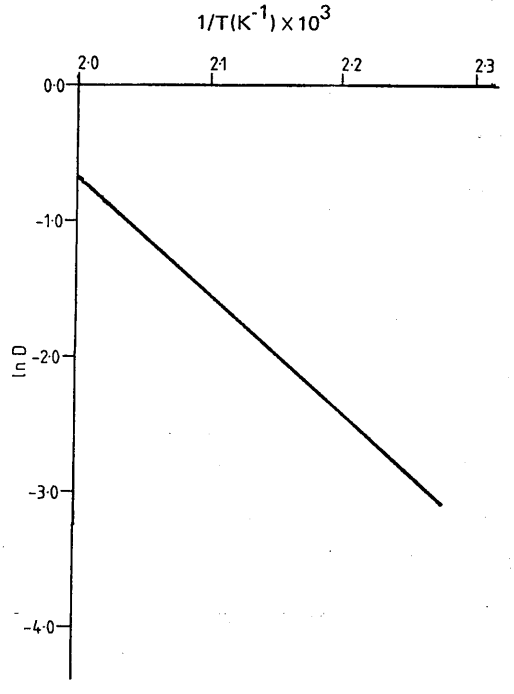

(b)

FIG.5.4. Plot of ln D(t) vs. 1/T for (a) Z- and (b) X-cut $LiNbO_3$.

constants into Equ.(5.5) gave a simple expression for the diffusion depth as a function of the exchange time and temperature. The expressions for X- and Z- cut $LiNbO_3$ are:

$$d = 4.17.10^4.(t)^{1/2}.\exp(-5.05.10^3/T)\ \mu m \qquad (5.6)$$

and:

$$d = 8.58.10^4.(t)^{1/2}.\exp(-5.65.10^3/T)\ \mu m \qquad (5.7)$$

respectively. Plots of Equs.(5.6) and (5.7) are shown in Fig.5.5 from which it is evident that deeper waveguides may be fabricated in X- cut than Z- cut $LiNbO_3$.

5.2 PROPAGATION LOSS MEASUREMENT.

To achieve full scale integration, the optical waveguides formed by a particular fabrication technology should exhibit a very low propagation loss (<< 1dB/cm). In general the loss mechanisms common to optical waveguides can be divided into two main fundamental categories: absorption and scattering. Usually, the overall loss arising from both mechanisms is incorporated in an insertion loss figure which also includes losses arising from reflections at the end faces and mode mismatch. Absorption arises if the wavelength of the incident radiation is sufficient to promote electron transitions within the band structure of the lattice. The scattering mechanism occurs due to defects or discontinuities in the crystal lattice arising from impurities incorporated during the growth proces centres: which act as point sources and radiate in all directions.

Two methods were employed in obtaining quantitative

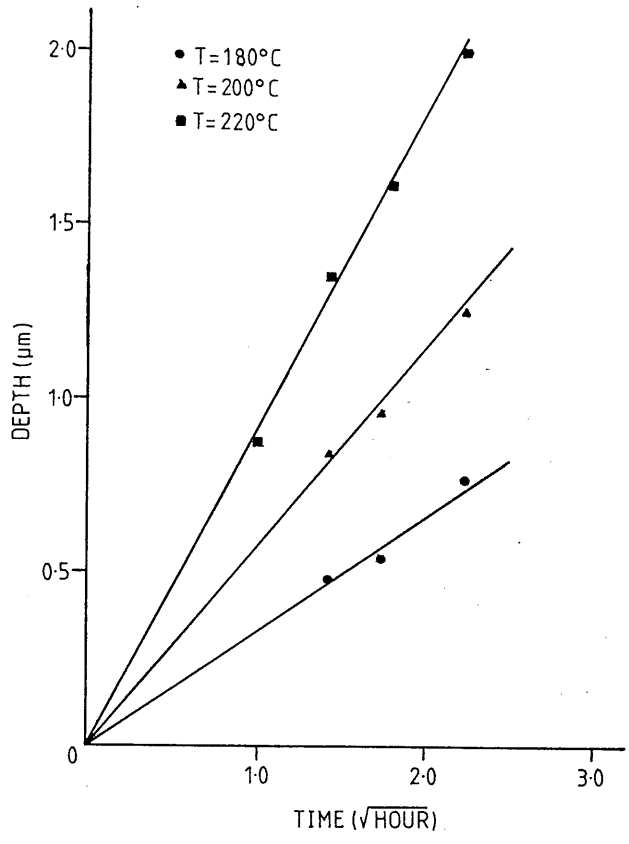

(a)

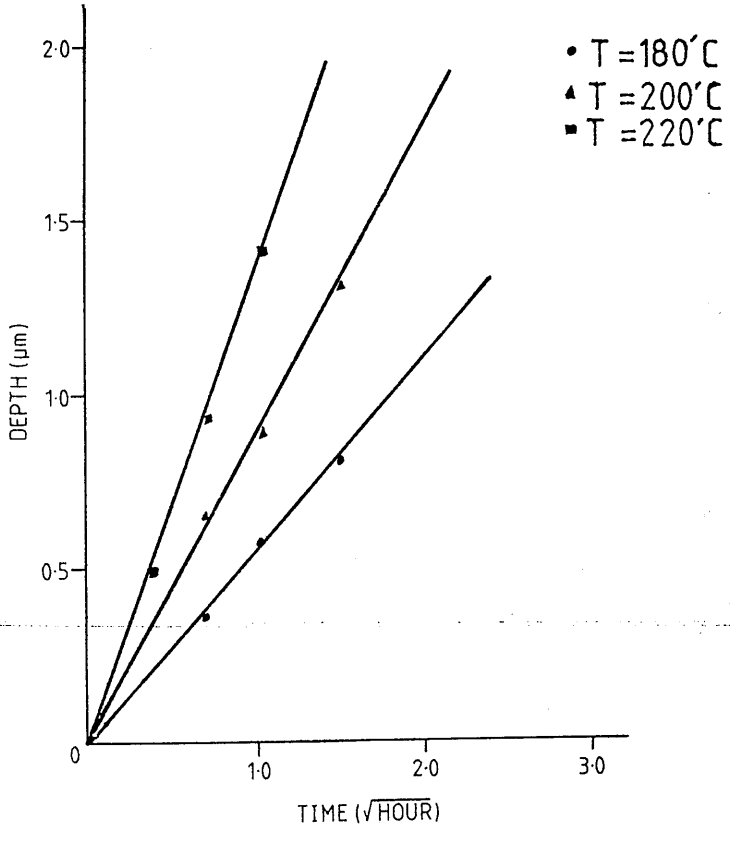

(b)

FIG.5.5. Depth vs. $\sqrt{\text{time}}$ for proton-exchanged planar waveguides in (a) Z- and (b) X- cut $LiNbO_3$.

estimations of the scattering loss in proton-exchange waveguides. The familiar prism coupling method allowed measurement of both the in-plane scatter loss and the total propagation loss. The two prism method was modified by the addition of a third prism [31] to decouple the sensitivity of this method to variations in the output coupling to give the overall propagation loss. Out-of-plane scattering was observed by imaging the scattered light onto a vidicon camera and scanning along the waveguide.

Using the two methods described above the out-of-plane propagation loss was found to lie between 1.3dB/cm and 2.8dB/cm for X- cut $LiNbO_3$ and between 2.4dB/cm and 4.8dB/cm for Z- cut $LiNbO_3$ at 0.633μm. The in-plane scatter was found to lie between 5.2dB/cm and 15dB/cm which was considerably greater than for titanium in-diffused waveguides [32]. There was no clear trend relating the losses to the fabrication conditions and the excitation wavelength. Considerable work still remains to be done in assessing the importance of the purity of the melt and the quality of the $LiNbO_3$ used influences the losses. In particular the reasons for such high losses compared to the values reported by other researchers should be addressed [33].

5.3. STABILITY OF PROTON-EXCHANGE WAVEGUIDES.

5.3.1. ANNEALING OF PROTON-EXCHANGED WAVEGUIDES.

From the results of the preceding sections, it is evident that proton-exchanged planar optical waveguides are capable of supporting several modes even for fairly short diffusion times at low temperatures (typically less than 2 hours at 180°C). However, when

using a pure melt it was found that the initial high index change decreased or relaxed with time. This phenomenon was first reported by Yi-Yan [19] although it should be noted that his fabrication process was carried out in a sealed ampoule. A variation in the film refractive index by as much 0.01 has been observed [34]. In many applications, for example directional couplers, this may seriously impair the performance of such a device by altering the coupling coefficient. In an attempt to alleviate this problem, while retaining the benefits of the high index, two process modifications have been investigated. Both the annealing method [35] and exchange in a dilute melt had already been reported by De Micheli et al. and Jackel et al. [36,37]

The experimental procedure for the annealing process was described in detail in Chapter 4. The post-annealing of proton-exchange waveguides had been reported to reduce the overall propagation loss (principally scattering losses) and to stabilise the refractive index while, at the same time, reducing the sensitivity of the optical waveguide characteristics to the initial conditions, but also allowing the fabrication of single mode waveguides.

A series of experiments were carried out on X- and Z-cut $LiNbO_3$ planar waveguides for a range of exchange times and temperatures to form multi-mode waveguides [35]. These samples were then subsequently annealed at temperatures of 325°C and 400°C in wet and dry atmospheres of gases. The flow rates of the gases were varied to see if this significantly altered the characteristics of the waveguides after annealing. Before the annealing commenced the effective indices of the modes were measured and by analysing these by a

piece-wise linear I.W.K.B. [38,39] technique, the refractive index profile was derived. The variation of the effective indices for Z- cut and X- cut $LiNbO_3$ annealed at 400°C in wet O_2 is shown in Fig.5.6a and 5.6b respectively. It is apparent that the effective index of the second mode for the Z- cut sample exhibited a slight increase when annealed at 400°C which does not appear to be present for the X- cut sample annealed at 400°C. The annealing treatment produced a second diffusion process whereby the protons already present within the lattice diffused deeper into the substrate, this process being essentially a limited source diffusion drive in process.

The unexpected variation of the effective index with annealing may be explained by analysing the refractive index profile by the I.W.K.B. method. The index profiles obtained are shown in Fig.5.7 for X- cut $LiNbO_3$ at 400°C. For annealing times upto 20 minutes the refractive index profile was still step-like although the diffusion depth had doubled and the peak refractive index was slightly reduced by approximately 0.03. For anneal times greater than 20 minutes the index distribution then gradually took on a Gaussian-like profile with a steady decrease in the peak guiding layer refractive index. At the lower anneal temperature (~325°C Fig.5.8) the refractive index distribution remained step like for times up to 4 hours with only an increase in the depth of the distribution and a small decrease in the maximum film refractive index. It was apparent that the anneal temperature had a more significant bearing upon the refractive index distribution than the actual anneal time. The propagation loss also generally exhibited a slight decrease of the order of 1dB at 0.633μm and approximately 1.5dB at 1.15μm.

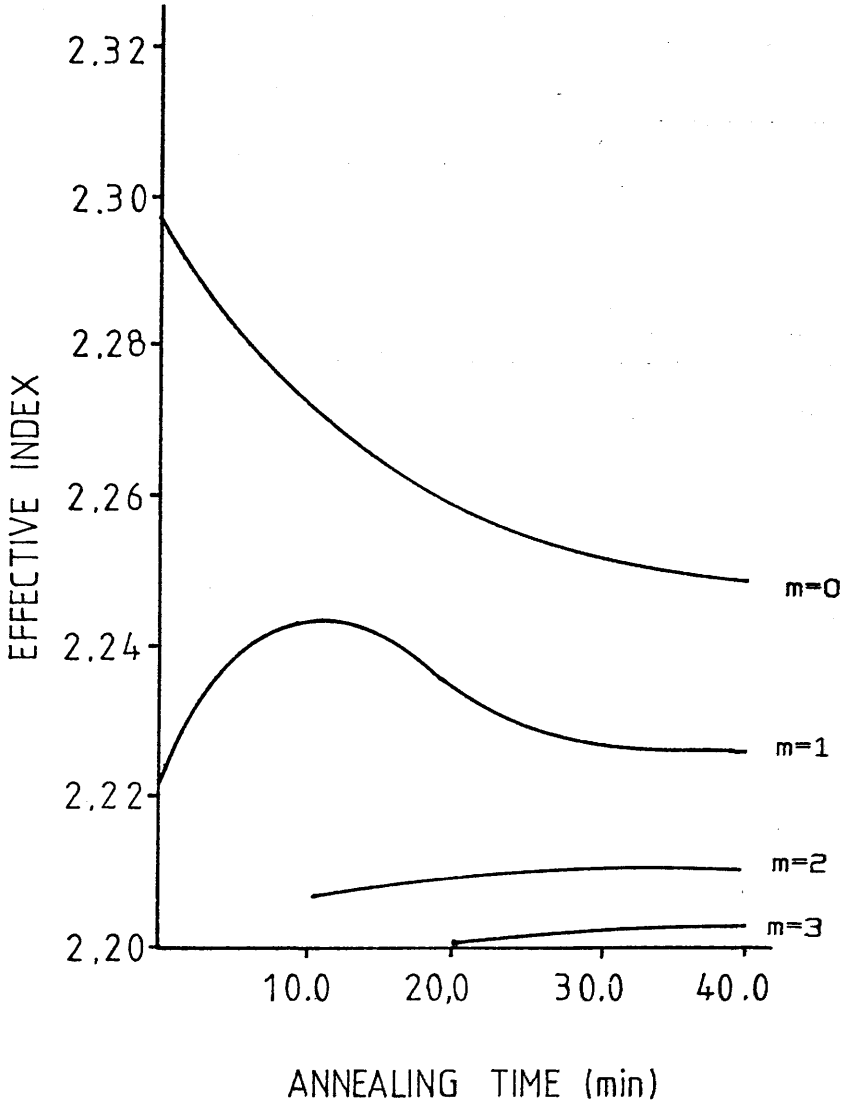

FIG.5.6a. Modal effective indices as a function of annealing time (T=400°C) for Z- cut $LiNbO_3$.

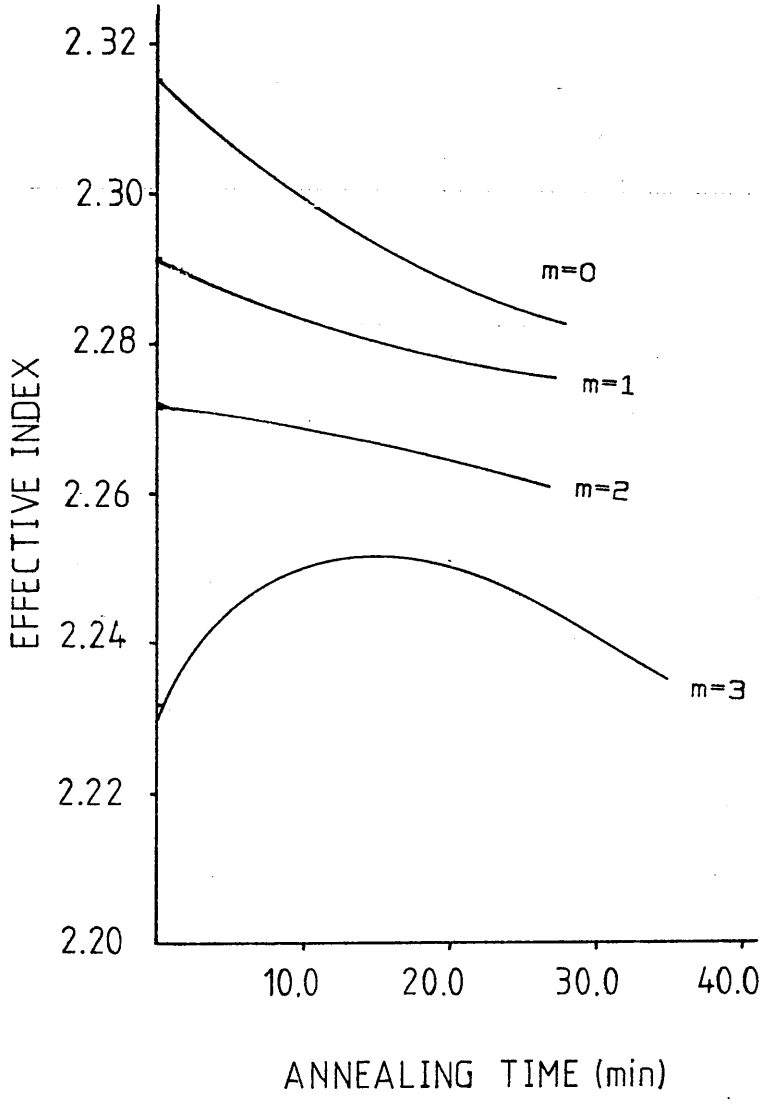

FIG.5.6b. Modal effective indices as a function of annealing time (T=400°C) for X- cut $LiNbO_3$.

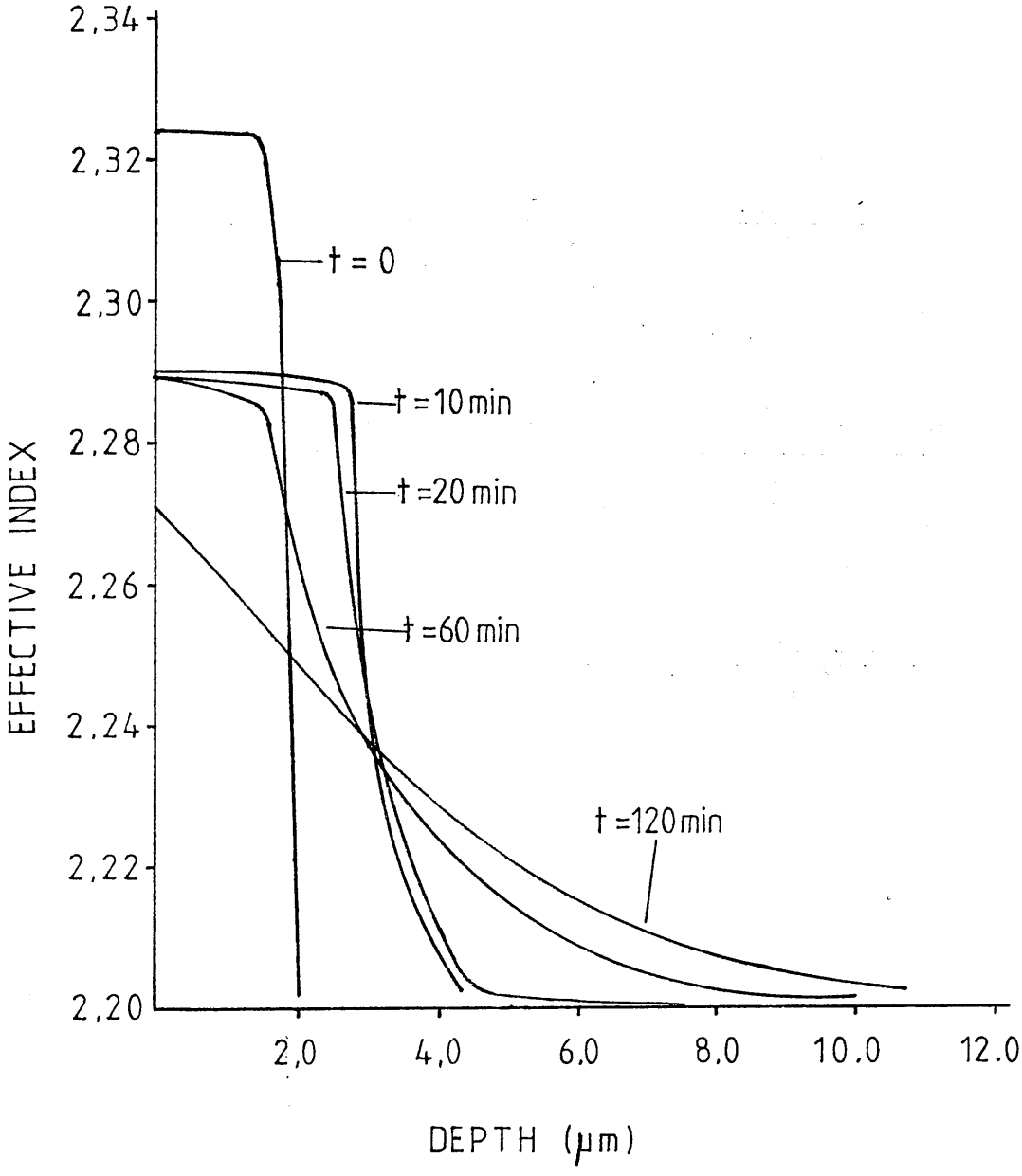

FIG.5.7. Effect of annealing upon the refractive index profile (T=400°C in O_2) of X- cut $LiNbO_3$.

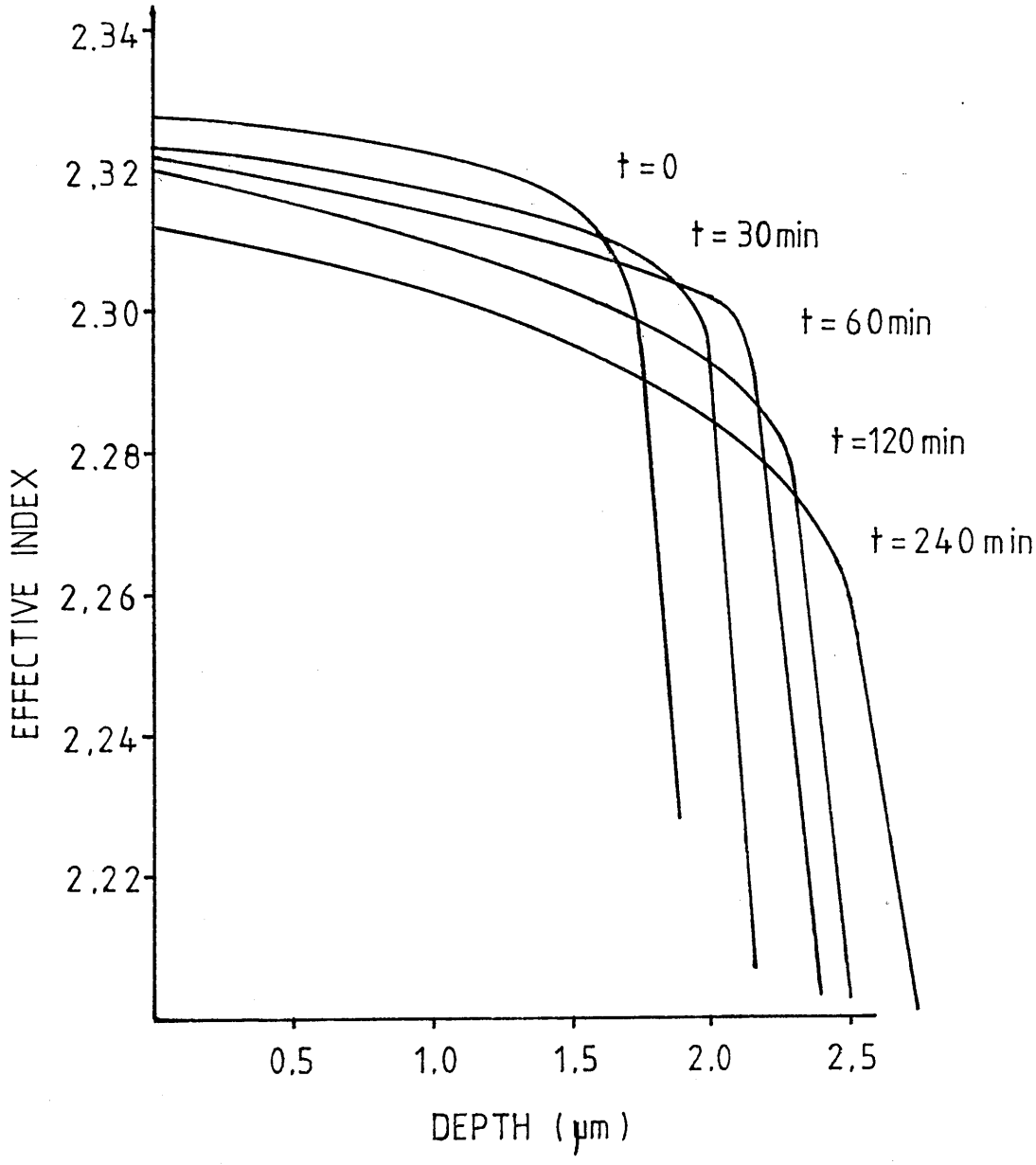

FIG.5.8. Effect of annealing upon the refractive index profile (T=325°C in O_2) of X- cut $LiNbO_3$.

The effect of the rate of gas flow on the annealed refractive index profile during annealing and the importance of an atmosphere saturated with water vapour were not clearly determined in the limited number of experiments carried out. This was partly due to the difficulty of determining the actual temperature of the sample surface. Work still remains to be done on ascertaining the importance of the annealing environment for the process.

5.3.2. PROTON-EXCHANGE USING DILUTE MELTS.

There is another extension to the general proton-exchange method in order to stabilise the refractive index of the waveguides. According to Jackel et al. [40] the proton-exchange process is an equilibrium process which may be written as:

$$LiNbO_3 + xH^+ \rightleftharpoons Li_{1-x}H_xNbO_3 + xLi^+ \qquad (5.8)$$

From the chemical analysis (to be discussed later) the proportion of lithium exchanged at the surface was found to be between 60 and 70%. However Equ.(5.8) does not incorporate the possible inclusion of protons in interstitial positions within the lattice. Therefore, the refractive index increase may be considered to be related to the amount of lithium exchanged and any method which controlled the degree of out-diffusion would also control the refractive index value. Indeed it is interesting to note that the Li/Nb ratio near the stochiometric regime is found to alter only the extra-ordinary refractive index [7].

From the above equation the equilibrium position was adjusted by adding a small quantity of lithium

benzoate salt (typically between 0.25% and 2% molecular weight) into the melt prior to exchange. On addition of lithium benzoate, the lithium ion concentration was increased, giving a decrease in the proton concentration through buffering with the benzoate ion. The increase in the lithium ion concentration and the decrease in the proton concentration push the equilibrium condition (Equ.5.8) to the left, inhibiting the out-diffusion of lithium from the substrate. The method was attractive in that it allowed fabrication of waveguides in all cuts of $LiNbO_3$. The peak refractive index resulting from exchanging in the dilute melt was found to be almost the same (to within 5%) as that obtained by using a pure melt, which was in contrast to De Micheli et al. [36], who found the refractive index to be linearly dependent upon the excess lithium concentration.

Similar expressions to Equs.(5.6) and (5.7) were developed to give the depth of the exchange region from the experimental time and temperature for X- cut $LiNbO_3$. For a 0.5% melt the pre-exponential and activation energy terms in Equ.(5.4) were found to be $2.8.10^6$ um^2/hr and 73kJ/mol respectively for X- cut $LiNbO_3$ which, when compared with the corresponding values for exchange in the pure melt, were reduced by a factor of two hundred and 1.3 respectively. For greater concentrations of lithium benzoate, the degree of control over the refractive index profile and the stability was offset by the increase in the exchange time.

Measured values of in-plane and out-of-plane scattering losses were generally lower, with values of below 2dB being routinely observed for the out-of-plane losses. The above compares favourably with those of

titanium in-diffused waveguides.

5.4. STRIPE WAVEGUIDES FORMED BY PROTON-EXCHANGE.

The preceding sections have been devoted to the characterisation of proton-exchange planar optical waveguides. For device applications, the one dimensional waveguide is of little consequence except for acousto-optic device applications [16] and as a means for obtaining data about the diffusion process and the quality of optical waveguides.

The most important form of waveguide is that which offers confinement in two dimensions, i.e. the stripe optical waveguide. The formation of such waveguides using the proton-exchange method was described in Chapter 4. Stripe optical waveguides were fabricated in both pure and dilute melts for a variety of times and temperatures in order to obtain the fabrication conditions for a single-moded optical waveguide. The annealing of samples which had undergone a brief initial exchange in a pure melt has also been studied. For possible future application of stripe waveguides in communications systems, low-loss waveguides are required. A general figure of merit for such wavegides in the experimental enviroment is the insertion loss. The figure includes the losses due to absorption, scattering, reflection and mode-mismatch between different waveguide sections.

Theoretical dispersion curves for the effective refractive index were constructed for the proton-exchanged waveguides formed by exchange in the pure melt ($\Delta n=0.126$ at $0.633\mu m$ and $\Delta n=0.096$ at $1.15\mu m$) and in a dilute melt (2%) ($\Delta n=0.125$ at $0.633\mu m$ and $\Delta n=0.094$ at $1.15\mu m$). Returning to Chapter 2 the simplest method for

analysing these waveguides, since n_1 is large and the aspect ratio is greater than 1, is the effective index method. However, due to the number of independent parameters which can be used to construct the dispersion curves (for example the width and depth), the most useful way of expressing this data is that shown in Fig.5.9. Here the regions corresponding to a particular number of modes are shown as a function of width and depth.

From this graph, the exchange time and temperature may be found using Equ.(5.6) and (5.7) to give the depth of the waveguide. In constructing this graph it was assumed that the refractive index profile was a step index distribution in each direction. Clearly there will be some latitude in the exact cut-off points depending on the analysis model used to analyse the waveguides. Nevertheless the results should prove valuable in determining the fabrication conditions for single mode operation, if the diffusion conditions are known.

Using the theoretical data given in Fig.5.1 and from the experimentally determined number of modes supported by proton-exchanged waveguides, a comparison between the actual number of modes can be made as shown in Fig.5.10. It is clear that the theoretical and experimental results agree for multi-mode waveguides with width dimensions greater than about 6μm. For narrow waveguides some discrepancy between the theoretically and the experimentally determined number of modes is apparent.

A possible explanation for this may be due to the exchange process occurring through a metallic diffusion mask. During diffusion through a metallic mask, an electric potential is known to exist across the diffusion aperture and this potential places a bias against the

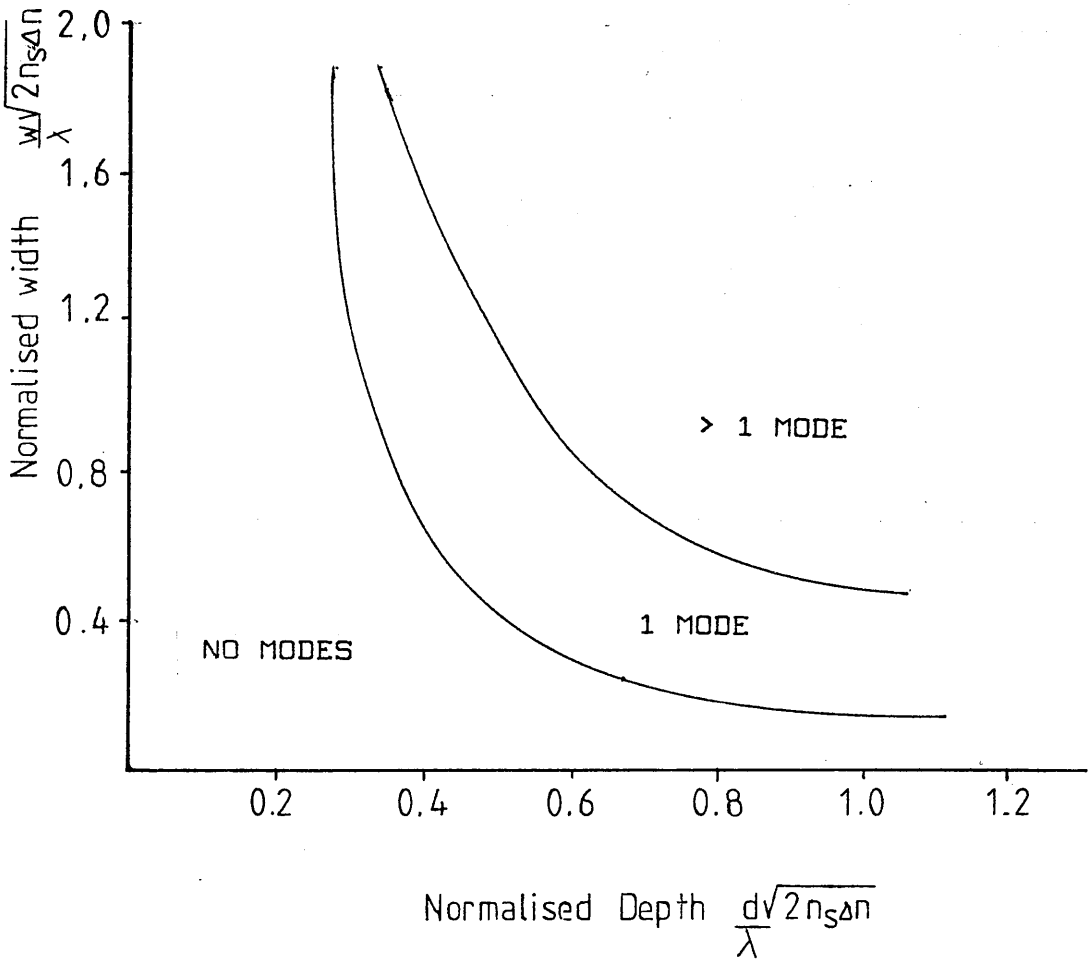

FIG.5.9. Cut-off widths and depths for proton-exchanged waveguides.

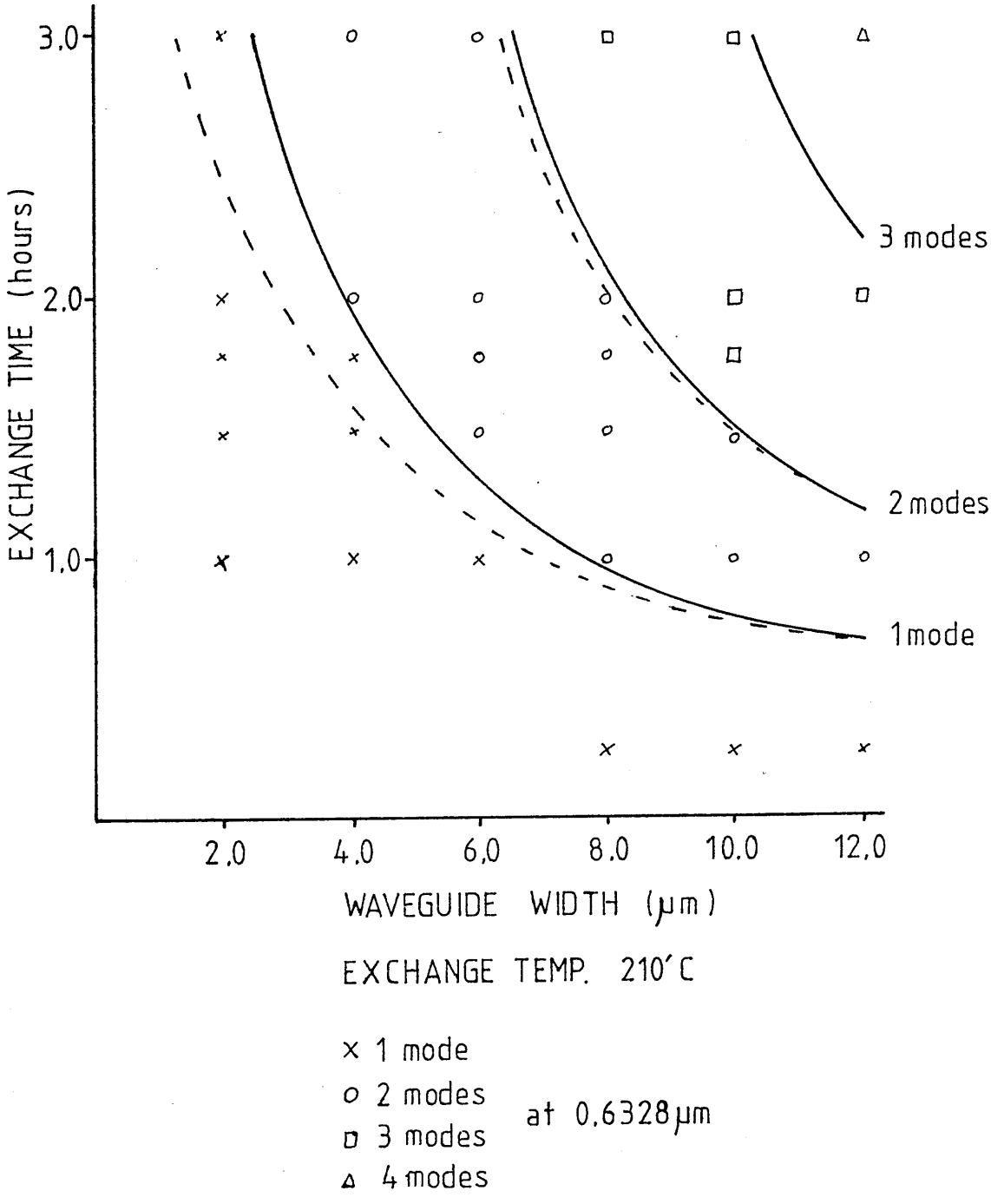

FIG.5.10. Number of modes as a function of exchange time and waveguide width (- - - theoretical curves) for X- cut $LiNbO_3$.

exchange mechanism which inhibits the extent of exchange. This would lead to a reduction in the amount of lithium exchanged for narrow waveguide apertures and a corresponding reduction in the maximum refractive index and diffusion depth recorded. To a certain extent this possibility was corroborated by Sanford et al. [26] who found that for waveguide widths of less than 6μm, there was only a 20% exchange of lithium instead of the normal 70% encountered for large apertures (>10μm). This is again verified by the results shown in Fig.5.10.

The problems encountered with using a metal for the diffusion mask may be modified by using a non-conducting material. The simplest way to achieve a non-conducting mask is to anodise a thin layer of aluminium to Al_2O_3. One method of obtaining a non-conducting mask has been reported elsewhere [40]. Work remains to be done on this aspect of proton-exchange waveguides. However, the reduction in the proportion of lithium that is exchanged for narrow waveguide geometries suggests the possibility of forming single mode waveguides relatively easily.

The insertion losses for proton-exchanged waveguides in X- cut $LiNbO_3$ fabricated in dilute melts are shown in Fig.5.11. Also shown in Figs.5.11 and 5.12 are results for a variety of other fabrication conditions including annealing and exchange in dilute and pure melts. Similar magnitudes for the insertion loss of waveguides formed in Z- cut $LiNbO_3$ were observed.

Waveguides formed in dilute melts or after annealing may be similarly analysed using the effective index method for diffused waveguides. However, more data is required to determine the exchanged region profile before the analysis is performed. The methods

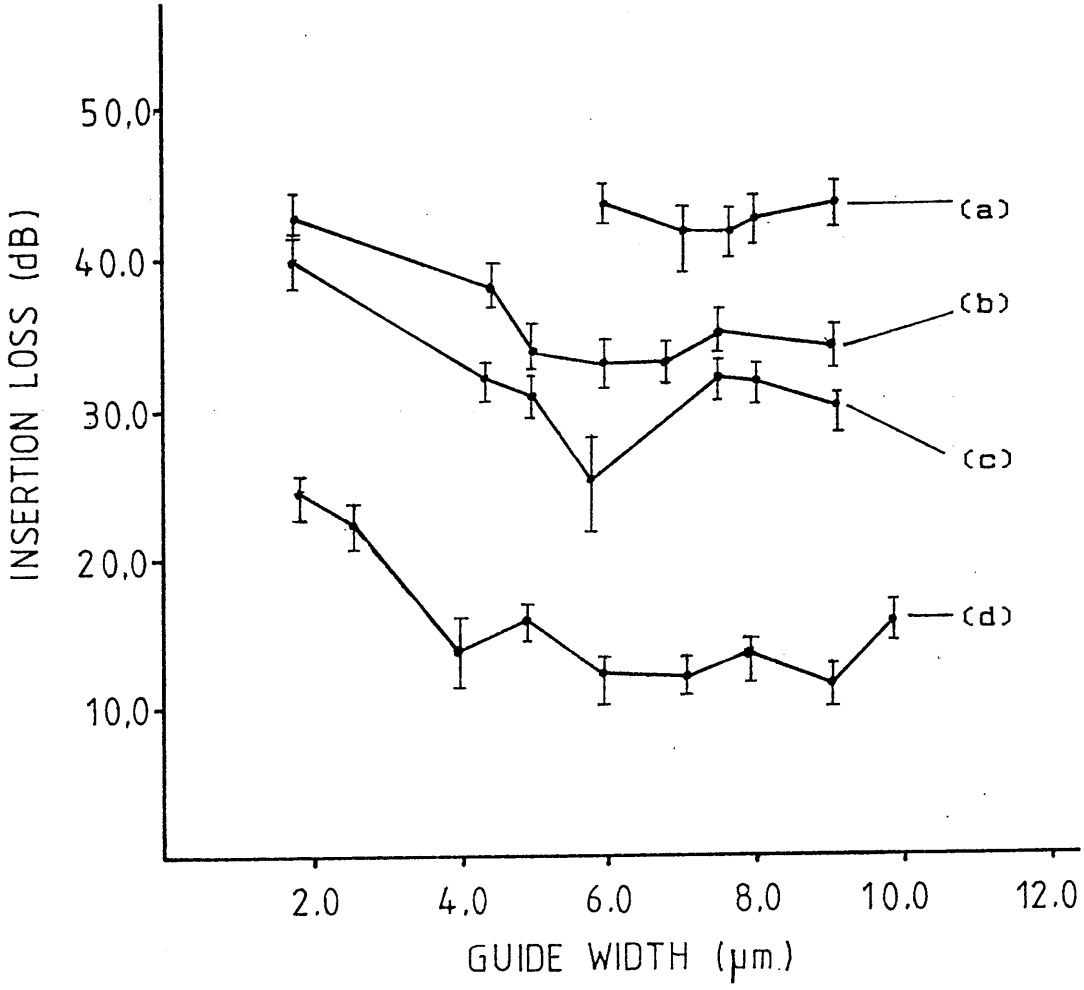

(a) 210°C 10 min.

(b) 210°C 3 hrs.
dilute melt (1%)
annealed 1 hr. 400'C.

(c) 210°C 10 min.
annealed 1 hr. 400'C.

(d) 210°C 3 hrs.

FIG.5.11. Insertion loss vs. waveguide width for different proton-exchanged conditions (X- cut $LiNbO_3$).

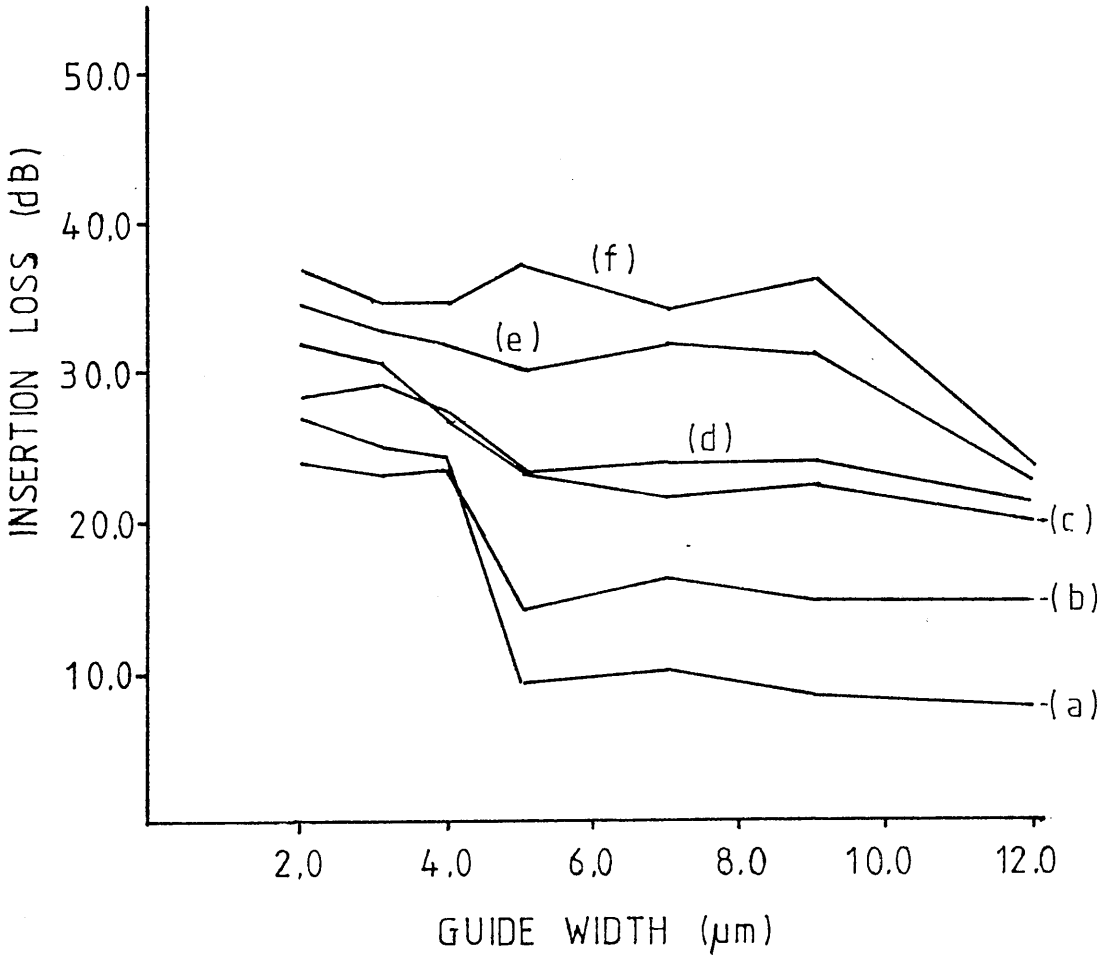

(a) Z- cut 0.633μm (d) Y- cut 0.633μm

(b) Z- cut 1.15μm (e) X- cut 1.15μm

(c) X- cut 0.633μm (f) Y- cut 1.15μm.

FIG.5.12. Insertion loss vs. waveguide width for 400Å Ti:in-diffused waveguides.

available to physically characterise the exchanged region will be described in the following section.

5.5. MICRO-ANALYTICAL TECHNIQUES FOR ANALYSING PROTON-EXCHANGE WAVEGUIDES.

Although proton-exchange waveguides have been well characterised using optical methods it is clearly also desirable to understand the physical process involved in forming these waveguides. As stated in the introduction to this Chapter, several microanalytical methods have been successfully employed in analysing the crystal structure. To recap, these include Rutherford Back Scattering (RBS) [21], Nuclear reactions [24], X-ray diffraction [22], chemical reactions, and Infra-Red absorption [23]. A brief description of each method will now be given, a fuller description can be found elsewhere [34].

In the RBS method, the backscattering of high energy He particles impinging on the sample is monitored. The degree of backscatter is primarily a function of the size of the atoms constituting the target crystal lattice and the concentration of the atoms in the lattice. In the proton-exchange process the concentration of the lithium atoms in the proton exchange layer is reduced by a factor of 60 to 70% [28]. If the orientation of the target is such that planes of high symmetry lie collinear with the direction of the bombarding particles then the incident ions are steered down these channels by Coulombic forces producing a significant decrease in the backscatter count. This phenomenon is used to detect the presence of any surface damage or interstitial atoms incorporated in a variety of sites in the lattice which lead to a local lattice distortion. An example of the data obtained using

this method is shown in Fig.5.13.

RBS is at its most effective when a substantial fraction of the atoms forming the target lattice have a large Z number. For smaller, more compact atoms a complementary technique has to be used to increase the sensitivity. This complementary technique relies upon the generation and detection of high energy gamma rays as a consequence of nuclear reactions between the incident particles and the atoms in the lattice. In applying this method, a certain degree of consideration has to be paid to choosing the correct bombarding particle to give a by-product which is both detectable and sensitive to the desired element present in the lattice. In proton-exchange it is the hydrogen concentration in the exchange layer that is of great interest in characterising the exchange mechanism. The simplest reaction to observe and to characterise the proton concentration present is [41]:

$$N^{15} + H^{1} \longrightarrow C^{12} + He^{4} + 4.43\,MeV\,(\gamma\text{-ray}) \qquad (5.9)$$

where gamma rays are generated only for nitrogen nuclei which have energies within a specific range corresponding to the resonant energy for the reaction.

For energies greater than the resonant energy for the reaction, the nuclei will pass into the exchange region and, in doing so, lose some of their energy through inelastic collisions. When the energy has decreased in this manner until it is equal to the resonant condition, the nuclear reaction takes place. The loss of energy per unit depth through the lattice can be obtained, allowing the determination of the proton concentration as a function of depth. The yield of the

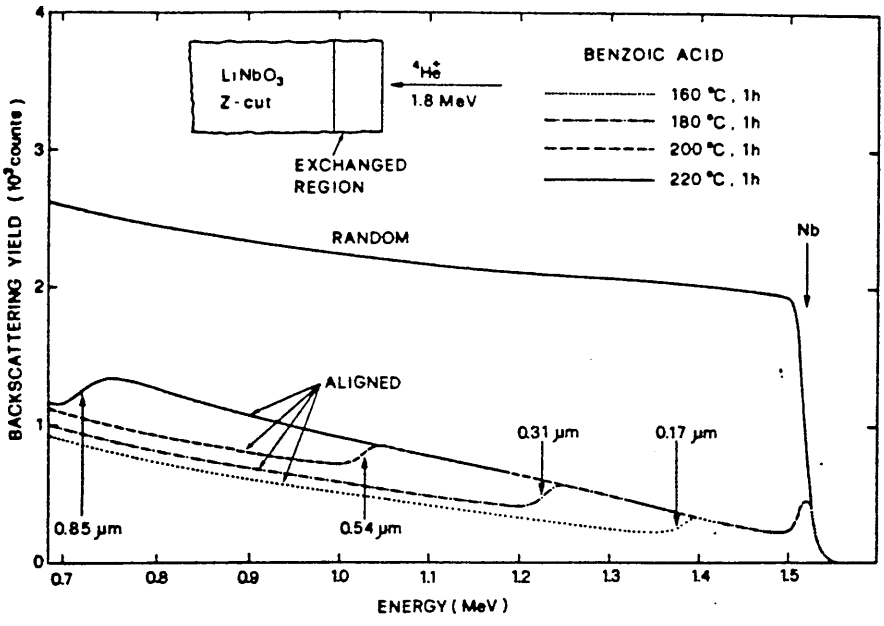

(a)

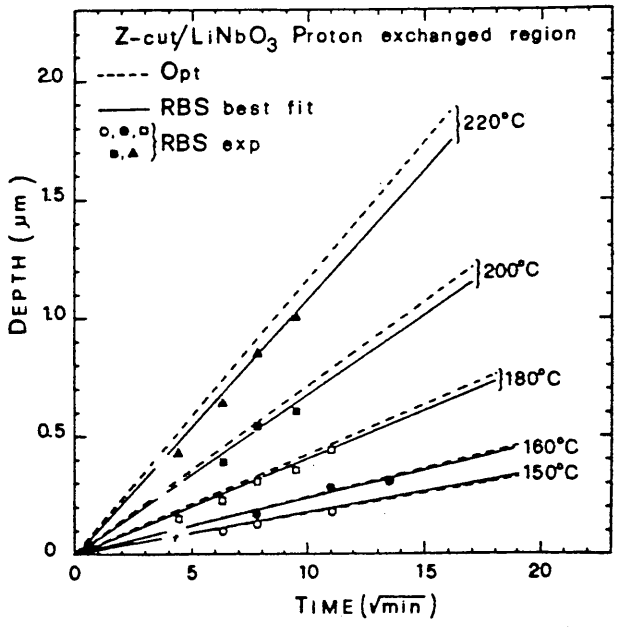

(b)

FIG.5.13. Measured hydrogen profiles for X- and Z- cut $LiNbO_3$ (a) and depth of exchange region measured by R.B.S. and determined optically (b).

radiation from the reaction is in proportion to the proton concentration. This method can provide a depth resolution of 20Å and 0.1% for the concentration although the manner in which the protons bond with atoms in the host lattice cannot easily be determined.

Results obtained from this method are shown in Fig.5.14. The graph also indicates that the hydrogen concentration has a step-like profile,confirming the results obtained from the optical experiments. A comparison between the optical and nuclear reaction methods is also shown in Fig.5.14.

The degree of stress that is present within the lattice after the exchange process is easily monitored by using single or double X-ray diffraction. In X-ray diffraction the constructive interference pattern of reflections of waves from sets of planes in the crystal lattice is monitored. The sample has to be aligned with respect to the incident beam so that the reflections from the subsequent lattice planes produce a phase shift of 180°. For this condition (the Bragg condition) a sharp peak occurs in the reflected radiation. The sharpness or finesse of this peak is related to the regularity of the lattice planes and the homogeneity of the material. If irregularities are present within the material or a different lattice structure is present other peaks will appear in the reflected signal. Typical results obtained by this method are shown in Fig.5.15 and indicate that the lattice undergoes considerable stress during the exchange process. The magnitudes of the double peaks, which are related to the stresses within the lattice, are dependent upon the exchange conditions.

The infra-red absorption method provides information

NUCLEAR REACTION

$H^1(N^{15}, \alpha\gamma)C^{12}$

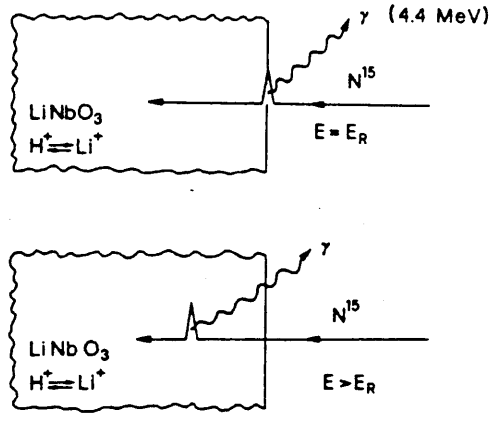

E_R = 6.385 KeV ΔE_R = 3KeV

DEPTH RESOLUTION ≥ 20 Å

SENSITIVITY ≃ 10^{-1} at%

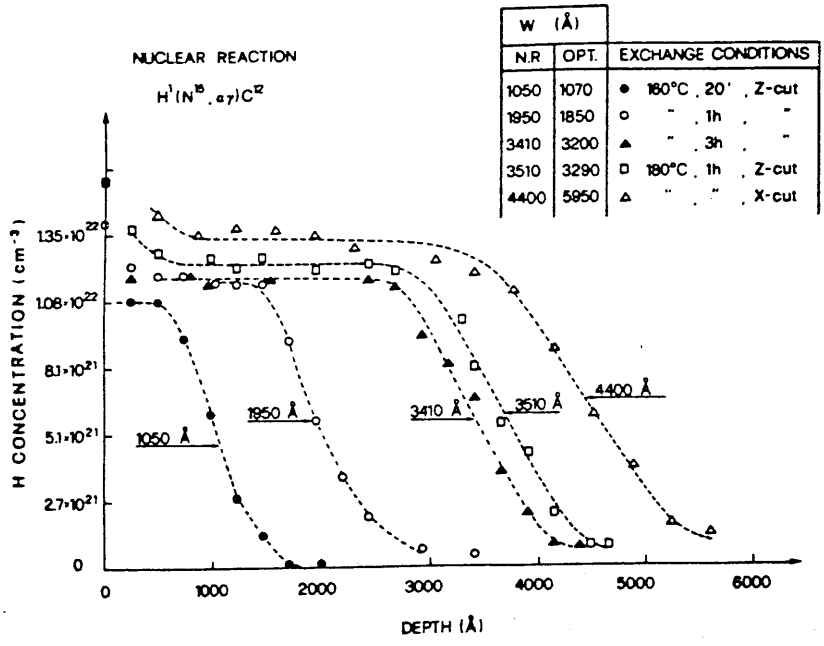

FIG.5.14. Results for hydrogen concentration by nuclear reaction method.

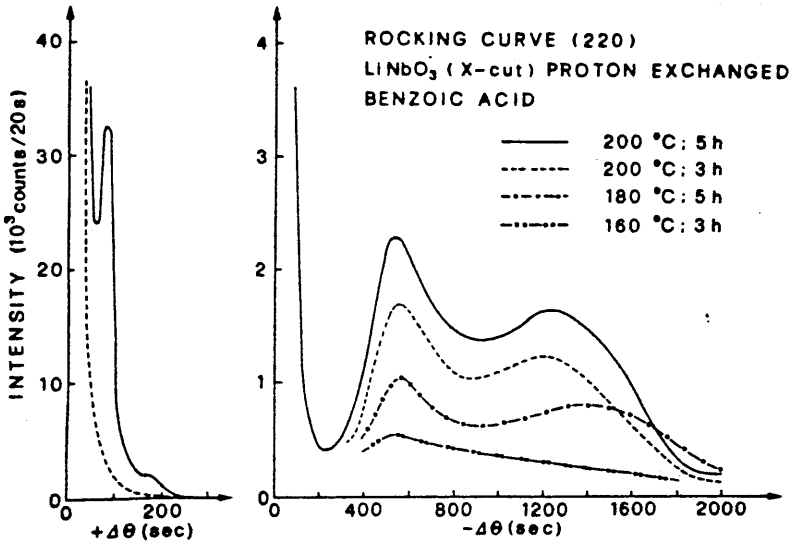

FIG.5.15. X-ray diffraction rocking curves for proton-exchanged waveguides.

regarding the bond formation between the protons and the atoms in the bulk of the crystal lattice and also the orientation of such bonds. For proton-exchange this mechanism leads to the formatiom of hydroxyl groups within the exchange region. The data is obtained by monitoring the transmission of infra-red radiation through a virgin and an exchanged sample and comparing the difference in the absorption spectra obtained.

In Fig.5.16a the peak of the absorption for radiation with the E-field polarised perpendicular to the c-axis for the virgin sample is due to the presence of residual water incorporated within the crystal lattice during growth. Fig.5.16b illustrates an increase at $3506cm^{-1}$ which is polarisation sensitive and a smaller, more diffuse peak at $3280cm^{-1}$ [42] which is polarisation insensitive. The asymmetry of this second peak is attributable to OH bonding occurring with different bond strengths and orientations with respect to the oxygen atoms in the lattice and also a certain degree of H-H bonding as well. This suggests that the exchange process may be either a direct one-to-one substitution into vacant lithium sites or into interstitial positions.

For high temperatures and/or long diffusion times, the infra-red transmission characteristics (Fig.5.16) exhibit a non-linear dependence against $t^{1/2}$ indicating that a non-linear diffusion mechanism is present. Results from the nuclear profiling method do indicate that the proton concentration deviates from a step-like distribution for high temperatures and/or long exchange times which suggests that the diffusion constant for the protons becomes concentration dependent [41].

The final method which can be employed to ascertain the

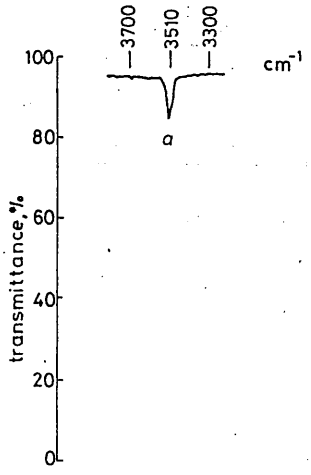

a. Virgin sample.

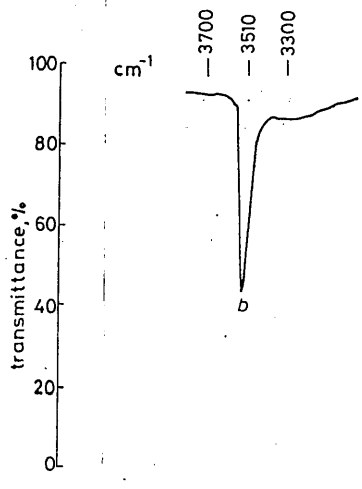

b. Exchanged sample.

FIG.5.16a. Infra-red absorption of virgin and (b) proton-exchanged X- cut $LiNbO_3$.

amount of lithium that diffuses out of the host crystal during the exchange process is chemical analysis of the melt after the exchange, by performing atomic absorption spectroscopy. The expected amount of lithium can be calculated by measuring the dimensions of the sample accurately and determining the depth and hence the total volume of the exchange region. From the total volume of the exchange region and the assumption that 70% of the lithium is exchanged, a value for the mass of lithium out-diffused can then be predicted.

5.6. SUMMARY.

This chapter has introduced the experimental results obtained for the proton—exchange method and compares it with the present titanium in-diffused technology. However, serious problems exist with this technology, the most serious being the stability of the refractive index and the decrease in the electro-optic effect. The decrease in the refractive index may possibly be overcome by modifying the basic proton-exchange procedure by either using dilute melts and/or annealing samples in a suitable enviroment at elevated temperatures. Experimental results presented illustrated the dependence of the optical characteristics upon the exchange conditions. The effect of annealing upon the refractive index distribution was also analysed from measured data forthe modal effective indices using the I.W.K.B. method. A comparison was also made between the scattering and the insertion losses for proton-exchange and titanium in-diffused waveguides. There was no significant correlation between the insertion loss of stripe waveguides and the fabrication conditions, although in general, annealed samples had a slightly reduced insertion loss.

A brief outline of some of the micro-analytical techniques used in obtaining information about the exchange mechanism has also been given. From these methods it was determined that there was a deficiency of upto 60-70% of lithium in the proton-exchanged layer. A proportion of the protons entering the lattice may not only undergo a direct exchange with the lithium ions but also form weak O-H and H-H bonds at interstitial sites in the lattice adjacent to oxygen atons. Proton-exchange nevertheless appears to be a potentially attractive alternative to the 'usual' titanium in-diffusion process.

Work still remains to be done on developing a detailed theoretical model relating the diffusion of protons into lithium niobate. This model would have to incorporate the exchange between lithium and hydrogen and also the formation of weak OH bonds at interstitial positions. The effect of diffusing through apertures in a metal mask must also be addressed to verify the extent to which this fully inhibits the exchange process. The analysis has been attempted for ion exchange in glass [40] and remains to be done for proton-exchange.

References Chapter 5.

[1] R.V.Schmidt and I.P.Kaminow.
Metal diffused optical waveguides in $LiNbO_3$.
Appl. Phys. Letts.,Vol.25(8),1974,pp.438-440.

[2] J.M.Naden and B.L.Weiss.
Ion implanted waveguides in lithium niobate.
Radio and Elect. Eng.,Vol.54,1984,pp.227-230.

[3] J.R.Carruthes,I.P.Kaminow and L.W.Stulz.
Diffusion kinetics and optical waveguiding properties of outdiffused layers in lithium niobate and lithium tantalate.
Appl. Opt.,Vol.13(10),1984,pp.2333-2342.

[4] R.G.Smith,D.B.Fraser,R.T.Denton and T.C.Rich.
Correlation of reduction in optically induced refractive index inhomogeneity with OH content in $LiTaO_3$ and $LiNbO_3$.
J. Appl. Phys.,Vol.39(10).1969,pp.4600-4602.

[5] J.L.Jackel and C.E.Rice.
Topotactic $LiNbO_3$ to cubic perovskite structural transformation in $LiNbO_3$ and $LiTaO_3$.
Ferroelectrics,Vol.38,1981,pp.801-804.

[6] J.L.Jackel,C.E.Rice and J.J.Veselka.
Proton exchange for high index waveguides in $LiNbO_3$.
Appl. Phys. Letts.,Vol.41(7),1982,pp.607-608.

[7] J.G.Bergman,A.Ashkin,A.A.Ballman,J.M.Dziedzic, H.J.Levinstein and R.G.Smith.
Curie temperature, birefringence and phase matching temperature variation in $LiNbO_3$ as a function of melt stoichiometry.
Appl.Phys. Letts.,Vol.12(3),1968,pp.92-95.

[8] M.Goodwin and C.Stewart.
Proton exchanged optical waveguides in Y- cut $LiNbO_3$.
Elec. Letts.,Vol.19(6),1983,pp.223-225.

[9] A.Mahapatra and W.C.Robinson.
Integrated optic ring resonator made by proton exchange in lithium niobate.
Appl. Opt.,Vol.24(15),1985,pp.2285-2286.

[10] M.De Micheli,J.Botineau,S.Neveu,P.Sibillot, D.B.Ostrowsky and M.Papuchon.
Etension of second harmonic phase matching range in lithium niobate guides.
Opt. Letts.,Vol.8(2),1983,pp.116-118.

[11] E.Y.B.Pun,K.K.Wong,I.Andonovic,P.J.R.Laybourn and R.M.DeLaRue.
Efficient waveguide Bragg deflection grating on $LiNbO_3$.
Elec. Letts.,Vol.18(17),1982,pp.740-741.

[12] R.A.Becker.
Comparison of guided wave interferometric modulators fabricated on $LiNbO_3$ via Ti indiffusion and proton exchange.
Appl. Phys. Letts.,Vol.32(2),1983,pp.131-133.

[13] M.Haruna,H.Nakajuma and H.Nishihara.
Optical π-arc waveguide interferometer in proton exchanged lithium niobate for temperature sensing.
Appl. Opt.,Vol.24(16),1985,pp.2383-2484.

[14] K.K.Wong,R.M.DeLaRue and S.Wright.
Electro-optic waveguide frequency translator in $LiNbO_3$ fabricated by proton exchange.
Opt. Letts.,Vol.7(11),1982,pp.546-548.

[15] M.Papuchon and S.Vatoux.
Integrated optical polarisers on $LiNbO_3$: Ti channel waveguides using proton exchange.
Elec. Letts.,Vol.19(16),1983,pp.612-613.

[16] A.Dawar,S.M.Al-Shukri and R.M.DeLaRue.
Surface acoustic waveguided optical wave interaction in Y- cut $LiNbO_3$ annealed proton exchanged waveguides.
I.E.E.E. International Workshop on Integrated Optical and Related Technologies for Signal Processing, Italy, 1984.

[17] Z.D.Yu.
Waveguide optical planar lenses in $LiNbO_3$: Theory and experiments.
Opt. Comm.,Vol.47(4),1983,pp.424-426.

[18] M.DeMicheli,J.Botineau,P.Sibillot,
D.B.Ostrowsky and M.Papuchon.
Fabrication and characterisation of titanium indiffused proton exchanged (TIPE) waveguides in $LiNbO_3$.
Opt. Comm.,Vol.42(2),1982,pp.101-103.

[19] A.Yi-Yan.
Index instabilities in proton exchanged $LiNbO_3$.
Appl. Phys. Letts.,Vol.42(8),1983,pp.269-270.

[20] K.K.Wong,R.M.DeLaRue and S.Wright.
An improved electro-optic waveguide serrodyne frequency translator in X- cut LiNbO3 using proton exchange.
in Proc. First International Conference on Optical Fibre Sensors.
I.E.E., London,1983,pp.72-74.

[21] W.K.Chu,J.W.Mayer and M-A. Nicolet.
Backscattering Spectrometry.
Academic Press.
New York,1978.

[22] C.A.Wallace and R.C.C.Ward.
X-ray diffraction techniques for the analysis of Epitaxic thin films.
J. Appl. Cryst.,Vol.8,1975,pp.545-556.

[23] I.W.Donald and P.W.McMillan.
Review: Infra-red Transmitting Materials.
Part 1. Crystalline Materials.
J. Mat. Sci.,Vol.13,1978,pp.1151-1176.

[24] P.Mazzoldi and G. Della Mea.
The use of nuclear techniques for the analysis of films on glass.
Thin Solid Films,Vol.77,1981,pp.181-193..

[25] K.Sugii,M.Fukuma and H.Iwasaki.
A study of titanium diffusion into $LiNbO_3$ waveguides by electron probe analysis and X- ray diffraction methods.
J. Mat. Sci.,Vol.13,1978,pp.523-533.

[26] N.A.Sanford and W.C.Robinson.
Secondary-ion mass spectroscopy characterisation of proton exchanged $LiNbO_3$ waveguides.
Opt. Letts.,Vol.10(4),1985,pp.190-192.

[27] P.K.Tien and R.Ulrich.
Theory of prism film coupler and thin film light guides.
J.Opt. Soc.Am.,Vol.60(10),1970,pp.1325-1350.

[28] J.L.Jackel,C.E.Rice and J.J.Veselka.
Proton exchange for high index waveuides in $LiNbO_3$.
Technical digest of Integrated and Guided Wave Optics.
Pacific Grove U.S.A.,1982,PDP-1.

[29] H.Kogelnik and V.Ramaswamy.
Scaling rules for thin film optical waveguides.
Appl. Opt.,Vol.13(8),1974,pp.1325-1350.

[30] D.F.Clark,A.C.G.Nutt,K.K.Wong,P.J.R.Laybourn and R.M.DeLaRue.
Characterisation of proton exchanged slab optical waveguides in Z- cut $LiNbO_3$.
J. Appl. Phys.,Vol.54(11),1983,pp.6218-6220.

[31] Y.H.Won,P.C.Jaussaud and G.H.Chartier.
Three prism loss measurements of optical waveguides.
Appl. Phys. Letts.,Vol.37(3),1980,pp.269-271.

[32] M.N.Armenise,C.Canali,M.DeSario,P.Franzosi, J.Singh,R.H.Hutchins and R.M.DeLaRue.
Dependence of In-plane scattering levels in Ti:$LiNbO_3$ optical waveguides on diffusiom time.
I.E.E.Proc.Prt.H,Vol.131(5),1984,pp.295-298.

[33] J.L.Jackel,C.E.Rice and J.J.Veselka.
Proton exchange waveguides for high index waveguides in $LiNbO_3$.
Appl. Phys. Letts.,Vol.41(7),1982,pp.607-608.

[34] A.C.G.Nutt.
Techniques for fabricating integrated optical components on Lithium Niobate.
Ph.D. Thesis,University of Glasgow,1985.

[35] S.M.Al-Shukri et al.
Analysis of annealed proton exchanged waveguides on lithium niobate by optical waveguide measurements and micro-analytical techniques.
7th. Top. meet. on Integrated and Guided Wave Optics.
Kissimmee, Florida,1984,PDP71.

[36] M.DeMicheli,M.Botineau,S.Neveu,P.Sibillot, D.B.Ostrowsky and M.Papuchon.
Independent control of index and profiles in proton exchanged lithium niobate waveguides.
Opt. Letts.,Vol.8(2),1983,pp.114-115.

[37] J.L.Jackel,C.E.Rice and J.J.Veselka.
Compositional control in proton exchanged $LiNbO_3$.
Elec. Letts.,Vol.19(10),1983,pp.387-388.

[38] J.M.White and P.F.Heidrich.
Optical waveguide refractive index profiles from measurement of mode indices: a simple analysis.
Appl. Opt.,Vol.15(1),1976,pp.151-155.

[39] J.Finak and H.Jerominak.
Planar diffusion glass waveguides obtained by immersing in molten KNO_3.
Optica Applicata,Vol.XII(1),1982,pp.11-17.

[40] C.D.W.Wilkinson and R.G.Walker.
Diffusion profile of stripe optical waveguide formed by ion exchange.
Elec. Letts.,Vol.14(18),1978,pp.599-600.

[41] W.A.Lanford.
^{15}N Hydrogen profiling:Scientific Applications.
Nuclear Insruments and Methods,Vol.149,Pt.1, 1978,pp.1-8.

[42] K.K.Wong,A.C.G.Nutt,D.F.Clark,J.Winfield, P.J.R.Laybourn and R.M.DeLaRue. Characterisation of proton-exchanged slab optical waveguides in X-cut $LiNbO_3$. I.E.E. Proc. Pt.J,Vol.133(2),1986,pp.112-116.

CHAPTER 6.

EXPERIMENTAL EVALUATION OF THE STANDING WAVE ELECTRO-OPTIC MODULATOR.

6.0 INTRODUCTION.

The preceding chapters have described the fabrication processes involved in forming optical waveguides in a variety of materials, along with the techniques available for analysing such waveguides. The theoretical analysis of the performance of the standing wave electro-optic modulator was also presented. This chapter draws from these previous sections in the experimental evaluation of the standing wave modulator as a phase modulator [1] and presents the preliminary results obtained. Possible directions for the future development of the modulator design and for increasing the efficiency of such a device will also be discussed in the following chapter.

6.1. EXPERIMENTAL EVALUATION PROCEDURES.

The overall characterisation of the device may be conveniently divided into two parts: evaluation of the microwave behaviour of the electrode structure and the determination of the overall optical modulation performance of the device. The microwave evaluation of the electrode structure will be described first.

6.1.1. OBSERVATION OF THE MICROWAVE CHARACTERISTICS OF THE ELECTRODE STRUCTURE.

The experimental set up for evaluating the microwave response of the device is shown in Fig.6.1. The output from the microwave sweep generator was amplified by the

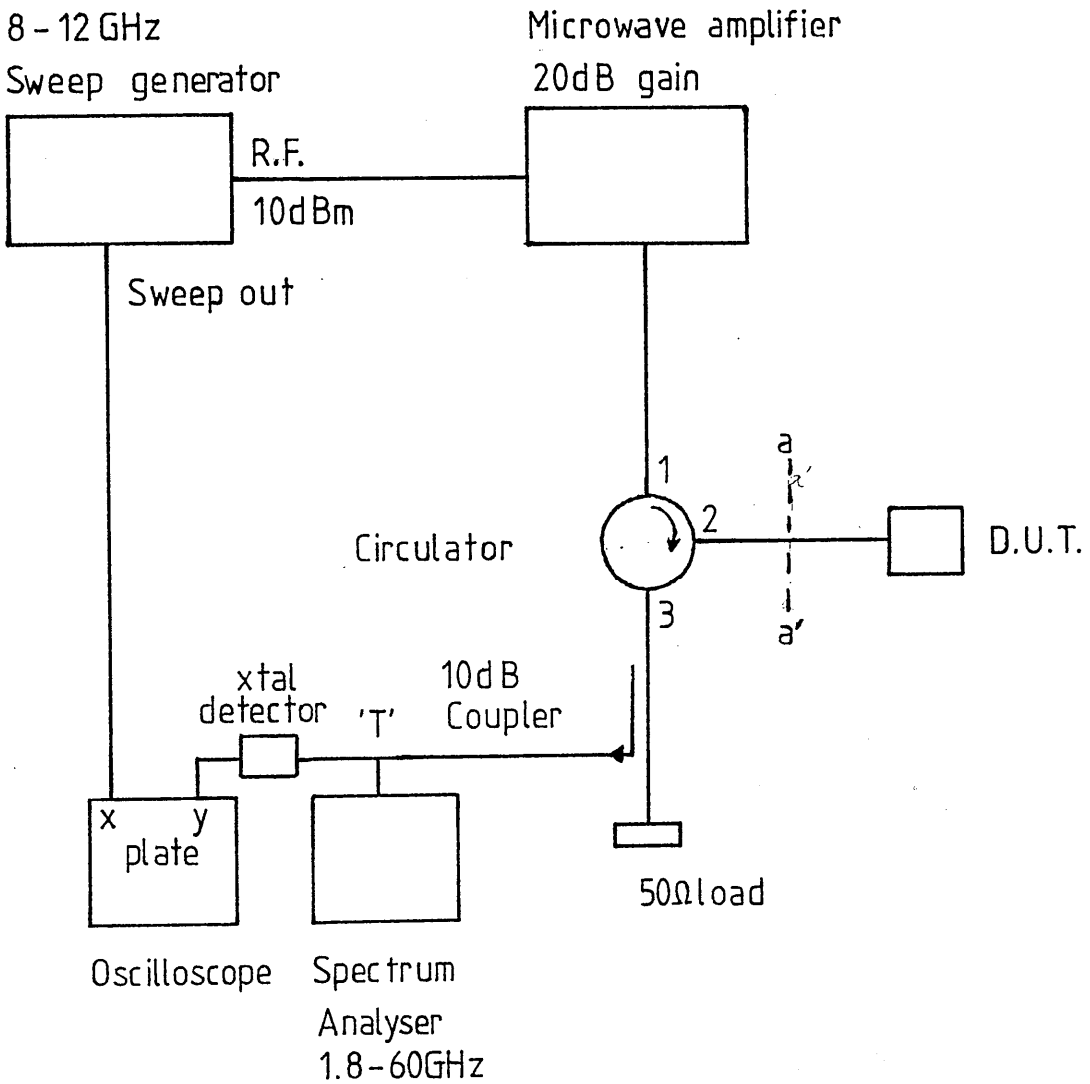

FIG.6.1. Microwave setup to obtain electrode response.

travelling wave amplifier up to a power level of approximately 30dBm. The output from the amplifier was then fed through a circulator which provided isolation between the amplifier and the reflected power from the device under test. The reflected power was sampled at port three by a 10dB directional coupler and absorbed by a 50Ω load terminating the directional coupler. The sampled power was then displayed on a Tektronix spectrum analyser operating in the frequency range 8 to 12GHz.

The transition from the 50Ω coaxial transmission system to the coplanar waveguide structure was achieved by a specially designed brass mount. A plan view and photograph of the mount used is shown in Figs.6.2a and 6.2b. The sample was positioned underneath the protruding centre core of the semi-rigid coaxial cable as shown in Fig.6.2b. Plastic screws were used to apply slight pressure to the base of the sample, after it had been positioned with respect to the centre conductor, to hold it in place and thus ensure good electrical contact. Great care had to be exercised during this procedure to avoid uneven pressure on the sample leading to cracking or scratching of the aluminium pattern.

The reflected power was monitored by the set up shown in Fig.6.1. Some careful adjustment of the sample position in the brass mount was necessary to maximise the resonant response of the device. A typical trace produced for the resonant response is shown in Fig.6.3, which was obtained for a device length of 3.6mm and a metal thickness of 1.8μm, derived through the photo-lithographic techniques outlined in Chapter 4. The trace indicates that there was a definite resonance dip at approximately 10GHz: at 9.875GHz, a relative error of some 2% from the design specification.

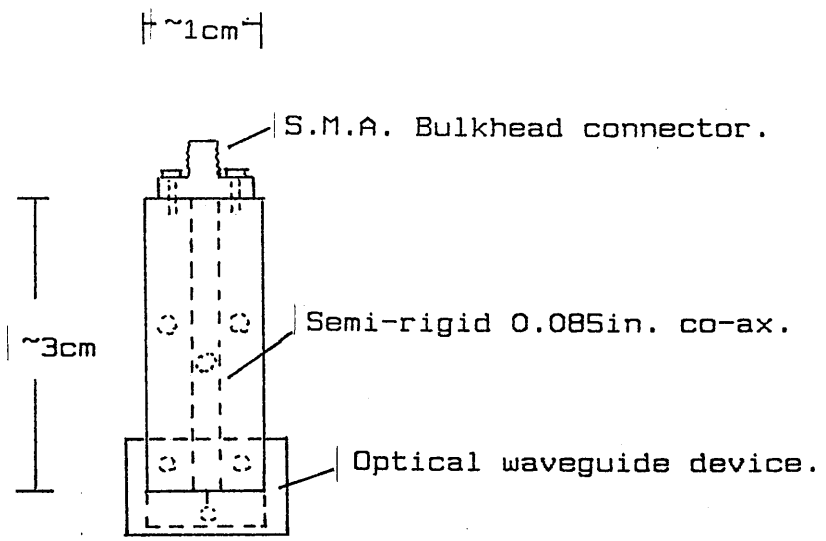

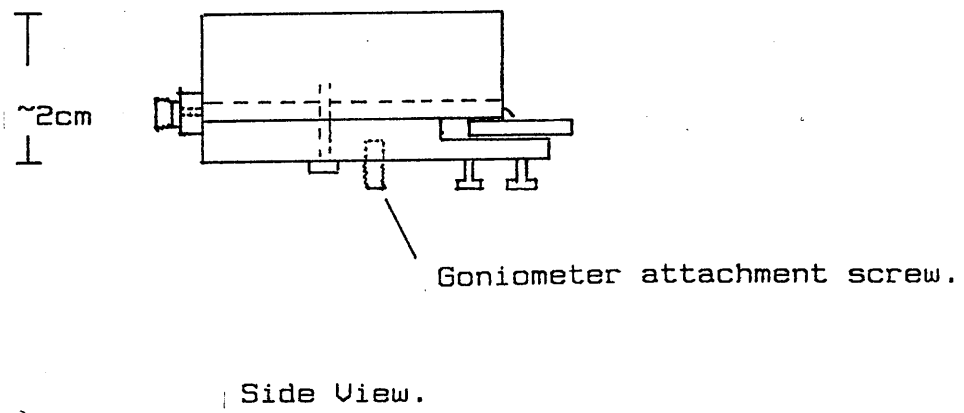

FIG.6.2a. Diagram of sample R.F. mount.

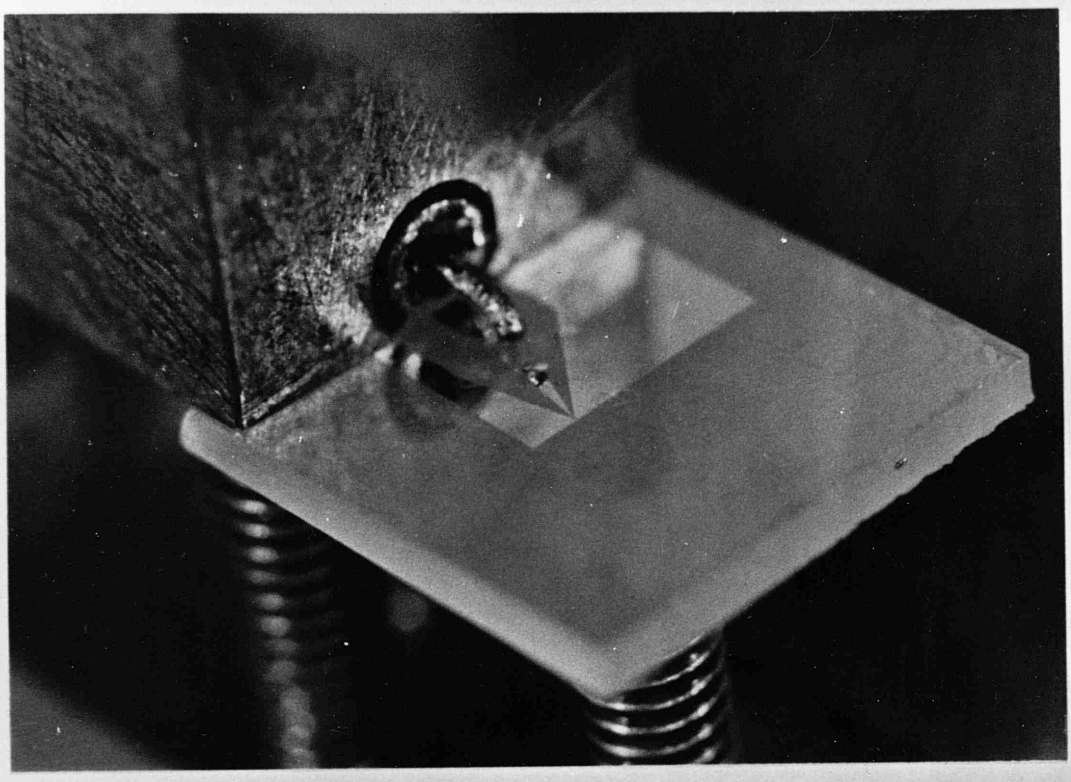

Fig 6.2b Photograph of sample R.F. mount

There are at least two possible explanations for the resonance occurring at a frequency slightly below 10GHz: the exact values of the dielectric constants were taken as those quoted elsewhere in the literature [2], without any immediate experimental evidence to support these values. Also the actual spatial position and impedance of the short circuit at the ends of the resonant line would be difficult to ascertain. The error in the resonant frequency corresponds to an error in the resonant line length of approximately 40μm or 1%.

6.1.2. DETERMINATION OF THE COUPLING COEFFICIENT, EXTERNAL, LOADED AND UNLOADED Q.

Information on the magnitude of the coupling coefficient between the driving transmission line and the resonant line was determined from the trace of Fig.6.3. The loaded, unloaded and external Q were also derived from this figure. The values obtained for these parameters will now be calculated.

From Fig.6.3. the reflection coefficient can be obtained from the reflected power Pr [3] and is given by:

$$P_r = 10\log_{10}\cdot|\rho|^2 \qquad (6.1)$$

from which the V.S.W.R. can be found from:

$$\Gamma = \frac{1 + |\rho|}{1 - |\rho|} \qquad (6.2)$$

The V.S.W.R. at each frequency is plotted on a graph to give the coupling coefficient k [3]:

$$k = \frac{1}{\Gamma_{f_0}} \quad \text{Undercoupled} \qquad (6.3a)$$

$k = \Gamma_{f_0}$ Overcoupled. (6.3b)

Some experimentation was necessary to determine whether the electrode structure was under- or overcoupled to the drive transmission system [3]. As is shown in Fig.6.4., the coupling parameter 'k' was almost unity at 9.85GHz, indicating that the system was nearly critically coupled. However, by inserting a slotted line into the experimental set up, as shown in Fig.6.1., at plane aa' and observing the change in the detuned short position close to resonance the system was found to be slightly overcoupled. From the data shown in Figs.6.3 and 6.4, a value of 0.923 was found for the coupling coefficient.

The values obtained for the loaded, unloaded and external Q were found by simply substituting the coupling coefficient into the expressions given in [3] to obtain the half-power V.S.W.R. corresponding to these different Qs. For completeness these expressions are given below:

$$\left(\Gamma_{1/2}\right)_0 = \left[2 + k^2 + \left(4 + k^4\right)^{1/2}\right]/2k \qquad (6.4)$$

$$\left(\Gamma_{1/2}\right)_\ell = \left[1 + k + k^2 + (1+k)\left(1+k^2\right)^{1/2}\right]/k \qquad (6.5)$$

$$\left(\Gamma_{1/2}\right)_{ext} = \left[1 + 2k^2 + \left(1 + 4k^2\right)^{1/2}\right]/2k \qquad (6.6)$$

From the half-power V.S.W.R. the half-power frequencies are easily found from Fig.6.4. and on substitution into Equ.(6.7) produce the relevant Q:

$$Q = \frac{f_0}{f_1 - f_2} \qquad (6.7)$$

With the results shown in Figs.6.3 and 6.4, the various Q values given in Fig.6.5 were derived.

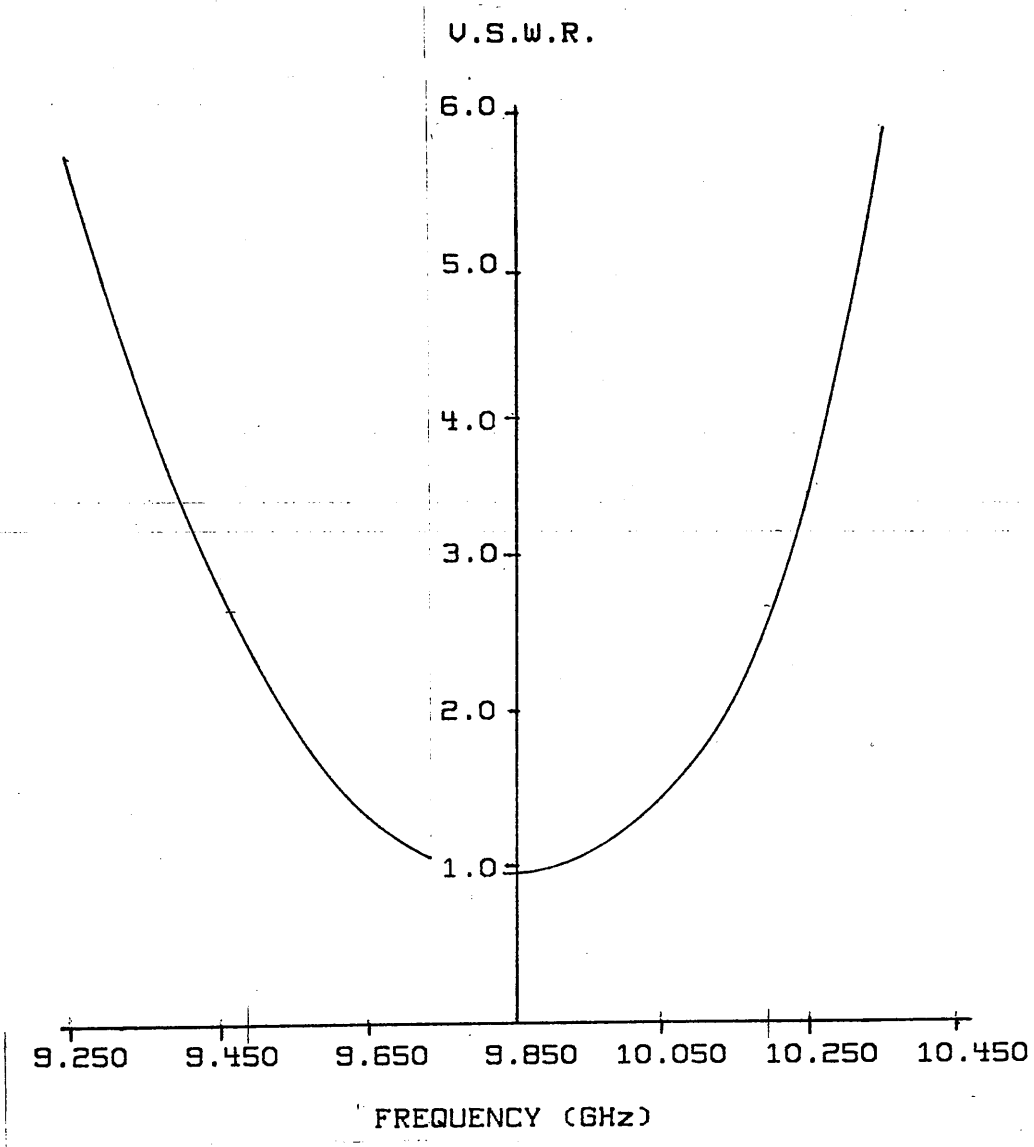

FIG.6.4. V.S.W.R. of device over operating range.

The results presented in Fig.6.5. show that the experimental loaded Q of the system agreed to within 5% with the initial theoretical design values i.e. Q_o=20 and Q_l=10 for a coupling coefficient of 1. With the resonance occurring at a frequency lower than 10GHz immediately suggests that the there was some error in calculating the resonant line electrical length. The calculation was solely dependent upon the effective dielectric constant of the material which was assumed to be 18, a figure generally quoted by other researchers [4], and the physical line length.

An unloaded Q of less than 20 indicated that the loss within the resonant line was marginally greater than that expected,which could be attributable to variations in the metal thickness along the length of the electrode, and in the bulk resistivity of the material.

Using the theoretical description outlined in Chapter 3 and the computer model explained therein, the response of the device was matched to the experimentally observed response by adjusting the line characteristic impedance and the electrical loss present in the resonant line [1]. The comparison between the theoretical and the experimentally determined attenuation constant and characteristic impedance is given in Fig.6.5. In each case there was an error of less than 10% between the attenuation constant and characteristic impedance which indicates that the model developed in Chapter 3 is adequate to explain the microwave operation of the device.

The greatest uncertainty was in calculating the electrical line length and the characteristic impedance

	Theoretical	Experimental
Q_o	20	22.3
Q_1	10	9.48
Q_{ext}	20	16.5
Z_o	50Ω	46Ω
α	1.9dB/cm	2.0dB/cm

FIG.6.5. Comparison between experimental and theoretical Q's.

of the coplanar waveguide, which are both dependent upon the dielectric constant. In an attempt to eliminate this uncertainty, the dielectric constants for $LiNbO_3$ were determined over the frequency range 8 to 12GHz by a technique that will now be described.

6.2. MEASUREMENT OF THE PRINCIPAL DIELECTRIC CONSTANTS OF $LINBO_3$.

The crystal structure of $LiNbO_3$ is uniaxial and therefore exhibits two independent dielectric constants along the principal axes. The values derived from any measurement of these dielectric constants will give either the value for the constant stress (low frequency) or the constant strain (high frequency) condition. In the investigation carried out here the dielectric constants relating to the constant strain or clamped condition were obtained [5].

A swept frequency technique was developed whereby the two independent dielectric constants could be determined easily. These dielectric constants were derived from the principle that materials which exhibit large dielectric constants can behave as resonators under suitable excitation conditions. The theory for the behaviour of such a device was formulated from the simple analysis of optical dielectric waveguides given by Knox et al. [6] and Kim et al. [7]. The anisotropy of the crystal was not taken into account in this analysis. However, as will be described later on it was not necessary to do so if the cystal was orientated correctly. The error introduced by this omission was found to be negligible.

The design of a dielectric resonator to operate at a particular frequency depends upon the dimensions [8,9] of

the sample and the dielectric constants of the material. Consequently, by investigating the behaviour of a resonator with known dimensions and crystal orientation, a figure for the dielectric constants may subsequently be found. To ensure that there was no ambiguity concerning the mode field profile excited, only the fundamental resonance was investigated. The mode designation within the dielectric slab resonator for TE-like and TM-like modes is shown in Fig.6.6.

The experimental method adopted for exciting a resonant mode within the resonator is shown in Fig.6.7. A resonant mode can exist within a dielectric slab by virtue of the large dielectric discontinuity which exists at the air/material interfaces. At this interface an evanescent field extends outside the dielectric into the surrounding medium. Total internal reflection of wavefronts impinging on the boundary from within the material occurrs, and if the total phase shift on one complete path is a multiple of 2π radians then resonance will occur. Coupling to the resonant mode is achieved simply through matching of the external electric (or magnetic) field profile to that of the evanescent field. The field orientation of the external field has to be similar to the evanescent field distribution for coupling to take place.

In the analysis, it is assumed that the presence of the metal waveguide walls do not substantially perturb the resonant mode field distribution within the dielectric resonator. By placing the dielectric resonator within an oversized waveguide the above condition can be achieved.

The sample of $LiNbO_3$ to be examined was placed inside a

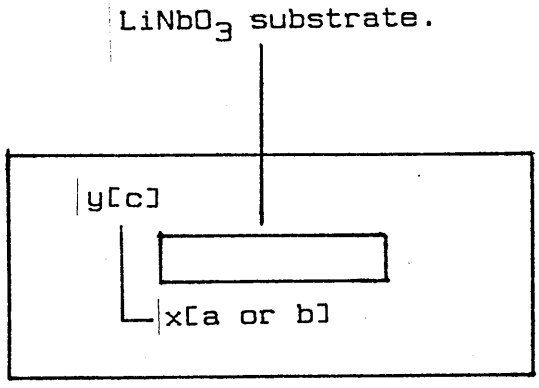

Excitation of $E^{y}_{11\delta}$ mode (TM-like).

Crystal axes orientation for Z- cut $LiNbO_3$ within metal waveguide.

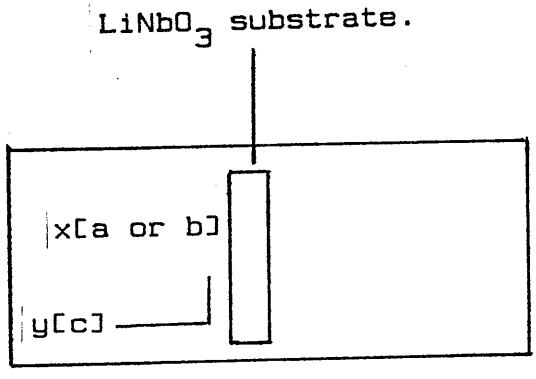

Excitation of $E^{x}_{11\delta}$ mode (TE-like).

FIG.6.6. Excitation of modes within dielectric resonator and substrate orientation.

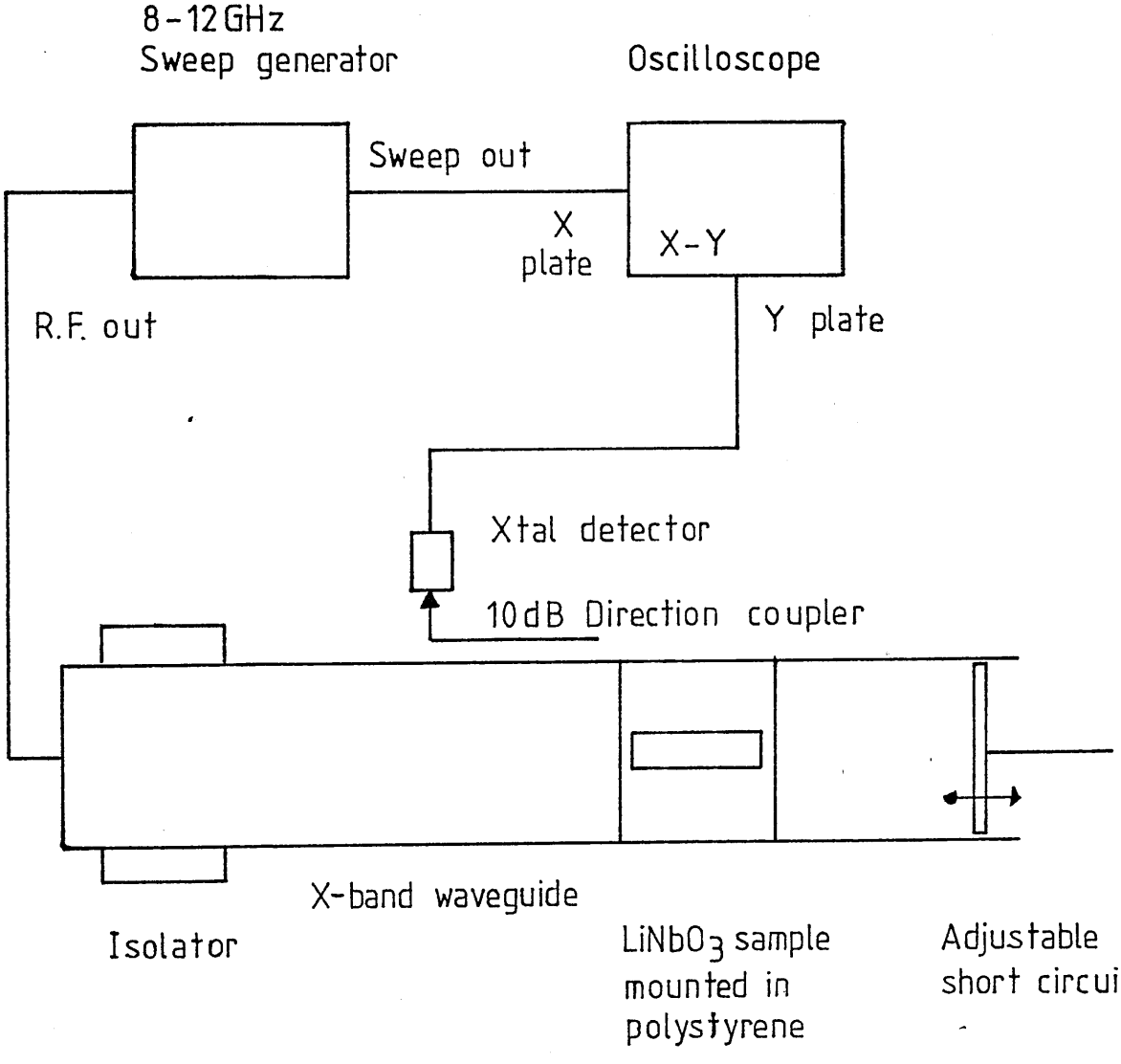

FIG.6.7. Experimental microwave setup to investigate the dielectric resonator.

section of X-band waveguide and held in place by a piece of expanded polystyrene. Referring to Fig.6.7., the reflected power from the short circuit was monitored through a 10dB directional coupler terminated by a crystal detector. The output from the detector was then fed to the Y-plate of an oscilloscope with the sawtooth output from the sweep generator driving the X-plate. In the X-Y mode of operation the oscilloscope diplayed the reflected power as a function of frequency.

When the excitation frequency corresponded to that of a resonant mode, a sharp dip in the reflected power trace was observed. The adjustable short circuit at the end of the waveguide allowed control of the coupling to obtain critical coupling. The short circuit was carefully adjusted until the dip was maximised.

Once the resonance condition had been found for the fundamental mode the dielectric constants along the principal axes were calculated. This was done by using a slight modification to the theory of optical waveguide analysis given by Knox et al. [6] and subsequently enhanced by Kim et al. [7] for an embedded waveguide with a significant proportion of the energy in the surrounding cladding.

Adapting Marcatili's nomenclature [10] to the electric field distribution within the resonator, the fundamental mode is designated $E_{11\delta}$ where δ indicates a fraction of a wavelength along one of the orthogonal axes. The resonance condition occurred when the electrical length of the sample was a multiple of pi radians (the ends of the sample coincided with a minimum in the electric field distribution).

Following Knox et al. [6] the longitudinal propagation constant is expressed in terms of the transverse propagation constants using the effective index concept. These are:

$$k_x a = 2\arctan\left[\frac{k_x^2 - k_o^2(\epsilon - 1)}{k_x}\right]^{1/2} \cdot \xi \qquad \xi = \begin{cases} 1 & TE \\ \epsilon \\ \epsilon_{eff} \end{cases} TM \quad : \epsilon = \epsilon \text{ or } \epsilon_{eff} \tag{6.5}$$

and:

$$k_y b = 2\arctan\left[\frac{k_y^2 - k_o^2(\epsilon - 1)}{k_y}\right]^{1/2} \cdot \xi \qquad \xi = \begin{cases} 1 & TE \\ \epsilon \\ \epsilon_{eff} \end{cases} TM \quad : \epsilon = \epsilon \text{ or } \epsilon_{eff} \tag{6.6}$$

giving:

$$\beta^2 = k_o^2 \epsilon - k_x^2 - k_y^2 \tag{6.7}$$

The order in which k_x and k_y are calculated depends upon the degree of confinement in each of the orthogonal directions, which is a function of both the refractive index change and the physical dimensions. The resonant condition may then be described by:

$$\beta l = m\pi \quad (m = 1, 2 \ldots) \tag{6.8}$$

Depending on the accuracy required, closed-form solutions may be substituted for Equ.(6.5) and (6.6), but otherwise for greater accuracy a numerical root search has to be performed to find the value of ϵ which gives the observed resonant frequency. This method may be used to determine the principal dielectric constants separately if the crystal axes are orientated as shown in Fig.6.6. This simplification may be deduced from the work by Steinberg et al. [11].

For Z- cut $LiNbO_3$ the dielectric constant perpendicular to the c-axis was obtained. X- and Y- cut $LiNbO_3$

were also used to find the dielectric constant parallel to the c-axis. However, if the crystal alignment with respect to the external field was slightly off-axis, a combination of the two dielectric constants would have been encountered [11].

The results obtained by this method are shown in Fig.6.8. from which the two dielectric constants were found to be 41.8 for $\epsilon_{\perp}$ and 30.6 for $\epsilon_{\parallel}$. When compared to the values usually quoted (44.3 for $\epsilon_{\perp}$ and 27.9 for $\epsilon_{\parallel}$) it is apparent that these values are greater and smaller than the quoted values respectively, which may be explained by the anisotropy of the material and the possible misalignment in cutting the crystal along the crystal axes. Further work is required to be done to investigate this aspect and also on characterising the dependence of the dielectric constants with temperature.

The accuracy of the above method can be guaged by comparing it with the results derived by Okaya et al. [12]. In their analysis an exact solution for the fields within and without the dielectric resonanator are derived. An estimate of the error incurred in calculating the dielectric constants by using the effective index method may be achieved by comparing with the results found by using Okaya's method. They state that their method is accurate to within a few percent. For example a sample of Z- cut $LiNbO_3$ of dimensions 4.84x15.30x1.02mm had a fundamental resonant frequency of 8.00GHz. The dielctric constant obtained from the effective index method for was 30.2 whereas that obtained from Okaya's analysis is 32.3, an error of less than 10%. It is assumed that for larger samples which exhibit greater confinement the error will be even less.

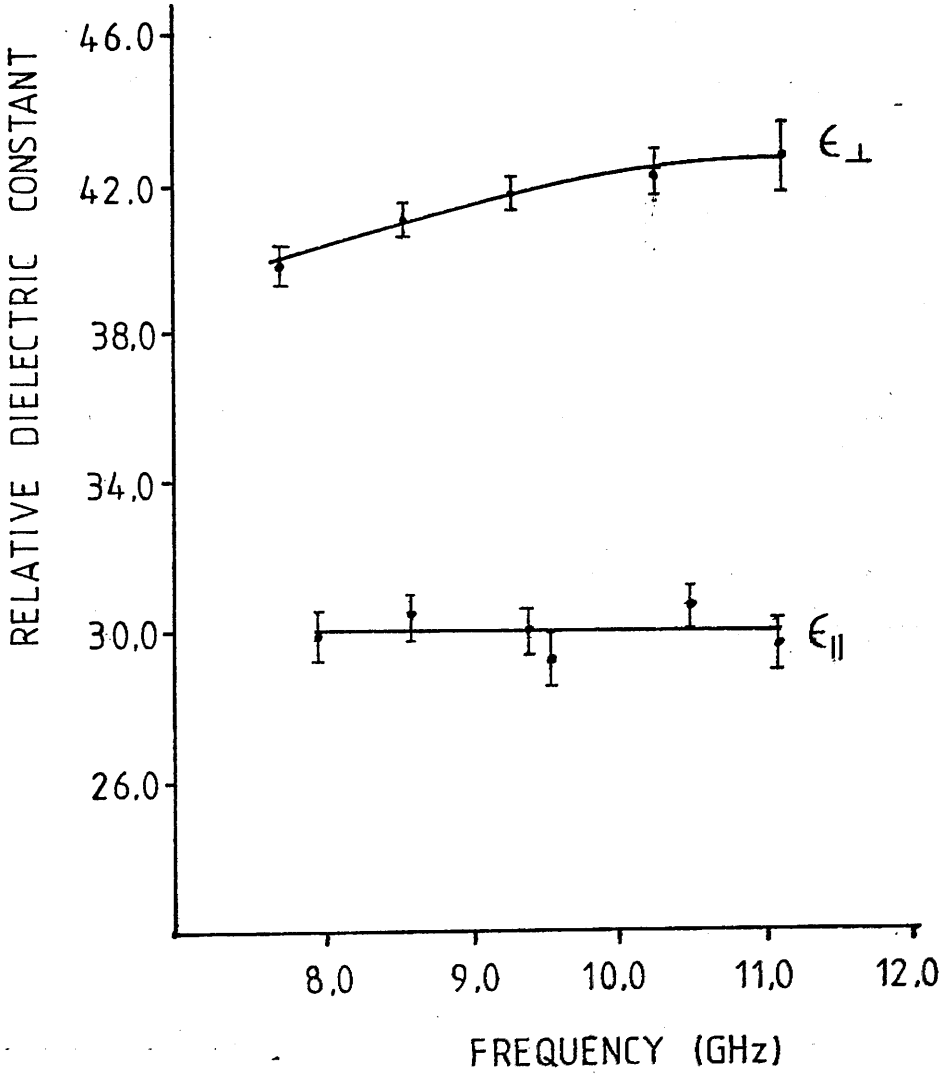

FIG.6.8. Unclamped dielectric constants for $LiNbO_3$ between 8.0-12.0GHz at 20°C.

Although only the fundamental mode was used to determine the dielectric constants, several other modes were observed in the frequency range 8 to 12GHz, and suggests that, for resonant electrode high frequency devices fabricated on $LiNbO_3$, parasitic resonances in the frequency response due to dielectric resonances may also be present. Energy will be coupled from the coplanar waveguide drive line on the substrate to the dielectric slab (assuming the correct field matching conditions), reducing the modulation efficiency of the device. This possibility has not been acknowledged in the literature [13], but rather degradation of the response has been attributed solely to the microwave packaging. The only way to reduce this problem is to have substrate dimensions which do not give any resonances in the frequency range of interest, or to ensure that the evanescent field coupling is minimised.

The remainder of this chapter will be devoted to a description of the experimental set-up required to detect and characterise the optical modulation at 10GHz produced by the standing wave modulator.

6.3. DETECTION OF OPTICAL MODULATION.

One of the most important characteristics of any type of optical modulator is its frequency response. For the standing wave modulator, the maximum phase change of the optical carrier at the resonant frequency is also an important parameter. In both cases, the modulation has to be detected and the relevant information about the modulating process extracted.

There are three methods available for observing the frequency spectrum of a phase modulated signal. These

are:

i) the scanning Fabry-Perot interferometer

ii) heterodyne/homodyne detection

iii) indirect low frequency detection.

The Fabry-Perot was not used because of the difficulty in obtaining mirrors with the correct radius of curvature for a free spectral range of at least 10GHz. A brief description of the other methods available will be given in turn, together with the appropriate mathematical assumptions which have to be made in the analysis. The experimental set up for the signal detection is shown in Fig.6.9.

The HeNe laser used operated at 0.633μm in a single transverse mode but with several longitudinal modes. The output from the laser was focussed onto the endface of the device by the usual endfire coupling technique [14]. A 40x microscope objective was used to focus the laser beam to a measured spot size of 5μm after it had passed through a $\lambda/4$ plate and a polariser to provide optical isolation. The input objective was mounted on a precision XYZ movement to provide flexibility of input launching into the waveguide. The device itself was mounted on a precision adjustable height and rotation stage. The output from the waveguide was imaged onto a photodetector by another microscope objective lens on an adjustable height stage.

Also shown in Fig.6.9. is the microwave configuration for driving the modulator. The experimental set-ups for the direct and indirect detection methods are also illustrated in Fig.6.9. The main difference between the two methods is the addition of a precision lock-in amplifier and a low frequency oscillator for the indirect

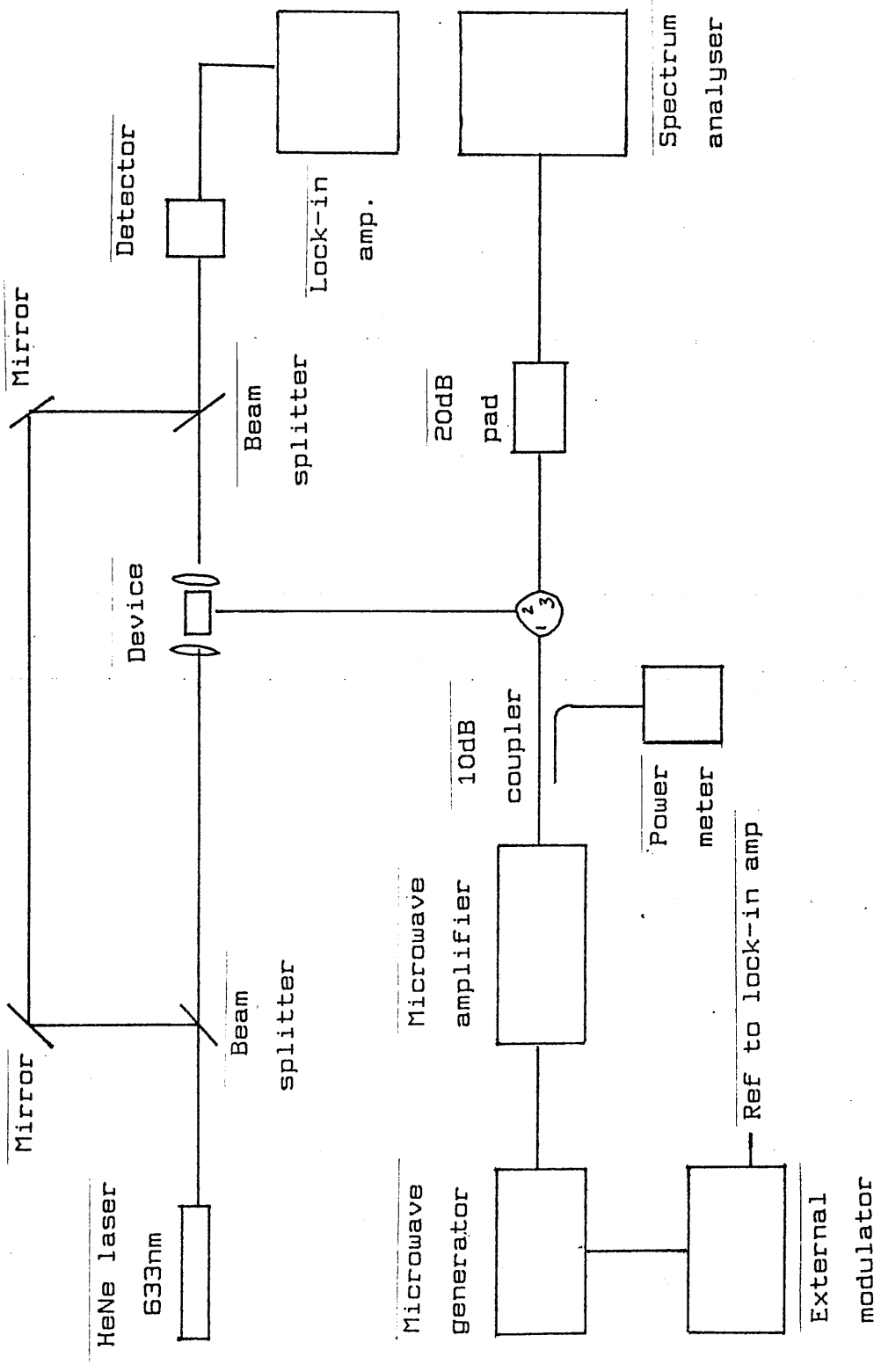

FIG.6.9. Experimental setup for optical characterisation of modulator.

method.

Direct detection of the modulated signal by the homodyne technique is conceptually the simplest method to understand. The output from the laser is split into two spatially separated beams by a beam splitter: one beam is directed onto the surface of a large bandwidth detector while the other beam is directed through the phase modulator. The output emerging from the modulator is then focussed onto the same area of the photodetector as the reference beam. At the surface of the photodetector a homodyning or beating process occurs between the two beams, with the result that the modulation on the carrier is reconstituted at baseband. The frequency response may then be determined by displaying the output of the detector on a spectrum analyser. It is assumed that the response of the photodetector is flat over the frequency range of interest. The demodulation process will now be described in detail.

6.3.1. MATHEMATICAL ANALYSIS OF DEMODULATION PROCESS.

The experimental set up shown in Fig.6.11. can be analysed as follows [15,16]: the carrier at frequency Ω_c is split into two beams one of which is angle modulated at a frequency of ω_m. The spatial difference between the two beams gives rise to an inherent phase shift of $\Delta\phi$ radians. The incident fields combine upon the detector which only responds to the time averaged incident power. This may be expressed as follows:

$$\langle EE^* \rangle = \langle \{ A\cos(\Omega_c t + M(\omega)\sin\omega_m t) + B\cos(\Omega_c t + \Delta\phi) \}^2 \rangle \qquad (6.9)$$

where $M(\omega)$ is the frequency response of the modulator which has to be measured. The output from the detector

can be rewritten in terms of a trigonometric expansion:

$$\langle EE^* \rangle = \frac{A^2}{2}\cdot\left[\cos 2(\Omega_c t + M(w)\sin w_m t + 1\right] + \frac{B^2}{2}\left[\cos 2(\Omega_c t + \Delta\phi)\right] + AB\cos\left(\Omega_c t + M(w)\sin w_m t\right).\cos\left(\Omega_c t + \Delta\phi\right) \quad (6.10)$$

The first two terms give the frequency components of the signal at d.c. and at $2\Omega_c$. Only the final term represents the baseband a.c. component. The other components are separated out by suitable filtering. The baseband component is then expressed as a sine expansion to give:

$$\frac{AB}{2}.\left\{\cos\left(2\Omega_c t + M(w)\sin w_m t + \Delta\phi\right) + \cos\left(M(w)\sin w_m t - \Delta\phi\right)\right\} \quad (6.11)$$

The first contribution in this expression again contains a frequency component at $2\Omega_c$, but on further expansion of the second term in Equ.(6.9) with the constraint that:

$$\Delta\phi = \frac{\pi}{2} \quad (6.12)$$

gives on substitution into Equ.(6.12):

$$\langle EE^* \rangle \quad \sin\left(M(w).\sin w_m t\right) \quad (6.13)$$

The final result can now be formulated in terms of an infinite series summation of Bessel functions:

$$\sin\left(M(w)\sin w_m t\right) = \sum_{n\,odd}^{\infty} 2.J_n(M)\sin n w_m t \quad (6.14)$$

If the drive power is low then the device will exhibit a linear characteristic around the operating point and M(w) can therefore be assumed to be small and linearly related to the frequency response. With this assumption the infinite series may be truncated to the first term of the expansion $J_o(M(w))$. The frequency response of the device is then mapped out by monitoring the amplitude of

the component at the external modulating frequency. If the drive power is sufficiently low then the Bessel function itself can be approximated by its argument.

6.3.2. FREQUENCY RESPONSE BY THE INDIRECT METHOD.

The indirect method of modulation detection dispenses with the requirement of a large bandwidth photodetector. Indeed only a limited bandwidth detector is necessary to map the high frequency response.

The slow variation response method was first proposed by Kaminow et al. [17] and further refined by Uehara [18] and Gee et al. [13]. This method monitors the low frequency sideband present in the optical signal due to low frequency modulation (<3kHz) amplitude modulating the microwave signal. The drive power to the modulator must again be of sufficient level so that the device operates in the quasi-linear region.

The mathematical development of this type of detection follows a similar argument to that given for direct detection. The modulating signal at ω_m is amplitude modulated by a signal of frequency ω_l so that the signal leaving the modulator may be expressed as:

$$E \propto \{A\cos(\Omega_c t + M(\omega)(1+\cos\omega_l t).\sin\omega_m t\} \qquad (6.16)$$

By using a similar experimental arrangement as for the direct detection the field present at the photodetector can be written as:

$$E \propto \{A\cos(\Omega_c t + M(\omega)(1+\cos\omega_l t).\sin\omega_m t + B\cos(\Omega_c t+\phi)\} \qquad (6.17)$$

and the output from the detector is proportional to the

time averaged incident intensity:

$$A^2.\cos^2[\Omega_c t + M(w)(1+\cos w_L t)\sin w_m t + B\cos(\Omega_c t+\phi) + B^2\cos^2 w_L t + 2AB\cos[\Omega_c t + M(w)(1+\cos w_L t)\sin w_m t].\cos(\Omega_c t+\phi) \quad (6.18)$$

The first two terms produce frequency components at $2\Omega_c$ whereas the last term only produces low frequency components. The last term may be simplified by the usual trigonometric expansion formula to give:

$$AB\{\cos\phi\cos[M(w)(1+\cos w_L t)\sin w_m t] + \sin\phi\sin[M(w).(1+\cos w_L t).\sin w_m t] - \cos[2\Omega_c t + M(w)(1+\cos w_L t)\sin w_m t] \quad (6.19)$$

Several of the above product terms may be expressed as summation expansions incorporating Bessel functions. The term ϕ is included to account for any phase difference between the reference beam and the modulated beam in the interferometer. It may be adjusted easily by changing the path difference in the reference arm. However, if $\phi=0$ then the first term in Equ.(6.19) predominates and may be rewritten as:

$$J_0[M(w)(1+\cos w_L t)] + \sum_{n\ \text{even}}^{\infty} 2J_n[M(w)(1+\cos w_L t)].\sin w_m n t \quad (6.20)$$

The only term in the above expression which does not contain harmonics of the driving R.F. signal is the first term. Assuming that the drive power is low then the argument of the zero order Bessel function is small and may be approximated by:

$$J_0(x) = 1 - \frac{x^2}{4} \quad x \ll 1 \quad (6.21)$$

or:

$$J_0[M(w)(1+\cos w_L t)] \cong 1 - \frac{1}{4}\{M(w) + M(w)\cos w_L t\}^2 \quad (6.22)$$

The output from the photodetector is restricted to very

low frequencies by virtue of its limited bandwidth so that it is onlt the amplitude of the low frequency component which is detected by either a spectrum analyser or a lock-in amplifier. Irrespective of the method employed to detect the low frequency signal, the frequency response of the device is proportional to the square root of the amplitude:

$$M^2(\omega) \propto a \qquad (6.23)$$

6.4. EXPERIMENTAL RESPONSE OF STANDING WAVE MODULATOR.

The operation of the modulator was demonstrated by the indirect demodulation process described in the preceding section. The device was incorporated into one arm of a Mach-Zehnder interferometer, and the resulting interference signal monitored by a low frequency photodetector.

The microwave drive to the modulator was set at the resonant frequency of the electrode structure. The resonant frequency was obtained by observing the return power from the device on a spectrum analyser. The modulating R.F. signal was, in turn, amplitude modulated by a low frequency square wave of frequency 1kHz. The magnitude of the 1kHz component monitored by the photodetector gradually increased as the R.F. power was increased. However, no noticeable increase in the detected signal was apparent for powers above 25mW. An exact figure for the depth of modulation could not be obtained due to the uncertainty of the operating point on the Mach-Zehnder characteristics.

6.5. SUMMARY.

This chapter has described the three main detection techniques available for characterising the high frequency phase modulation produced by any type of integrated phase modulator. The microwave response of the resonant line was also verified experimentally and subsequently compared with the predictions from the theory of Chapter 3. It was found that the theory gave values in close agreement with those obtained experimentally.

An attempt was made to explain the other resonances sometimes present in the experimental return power from the electrode structure. It was found that the parasitic resonances could be explained in terms of the substrate acting as a bulk dielectric resonator. From the investigation into the bulk resonances a method was developed whereby the high frequency dielectric constants of the substrate may be obtained.

Although a full characterisation of the phase modulation of the standing wave modulator remains to be performed, the basic operation was demonstrated during the course of this work. Of prime importance in any future investigation would be the determination of the efficiency of the device. The requirement of incorporating a d.c. bias arrangement into the electrode pattern of the device should be investigated as well.

References Chapter 6.

[1] D.F.Clark,A.C.G.Nutt,M.R.S.Taylor and R.M.DeLaRue.
Design procedure and experimental characterisation of a standing wave electrode electro-optic modulator.
I.E.E. Colloquium "Optical control and generation of microwave signals."
London,1986.

[2] R.C.Alferness.
Waveguide electro-optic modulators.
I.E.E.E. Trans. Microwave Theory and Tech.
Vol.M.T.T.30(8),1982.pp.1121-1137.

[3] E.L.Ginzton.
Microwave Measurement.
McGraw-Hill,1957.
Chapter 9.

[4] K.Kubota,J.Noda and O.Mikami.
Travelling wave optical modulator using a directional coupler LiNbO3 device.
I.E.E.E. J. Quant. Electrs.,Vol.QE16(7),1980.
pp.754-760.

[5] J.R.Teague,R.R.Rice and R.Gerson.
High frequency dielectric measurements on electro-optic single axis crystals.
J. Appl. Phys.,Vol.46(7),1975,pp.2864-2866.

[6] R.M.Knox and P.P.Toulios.
Integrated circuits for the millimetre through optical frequency range in Fox,J. (Ed) "Proceedings of the M.R.I. symposium on submillimeter waves."
Polytech Press.
Brooklyn, N.Y., 1970.
pp.497-516.

[7] C.M.Kim,B.G.Jung and C.W.Lee.
Analysis of dielectric rectangular waveguide by modified effective index method.
E;ectr. Letts.,Vol.22(6),1986,pp.296-298.

[8] T.D.Iveland.
Dielectric resonator filters for application in microwave integrated circuits.
I.E.E.E. Trans. Microwave Theory and Tech.
Vol.M.T.T.19(7),1971,pp.643-650.

[9] J.C.Sethares and S.J.Nauman.
Design of microwave dielectric resonators.
I.E.E.E. Trans. Microwave Theory and Tech.
Vol.M.T.T.14(1),1966,pp.2-7.

[10] E.A.J.Maracatili.
Dielectric rectangular waveguide and directional coupler for integrated optics.
B.S.T.J.,Vol.48(7),1969,pp.2071-2112.

[11] R.A.Steinberg and T.G.Gioallorenzi.
Modal fields of anisotropic channel waveguides.
J. Opt. Soc. Am.,Vol.67(4),1977,pp.523-533.

[12] A.Okaya and L.F.Barash.
The Dielectric Resonator.
Proc. I.R.E.,Vol.18(8),1962,pp.2081-2092.

[13] C.M.Gee,G.D.Thurmond and H.W.Yen.
17GHz bandwidth electro-optic modulator.
Appl. Phys. Letts.,Vol.43(11),1983,pp.998-1000.

[14] I.Andonovic.
Lithium Niobate Waveguide Devices.
Ph.D. Thesis, University of Strathclyde,1983.

[15] A.B.Carlson.
Communications Systems.
McGraw-Hill, 2nd. ed.,1975.
Chapter 6.

[16] M.Schwartz.
Information transmission, Modulation and
Noise.
McGraw-Hill,2nd. ed.,1970.

[17] I.P.Kaminow and W.M.Sharpless.
Performance of $LiTaO_3$ and $LiNbO_3$ light
modulators at 4GHz.
Appl. Opt.,Vol.6(2),1967,pp.351-352.

[18] S.Uehara.
Calibration of optical modulator frequency
response with application to signal level
control.
Appl. Opt.,Vol.17(1),1978,pp.68-71.

CHAPTER 7.

CONCLUSIONS AND FUTURE WORK.

The scope of this thesis has encompassed the theoretical analysis of optical waveguides, the investigation of proton-exchange waveguides and the theoretical design and experimental demonstration of a new type of integrated optical modulator - the standing wave electro-optic modulator [1].

The analysis of integrated optical waveguides which exhibit confinement in two directions has been described in Chapter 2. Several methods have been considered for calculating the effective index, which ranged from a simple variable separation technique [2] to a sophisticated numerical method incorporating a Rayleigh-Ritz minimisation procedure [3]. It has been found that the simplest method capable of giving close agreement with numerical techniques was that proposed by Knox et al. [4] - the effective index method.

The effective index method could be applied to a variety of diffused and etched waveguide configurations with confidence as long as the limitations associated with this method were recognised. For the effective index method to be meaningful, the waveguides had to have a large aspect ratio and a large refractive index change. If these conditions were not fulfilled, recourse had to be made to a more complex analysis technique. For multi-layer structures, the transverse resonance method was found to provide the simplest method of analysis. The behaviour of optical waveguides covered by metal films could also be analysed by the transverse resonance method. Caution had to be taken to ensure that

the correct nomenclature for the TM-modes was used [5].

An attempt was also made to analyse the effect of a Schottky barrier upon the carrier distribution underneath an etched rib waveguide formed in GaAs. The method involved solution of Poisson's equation numerically, subject to boundary conditions. The end result was an indication of the carrier concentration and modulating voltage necessary to fully deplete the region underneath the contact. Further work is required to ascertain the electrical capacitance of such a Schottky contact and therefore find the maximum operating frequency possible for such a device and to obtain values for the change in refractive index due to free carrier depletion.

Chapter 3 introduced the theoretical design of the standing wave modulator. In contrast with the travelling wave device, the standing wave modulator exhibits a relatively narrow bandwidth resonance. It was shown that the resonant frequency was controlled by the length of the resonant line whereas the bandwidth was fixed by the attenuation of the line. Significant work remains to be carried out on modelling the effects of radiation at the ends of the resonant line and of the finite conductance presented by the short circuits. A new figure of merit based upon the average voltage along the interaction region was derived to compare accurately the performance of travelling wave and standing wave modulators.

The fabrication techniques necessary to successfully define the optical waveguide and electrode patterns on $LiNbO_3$ have been described in Chapter 4. A modification to the standard photolithographic processes was required to permit the patterning of thick, thermally deposited

metallic films by lift-off. The thickness of the metal film was of prime importance in determining the bandwidth of the standing wave modulator. Subsequent work to assess the feasibility of using electrolytically grown metal films for the electrode structure remains to be done.

The proton-exchange method for fabricating optical waveguides with a large index change has been discussed in Chapter 5, along with values of the index change, refractive index profile and diffusion characteristics for Z- and X-cut proton-exchanged $LiNbO_3$. Techniques for reducing the effects of the more serious problems associated with proton-exchange i.e. the gradual reduction of the maximum refractive index change and the high scattering losses were also presented. Possible solutions to the refractive index variation were examined such as annealing and exchanging in dilute melts. The formation of stripe waveguides was investigated and the results analysed by the methods covered in Chapter 2 in order to derive fabrication conditions for the formation of mono-mode waveguides.

A brief summary has been included concerning the analytical methods employed in characterising the proton-exchange diffusion mechanism and explaining the refractive index variation in terms of strain induced in the lattice structure. A complete analysis of the proton-exchange diffusion mechanism still remains to be carried out.

The experimental evaluation of the standing wave modulator has been discussed in Chapter 6. The response of the resonant electrode structure was verified experimentally and compared with the theoretical model. Possible reasons for the difference between the

theoretically calculated and the experimentally measured values were assessed. The determination of the dielectric constants for $LiNbO_3$ was investigated by considering it as a dielectric resonator. It was found that the values for the dielectric constants agreed to within 10% with values used by other researchers. The variation of the dielectric constants with temperature will also require further investigation to determine the dependence of the matching condition upon the drive R.F. power and heating effects along the modulating section of the electrode structure.

Although a convincing demonstration of the operation of the standing wave modulator was observed, a full characterisation of the performance of the standing wave modulator remains to be carried out. This characterisation will include a measure of the maximum phase deviation for a particular input drive power as well as the overall frequency response. Further investigation should address the feasibility of fabricating modulators functioning at centre frequencies up to 40GHz from the theoretical model developed.

References Chapter 7.

[1] D.F.Clark,A.C.G.Nutt,M.R.S.Taylor and R.M.DeLaRue.
Design procedure and experimental characterisation of a standing wave electrode electro-optic modulator.
I.E.E. Colloquium "Optical control and generation of microwave signals."
London, 1986.

[2] E.A.Marcatili.
Dielectric rectangular waveguide and directional coupler for integrated optics.
B.S.T.J.,Vol.48(3),1969,pp.2071-2102.

[3] M.Matsuhara.
Analysis of T.E.M. modes in dielectric waveguides by a variational techniqe.
J. Opt. Soc. Am.,Vol.63(12),1973,pp.1514-1517.

[4] R.M.Knox and P.P.Toulios.
Integrated circuits for the millimetre through optical frequency range. in Fox,J.(Ed) "Proceedings of the MRI Symposium on Submillimeter waves."
Brooklyn, N.Y.,1970.
pp.497-516.

[5] A.A.Oliner and S.T.Peng.
Effects of metal overlays on 3-D optical waveguides.
Appl. Opts.,Vol17(18),1978,pp.2866-2867.

APPENDIX A.

THE ELECTRO-OPTIC EFFECT.

The linear change in the refractive index of a crystal resulting from the application of an external electric field is termed the Pockels or linear electro-optic effect [1]. The Pockels effect is only of significance in crystals which lack a centre of symmetry.

The usual method of describing the refractive index of a general crystalline material is by the indicatrix or index ellipsoid [2] i.e.:

$$\frac{x^2}{n_x^2} + \frac{y^2}{n_y^2} + \frac{z^2}{n_z^2} = 1 \qquad \text{(A1)}$$

where x,y,z are parallel to the principle axes of the crystal. The effect of the electric field across the crystal upon the propagating optical field is expressed by giving the changes in the constants $1/n_x^2$, $1/n_y^2$, $1/n_z^2$ of the indicatrix. Equ.(A1) on application of an electric field transforms to:

$$\left(\frac{1}{n_1^2} + \Delta\left(\frac{1}{n^2}\right)_1\right)x^2 + \left(\frac{1}{n_2^2} + \Delta\left(\frac{1}{n^2}\right)_2\right)y^2 + \left(\frac{1}{n_3^2} + \Delta\left(\frac{1}{n^2}\right)_3\right) + 2\Delta\left(\frac{1}{n^2}\right)_4 yz + 2.\Delta\left(\frac{1}{n^2}\right)_5 xz + 2\Delta\left(\frac{1}{n^2}\right)_6 = 1 \qquad \text{(A2)}$$

This indicates that the major axes are no longer parallel to x,y,z.

The linear change in the polarisation coefficients $\Delta\left(\frac{1}{n^2}\right)_i : i=1,..,6$ due to an arbitrary electric field is given by:

$$\Delta\left(\frac{1}{n^2}\right)_i = \sum_{j=1}^{3} r_{ij} E_j \; : \; i=1,\ldots,6 \qquad \text{(A3)}$$

The above equation can be written as a third-rank tensor which may be conveniently simplified to a 6x3 matrix representation. The elements within the third-rank tensor are termed the electro-optic coefficients. The electro-optic coefficients relate the applied electric field, light polarisation and propagation directions to the index changes.

The form of the simplified matrix representation is further reduced by symmetry considerations which dictate that several of the terms are zero. As an example , for $LiNbO_3$, with the electric field component along the z-axis (to utilise the r_{33} coefficient) gives the indicatrix as:

$$\frac{x^2+y^2}{n_o^2} + \frac{z^2}{n_e^2} + r_{33}E_z z^2 + r_{13}E_z x^2 + r_{13}E_z y^2 = 1 \qquad (A4)$$

since $E_x=E_y=0$ and $n_x=n_y=n_o$, $n_z=n_e$ as it is an uniaxial crystal.

The above expression can be further simplified by transforming to a new co-ordinate system x', y', z' such that:

$$\frac{1}{n_{x'}^2} = \frac{1}{n_{y'}^2} = \frac{1}{n_o^2} + r_{13}E_z \quad : \quad \frac{1}{n_{z'}^2} = \frac{1}{n_e^2} + r_{33}E_z \qquad (A5)$$

by assuming $r_{13}E_z \ll n_o^{-2}$ and $r_{33}E_z \ll n_e^{-2}$ leads to:

$$n_{x'} = n_{y'} = n_o - \frac{n_o^3 r_{13} E_z}{2} \qquad (A6a)$$

and

$$n_{z'} = n_e - \frac{n_e^3 r_{33} E_z}{2} \qquad (A6b)$$

Therefore the change in the refractive index induced by the external voltage is:

$$\Delta n_o = -\frac{n_o^3 r_{13} E_z}{2} \quad : \quad \Delta n_e = -\frac{n_e^3 r_{33} E_z}{2} \qquad (A7)$$

However certain crystals exhibit the piezoelectric effect (eletric field induced stress) which must be incorporated to give a more complete description of the total refractive index change. The stress associated with the external electric field will modify the refractive index through the photo-elastic effect. Clearly, the external environmental conditions play an important role on determining the magnitude of the electro-optic coefficients. In general, the electro-optic coefficients for the constant strain (high frequency) and constant stress (low frequency) are cited, depending on whether the external modulating field is above and below the mechanical resonances of the crystal respectively.

The response time of the electro-optic effect is limited only by the time of electronic transitions within the lattice which is of the order of 10^{-12} to 10^{-13} seconds.

The reduced form of the electro-optic tensor for GaAs and $LiNbO_3$ is shown in Fig.A.1.

For $LiNbO_3$:

$$\begin{pmatrix} 0 & -r_{22} & r_{13} \\ 0 & r_{22} & r_{13} \\ 0 & 0 & r_{33} \\ 0 & r_{42} & 0 \\ r_{42} & 0 & 0 \\ -r_{22} & 0 & 0 \end{pmatrix}$$

Clamped state at 633nm (room temp.):

r_{33}	r_{13}	r_{22}	r_{42}	
30.8	8.6	3.4	28.0	$\times 10^{-12}$ m/V

For GaAs:

$$\begin{pmatrix} 0 & 0 & 0 \\ 0 & 0 & 0 \\ 0 & 0 & 0 \\ r_{41} & 0 & 0 \\ 0 & r_{41} & 0 \\ 0 & 0 & r_{41} \end{pmatrix}$$

Clamped state at 1500nm (room temp.):

r_{41}	
1.1 $\times 10^{-12}$	m/V

FIG.A1. Matrix representation of reduced electro-optic tensor for $LiNbO_3$ and GaAs.

References Appendix A.

[1] J.F.Nye.
Physical Properties of Crystals.
Oxford University Press,1960.

[2] A.Yariv.
Introduction to Optical Electronics.
Holt,Rinehart and Winston,New York,1976.

APPENDIX B.

A simple analysis is presented to compare the relative magnitudes of the input drive powers required to produce a phase shift of π radians by the travelling wave and standing wave modulators. The analysis for the standing wave modulator will be considered first.

If it is assumed that the standing wave modulator is at resonance, then the voltage distribution along the electrode is approximately:

$$|V(z)| = |V_0| \sin \beta z \qquad \text{(B1)}$$

where $|V_0|$ is the peak voltage at the centre of the electrode. The voltage at the input feed plane, (Fig.3.1) taking into account the resonance enhancement, close to one end is:

$$|V(\ell)| \doteq \frac{|V_0| \beta \ell}{Q} \qquad \text{(B2)}$$

V(1) is related to the input drive power by:

$$P_i = \frac{|V(\ell)|^2}{2 Z_0} \qquad \text{(B3)}$$

The average voltage along the electrode is:

$$|V_{av}| = \frac{\int_0^{\lambda_g/2} |V_0| \sin \beta z \, . \, dz}{\lambda_g/2} \qquad \text{(B4)}$$

which, when evaluated gives:

$$|V_0| = |V_{av}| \frac{\pi}{2} \qquad \text{(B5)}$$

or after substituion into Equ.(B2) produces:

$$|V(\ell)| \doteq \frac{\pi |V_{av}| \beta \ell}{2Q} \qquad \text{(B6)}$$

The induced phase shift, ignoring phase mismatch between the optical and the r.f. field and r.f. attenuation for both devices is given by (Chapter 3):

$$\Delta\phi = \frac{\pi n_o^3 r_{33} V_{av} \Gamma \ell}{\lambda d} \qquad \text{(B7)}$$

Ignoring the phase mismatch factor is equivalent to assuming an ideal travelling wave modulator and a non ideal standing wave modulator. From Equ.(B7), the voltage V_{av} required to induce a phase shift of π radians for a device 3.6mm long with an electrode separation of 10 um can be evaluated. If Γ is taken as unity and λ =0.633μm then V_{av} is found to be 5.5V. The input voltage V(1) is calculated to be 0.23V for a Q of 10, which corresponds to an input power of 0.5mW.

The equivalent drive power to produce the same phase modulation from an ideal travelling wave modulator is 300mW (Equ.(B3) with V(1)=5.5V). However, the R.F. power delivered to the standing wave modulator has to be completely dissipated by the electrode structure, whereas for the travelling wave configuration only a proportion of the incident power is absorbed. In both situations the aborption of the r.f. power manifests itself as a local temperature rise at the interface between the elctrode and the substrate. It should be remembered that a travelling wave device with ~19GHz bandwidth has been compared with a standing wave device at centre frequency of 10GHz.

An analysis may be performed to find the approximate temperature rise associated with the r.f. power

dissipation along each structure. The analysis here follows that of Fujii et al. [1] with the assumptions that (i) only the crystal is heated, (ii) the heat flow is approximated by semi-circular isothermal contours and (iii) the lower boundary of the crystal is in contact with a thermal reservoir. The variation of the temperature with depth is described by the following differential equation:

$$\frac{dT}{dD} = \frac{-\dot{Q}}{\lambda_c L R} \qquad (B8)$$

where $\dot{Q}$ is the heat flow per second
λ_c is the thermal conductivity of the substrate
L is the electrode length
and R is the contour length (see Fig.B1)

Integrating Equ.(B8) leads to a simple expression for T:

$$T = -\frac{\dot{Q}}{\lambda_c L \phi} \cdot \ln\left[\frac{D+d_o}{D_o+d_o}\right] + T_o \qquad (B9)$$

where the term D_o is the substrate thickness and ϕ is the angle of the sector forming the contour. For $LiNbO_3$ with $\lambda_c = 4.2.10^{-2} W/mK$ [2] the temperature at the crystal surface (D=0) for an input power of 0.5mW is approximately 10°C. The corresponding power giving the temperature rise along the travelling wave structure, taking into account the attenuation factor of 2dB/cm (the value used for the standing wave modulator) is:

$$P = P_i\left(1 + \frac{1}{2\alpha l}\left[e^{-2\alpha l} - 1\right]\right) \qquad (B10)$$

which gives an average power dissipation of 30mW and is equivalent to a temperature rise of approximately 600°C. It should be noted that for the travelling wave structure, an attenuation factor of less than 1dB/cm is

attainable. It was observed that drive powers in excess of 25mW destroyed the electrode structure of the standing wave modulator and from the analysis this would correspond to a temperature rise of 500°C which is close to the melting point of aluminium (m.p.~650°C).

In conclusion the effective temperature increase for both modulators for the equivalent input powers to produce the same phase change are almost identical.

References Appendix B.

[1] Y.Fujii,K.Kajimura,S.Ishihara & H.Yajima.
Thermal-gradient-induced optical deflection
in TiO_2 crystals.
Appl. Phys. Letts. Vol.41(3),1982,pp.217-219

[2] Barr and Stroud,
Data sheet.
Lithium Niobate crystals.

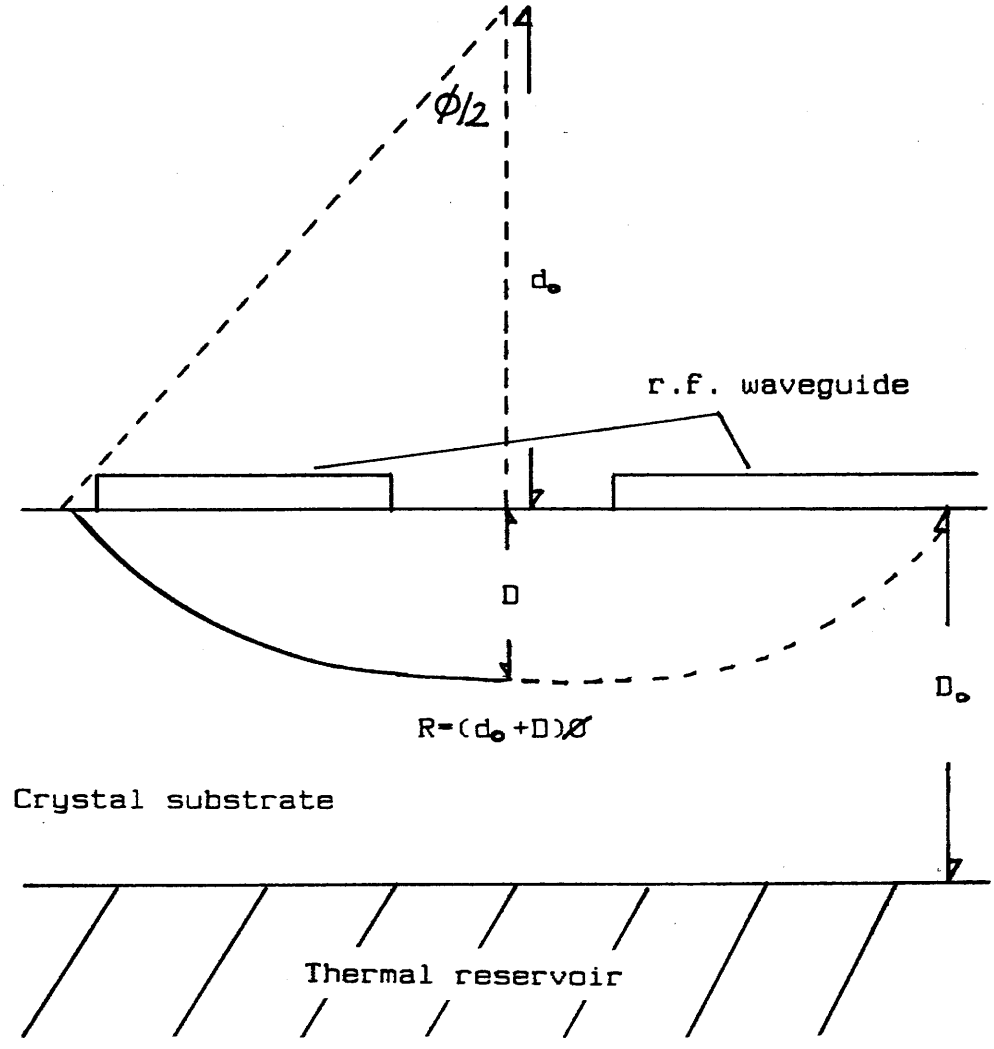

FIG.B1. Model for calculation of heating effect.

LIST OF PUBLISHED WORK.

1) D.F.Clark,A.C.G.Nutt,K.K.Wong,P.J.R.Laybourn, and R.M.DeLaRue.
Characterisation of proton-exchanged slab optical waveguides in Z- cut $LiNbO_3$.
J. Appl. Phys.,Vol.54(11),1983,pp.6218-6220.

2) A.C.G.Nutt,K.K.Wong,D.F.Clark,P.J.R.Laybourn and R.M.DeLaRue.
Proton-exchanged lithium niobate slab and stripe optical waveguides:characterisation and comparisons.
2nd. E.C.I.O.,Firenze,1983. I.E.E. Conf. Pub. No.227,1983,pp.53-56.

3) K.K.Wong,A.C.G.Nutt,D.F.Clark,J.Winfield, P.J.R.Laybourn and R.M.DeLaRue.
Characterisation of proton-exchanged slab optical waveguides in X- cut $LiNbO_3$.
I.E.E. Proc. Pt.J,Vol.133(2),1986,pp.112-116.

4) D.F.Clark,A.C.G.Nutt,M.R.S.Taylor and R.M.DeLaRue.
Design procedure and experimental characterisation of a standing wave electro-optic modulator.
I.E.E. Colloquium "Optical control and generation of microwave signals."
London,1986.